POLITECNICO DI MILANO
DEPARTMENT OF CIVIL AND ENVIRONMENTAL ENGINEERING
DOCTORAL PROGRAMME IN ENVIRONMENTAL AND INFRASTRUCTURE ENGINEERING

UAV SURVEYS FOR CROP MONITORING AND MANAGEMENT IN PRECISION AGRICULTURE

Doctoral Dissertation of:
Giulia Ronchetti
Matr. 879697

Supervisor:
Dr. Giovanna Sona

Tutor:
Prof. Riccardo Barzaghi

The Chair of the Doctoral Program:
Prof. Riccardo Barzaghi

2016/2019 – XXXII Cycle

Abstract

Precision Agriculture is generally defined as “doing the right practice at the right location and time at the right intensity”. To achieve this, the knowledge of crop and soil characteristics is fundamental and new technologies have been growing in the last thirty years. In this context, Unmanned Aerial Vehicles (UAVs) surveys can provide a simple, reliable and cost-effective way to monitor agricultural areas.

This dissertation demonstrates the potential of the use of UAVs in agriculture and tries to find solutions to some relevant issues still open, in order to encourage the spread of UAV surveys for crop monitoring and management. The final aim of the thesis is to recommend guidelines for conducting UAV surveys in precision agriculture applications. Some critical aspects of the surveys are addressed in it, from sensors analysis to data exploitation, by means of four different case studies. In the first, the radiometric calibration of sensors is presented, with a careful analysis of the consistency of multispectral datasets acquired by a common and widespread sensor, the Parrot Sequoia camera. The performances of different processing strategies are analyzed and compared and finally the reliability of results is assessed with respect to Sentinel-2 data. In the second case study, some practical aspects of surveys and processing are illustrated, in order to generate accurate terrain models with a low-cost mass market UAV in a vineyard. The best flight configurations are studied together with the various processing software available on the market, to optimize survey times and costs without excluding the accuracy of the final product. The third case focuses on one of the topics most studied by researchers: the detection of crop rows from UAV imagery to derive specific information on vegetation canopy. Thresholding algorithms, classification algorithms and Bayesian segmentation are tested and compared on three different crop types, namely grapevine, pear and tomato, for analyzing the suitability of the methods according to the characteristics of each crop. Finally, the last study is an example of the effectiveness of the use of UAV in precision agriculture. It deals with the integration of data collected by UAV and geophysical ground-based surveys to delineate site-specific management zones in a vineyard. For this purpose, the use of UAV multispectral and thermal images provides a unique way to get information related to the crop development along the growing season.

Contents

List of Figures

List of Tables

CHAPTER 1

Introduction

The term "Precision Agriculture" was adopted for the first time at the beginning of the nineties, as the title of a workshop held in Great Falls (Montana, USA) about modern agricultural practices (Oliver et al., 2013). Precision Agriculture (PAg) can be generally defined as “doing the right practice at the right location and time at the right intensity” (Mulla and Khosla, 2016). This requires a detailed description of the variability at field scale of soil and crop properties, in order to manage water and nutrients with variable rates, according to the actual irrigation and nutrient requirements (Ortuani et al., 2019). Fields are not treated homogeneously, but are divided in management zones and the right treatments are provided separately within each zone (Maes and Steppe, 2019). Benefits of PAg are twofold: on one hand, saving the environment, by reducing the environmental impacts of agricultural practices and limiting the waste of natural resources, on the other hand, increasing farmers’ incoming, by decreasing their inputs without affecting or even improving the quality of crop yield (Mulla, 2013).

Fundamental in PAg is the knowledge of the in-field spatial variability of soil and crop properties. Since the last four decades, Remote Sensing (RS) techniques have been widely adopted to collect spatial information on crops and soils. A detailed review of the use of RS in agriculture is provided in Mulla (2013). Starting from the launch of Landsat missions in 1972, satellite RS has been used to monitor crops status and retrieve correlation between spectral data and crop yield (Tucker et al., 1980). Satellite RS provides a unique way to obtain estimates over spatially extensive areas, strongly contributing in PAg applications from regional to global scale (Atzberger, 2013). Various are RS applications in agriculture: monitoring vegetation vigor (Sashikkumar et al., 2017), assessing crop phenological stages (Boschetti et al., 2018), estimating crop biomass (Guerini Filho et al., 2019). Variables collected with RS technologies help in yield forecasting many existing operational large-scale agricultural monitoring systems (Fritz et al., 2019). Among all, a special mention for the Food Security unit at JRC of the European Commission in Ispra (Italy) (López-Lozano et al., 2015).

Nevertheless, satellite RS applications are limited by the spatial and temporal resolution available from these systems, which is often not suited to meet local objectives, in particular at field-scale level. In recent years, a noteworthy development of Unmanned Aerial Vehicles (UAVs) has been registered, in terms of vehicles miniaturization, improvement of their components, especially GNSS (Global Navigation Satellite System) and INS (Inertial Navigation System) systems, and availability of new and ultra-light sensors. This advancement has made the UAV a suitable platform to collect data in agricultural applications, filling the gap between RS and terrestrial techniques (Pádua et al., 2017). Using UAVs is a good compromise between the large coverage obtainable with remote platforms (mainly satellite and aircraft) and the accuracy of the terrestrial data, with advantages in terms of time-consumption and costs of the surveys. In Figure 1.1, a comparison of different survey systems is proposed, by relating the extension of the area of interest and the spatial resolution of the acquired images. Unlike satellites and airplanes, the increase in resolution compensates for the decrease in the size of the area and makes UAVs the platform dedicated to identifying within-field variations in agriculture.

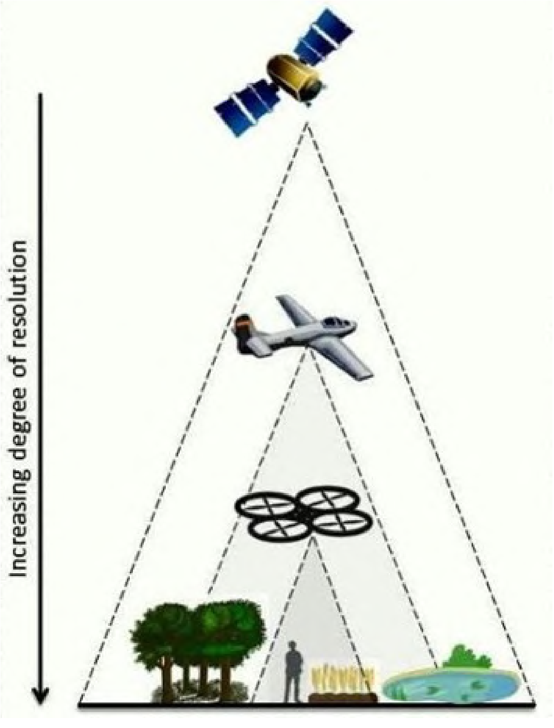

Figure 1.1: *Comparison among different survey systems, as respect to the extension of the area of interest and resolution, in Nixon et al. (2017).*

UAVs have introduced a new point of view for agricultural surveys, by allowing to collect information closely from above, giving rise to several applications. As early as 2008, Nebiker et al. (2008) proposed the prototype of a multispectral sensor suitable to be mounted on UAV and conducted experiments with it to assess vegetation health with promising results. Starting from this experience, a variety of studies can be found in the literature about effective UAV surveys conducted for PAg purposes. Main applications involve in-field weed mapping, vegetation growth monitoring and yield estimation, crop water stress analysis and optimization of irrigation management (Pádua et al., 2017, Tsouros et al., 2019). De Castro et al. (2018b) exploited the very-high resolution of UAV imagery to map weeds in sunflowers and cotton fields, developing an algorithm based on machine learning techniques. In Stroppiana et al. (2018), the presence of weeds in rice fields was detected by means of an automatic procedure for classifying UAV data at early stages of the growing season. Nebiker et al. (2016) investigated the suitability of UAV surveys with light-weight sensors for crop yield prediction of rape and barley, finding high correlation values between vegetation indices derived from UAV images and reference yield measures. UAV data were adopted in Stroppiana et al. (2019) for estimating maize vegetation density at the beginning of the season in Northern Italy. In Hoffmann et al. (2016), crop water stress maps were derived from RGB and thermal UAV imagery for spring barley fields located in Western Denmark in different moments of the season. Caruso et al. (2019) conducted experiments on both irrigated and rainfed olive orchards in order to estimate tree height, canopy diameter and canopy volume from UAV images. Quebrajo et al. (2018) stressed the needs of site-specific irrigation strategies by evaluating water status of sugar beet plants from thermal data acquired with UAV surveys. In addition, some papers focus not only on application results but also on assessing methodologies performances. Gómez-Candón et al. (2016) proposed new insights for acquiring and calibrating thermal UAV imagery, aiming at correcting errors due to sensors drift during data capturing. The methodology described in Zhang et al. (2019a) involves the concurrent use of RGB and thermal UAV imagery for the accurate extraction of maize temperature canopy. In Poncet et al. (2019), accuracies of five different radiometric calibration methods, commonly used on multispectral UAV data, were investigated, providing a better understanding on advantages and limitations on the compared methods.

The major strength of UAV surveys is providing information of various kinds, thanks to the versatility of the sensors that can be mounted, in a rapid, non-invasive and extensive way, and at the same time with a level of detail such that can detect within-field variations. On the other hand, the weak point lies in the capability to transform the acquired data into helpful information for crop management and make the data easily usable and understandable to the stakeholders, mainly farmers. Despite all the efforts, a standardized workflow to perform successful UAV-based surveys in PAg is still missing (Tsouros et al., 2019). Some practical and technical expertise are required to exploit the acquired data, in particular knowledge related to remote sensing and photogrammetry sectors, thus preventing a wider use of UAV among farmers for operational use (Maes and Steppe, 2019, Tsouros et al., 2019). The main challenges still refer to both data collection and data processing. This dissertation arises from these problems and tries to find solutions to some relevant issues still open, in order to encourage the spread of UAV surveys for PAg applications. The final aim of this thesis is to propose guidelines and define best practices for performing effective UAV surveys in agriculture. Therefore, some critical aspects of UAV-based surveys are faced in it, from sensors analysis to data exploitation, by means of four different case studies, conducted during my PhD career. In the first case, analysis of radiometric performances of a popular multispectral sensor is addressed, by comparing results that can be obtained following different elaboration strategies. The second case study focuses on the best practices of data acquisition and processing in order to obtain accurate products with a mass-market UAV equipped with a fisheye camera on a vineyard. Methodologies for detecting crop rows on UAV imagery are presented in the third study and then one of these methods has been used in the fourth case study, to produce site-specific management zones maps in a vineyard. The latter is a clear example of the potential of UAV surveys in PAg, by combining UAV-based and ground-based measurements. Three of the reported case studies have been already presented to the public as articles that I have authored or co-authored and published in scientific journals or in conference proceedings, in the last three years. Specifically the first, the second and the fourth case study refer to Franzini et al. (2019), Ronchetti et al. (2018) and Ortuani et al. (2019), respectively.

The rest of the dissertation is organized as follows. In Chapter 2 a review on UAV-based RS for PAg is presented, including a description of the most popular vehicles, sensors and processing software packages. Chapter 3 focuses on the radiometric assessment of the multispectral sensor Parrot Sequoia (Franzini et al., 2019), while Chapter 4 is about the generation of terrain models in a vineyard through fisheye imagery (Ronchetti et al., 2018). In Chapter 5, the problem of images segmentation is addressed, by presenting methodologies for extracting vegetation canopy from the background for different crop typologies. The integration of geophysical ground-based measurements and UAV imagery for delineating site-specific management zones in a vineyard is illustrated in Chapter 6 (Ortuani et al., 2019). Finally, conclusions and future perspectives are discussed in Chapter 7.

CHAPTER 2

UAV Remote Sensing for Precision Agriculture

Introducing UAV has represented a revolution in RS techniques for environmental applications, such as PAg. In the last decade, the availability of UAV platforms and ultralight sensors has considerably increased, together with the improvement of computing power and easy to use processing tools (Aasen et al., 2018).

In this Chapter, a brief review on vehicles, sensors, and software packages commonly adopted in UAV RS for PAg applications is presented. In particular, this Chapter focuses on: i) the different types of vehicles suitable for conducting optimal UAV surveys on agricultural areas; ii) the different types of sensors that can be mounted on UAV platforms and are able to collect suitable information on soils and vegetation canopy; iii) the best practices to obtain accurate agricultural data by means of UAV surveys, from survey planning to images processing. Several instruments and methods were directly tested during the PhD work. The review is completed with information mostly taken from some review articles available in the literature, including Tsouros et al. (2019), Aasen et al. (2018), Pádua et al. (2017), Matese et al. (2016), Colomina and Molina (2014), and Salamí et al. (2014).

2.1 Vehicles

UAVs can differ in dimension, shape, flight time and height and payload. In agriculture, the attention of the most of the operators is focused on mini and micro UAV, with weight less than 25 kg. Among them, two main groups of vehicles exist: fixed-wing and multi-rotor, both with different and specific characteristics, advantages and usages. The first type of vehicles planes with wings, while the latter relies on a variable number of propellers. The main conditions that have to be evaluated in order to choose between the two categories, are the dimension and the orography of the area under survey, the desired image resolution (directly dependent on the flight height) and the available space for take-off and landing operations. Fixed-wing UAVs are employed in large areas survey, from 1 to 10 km^2, and allow to collect imagery with ground level resolution in the order of magnitude of decimeters. They need a plane space of about ten square meters for taking-off and landing. On the contrary, multi-rotor vehicles fit to cover areas with dimensions in the range of 0.01 and 1 km^2, with a resolution of acquired data in the order of centimeters and do not need adding space for the take-off and the landing (both vertical). Generally, but not in all cases, in PAg applications the multi-rotors are preferred to fixed-wing vehicles, thanks to their slower flight speed and easiness to operate and maneuver.

The main components of a UAV are the same for both vehicle types, in order to guarantee safe flights. They can be summarized, but not limited, as follows:

- *Ground Control Station*: ground-based computer that can communicate and monitor the UAV;
- *Remote Control*: flight control systems, which control the flight operation;
- *GNSS system*: on board GNSS receiver to define flight route;
- *IMU systems*: Inertial Measurement Unit, composed by accelerometers and gyroscopes to maneuver the UAV;
- *Safety systems*: other miniaturized on board sensors, in order to maintain a safety/minimal distance from obstacles during flights;
- *Payload*: equipment for data acquisition.

A lot of technical solutions are available on the market, for both fixed-wing and multi-rotor UAV, searching from the main commercial labels or from self-made products. Figure 2.1 shows some examples of UAVs, representative for both fixed-wings and multi-rotor vehicles.

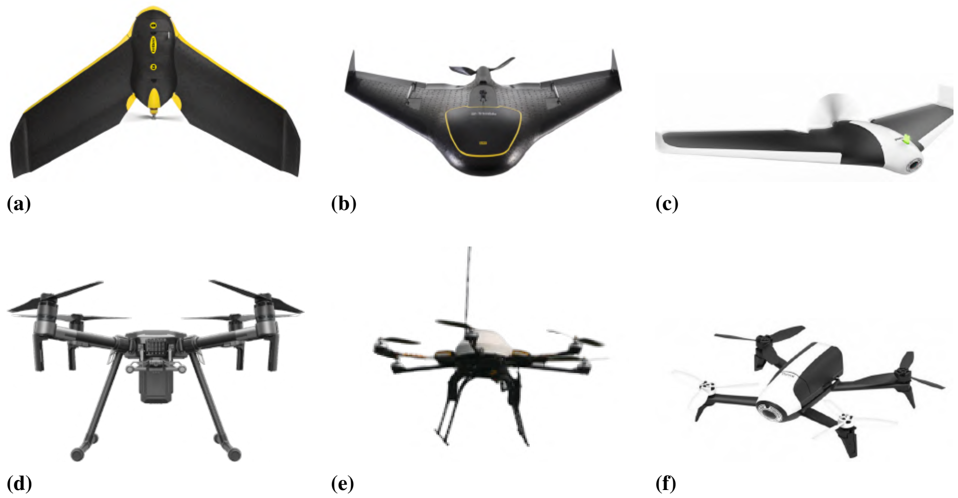

Figure 2.1: *Fixed-wing UAVs: (**a**) SenseFly eBee, (**b**) Trimble UX5, (**c**) Parrot Disco. Multi-rotor UAVs: (**d**) DJI Matrice 210, (**e**) MikroKopter HexaKopter, (**f**) Parrot Bebop 2. Images were taken from manufacturers' websites.*

2.2 Sensors

The main limitation for conducting effective UAV surveys in agriculture is the payload. In the last years, it has been registered a huge growth of low-cost and low-weight sensors, suitable to be mounted on light-weight UAVs. RS sensors are capable to collect defined bands of the electromagnetic (EM) spectrum and return measurements of EM radiation at certain wavelengths. According to the source of energy adopted, two types of sensors can be distinguished: active and passive. The active sensors transmit their own radiation, as pulses, and then detect the radiation reflected back from surfaces. The passive sensors, on the other hand, simply collect the natural radiation reflected and emitted by surfaces, without transmitting their own radiation but exploiting sunlight or artificial lights.

Different solutions are available on the market, both active (Figure 2.2) and passive sensors (Figure 2.3), and the proper device has to be chosen according to final aims of the application. In the following, a general overview is given on the large variety of sensors suitable for UAV RS.

RGB sensors

These sensors operate in the visible (VIS) portion of the EM spectrum, commonly known as light, with wavelengths ranging from 400 to 700 nm. The acronym RGB corresponds to Red-Green-Blue, namely the three spectral bands collected by this type of sensors that originate natural colors images. In some RS applications, RGB images are separated in their original channels and individually used or combined in a false color composite to enhance particular features. These sensors acquire ultra-high resolution imagery, whose processing is usually not particularly hard. RGB sensors are mainly adopted in mapping applications, including 3D modelling and biomass estimation. Despite the advantages, their usage in agriculture is often limited because lots of vegetation parameters cannot be assessed in the VIS but require longer wavelengths, such as Near-InfraRed (NIR) or RedEdge (RE). Some examples of RGB cameras are shown in Figure 2.3a and 2.3b.

CIR sensors

Color InfraRed (CIR) sensors are cameras sensitive also to near infrared wavelengths, approximately ranging from 700 to 1000 nm. Considering the EM spectrum, in the NIR region there is the highest peak of the vegetation reflectance, therefore these sensors are largely diffuse in PAg applications. CIR cameras (Figure 2.3c and 2.3d) are modified RGB cameras, where the infrared filter is removed and substituted with a filter for one of the RGB channels, usually blue channel. In agriculture, they are commonly used for deriving vegetation properties and their usage is often combined with RGB sensors.

Multispectral and hyperspectral sensors

Multispectral sensors are multi-lenses systems, that can capture images in several EM bands simultaneously. The most common sensors are composed from 4 to 10 different lenses and, in addition to R,G,B and NIR channels, usually acquire RE channel, namely the portion of the EM spectrum between red and near-infrared, covering wavelengths around 700 nm. The development of these sensors have significantly increased in recent years and nowadays, different typologies are available on the market, varying from number and types of bands, weight and price. The interest in multispectral sensors has grown among both researchers and farmers, thanks to the high potential of their use for PAg applications, above all for monitoring spatial variability of vegetation vigor. Nevertheless, image processing is complex and various calibration and correction procedures are required in order to obtain reliable information from data acquired by multispectral sensors.

With respect to multispectral sensors, hyperspectral ones have more numerous and narrower spectral bands. Hyperspectral sensors usually capture hundreds of bands in narrow bandwidth. With these sensors, it is possible to retrieve more detailed information on crops and soils and to perform more precise analysis, but their price, still too high, represents an obstacle for their diffusion in PAg. In addition, along with the number of bands, also data processing complexity increases (Adão et al., 2017). Two commonly used multispectral sensors are shown in 2.3e and 2.3f, while in Figure 2.3g an example of hyperspectral sensor.

Thermal sensors

Thermal sensors (Figure 2.3h and 2.3i) are a particular typology of cameras able to detect thermal variability of surfaces. These sensors can collect the radiation emitted by objects in the EM range from 8000 to 14000 nm, the so called TIR (thermal infrared) wavelengths. According to the Planck's Law, the emitted radiation is proportional to objects' temperature, therefore thermal sensors return measurement of surface temperature. In PAg applications, they are typically used to monitor vegetation water stress, often in tandem with other sensors.

LiDAR sensors

Unlike the aforementioned sensors, Light Detection And Ranging (LiDAR) are active sensors (Figure 2.2), able to measure distances from targets. LiDAR data consist of georeferenced 3D point clouds of surfaces, and in vegetated areas, both plants and ground below can be reconstructed. Although their usage is more common in forestry applications, in agriculture LiDAR sensors are adopted for monitoring vegetation growth and biomass estimation. Nowadays, LiDAR suitable for UAV platforms are still very expensive, around tens of thousands of euros, therefore not yet widespread.

(a) (b)

Figure 2.2: *LiDAR sensors: (**a**) LeddarTech VU8, (**b**) Velodyne HDL-32E. Images were taken from manufacturers' websites.*

Figure 2.3: *RGB sensors: (**a**) Canon EOS M10, (**b**) MAPIR Survey2. CIR sensors: (**c**) Tetracam ADC Lite, (**d**) MApir Survey3. Multi/hyper-spectral sensors: (**e**) Parrot Sequoia, (**f**) MAIA WV, (**g**) Headwall Micro-Hyperspec. Thermal sensors: (**h**) Optris PI400, (**i**) FLIR TAU2. Images were taken from manufacturers' websites.*

2.3 UAV surveys

The activities involved in a UAV survey are different and all-important because they may affect the success of the survey itself and the quality of the data acquired. The preliminary phase is the flight-planning. This phase is certainly the most critical one, since it guarantees to operate safety flights and to reduce post-processing times and costs. Starting from shape and size of the area of interest, the characteristics of the sensor, specifically the focal length and the dimensions of the image, and the spatial resolution, namely Ground Sample Distance (GSD) required by the application, it is possible to derive the flight-height and the level of overlapping among images, both forward and side overlap. In agricultural applications, dealing with vegetation imagery is quite onerous, because of the vegetation characteristics that hamper the image matching. In order to face these issues, UAV surveys require to plan the flight before data collections assuming very high values of overlap, respectively at least 80% along flight direction (i.e., longitudinal or forward overlap) and 60% along cross direction (i.e., transversal or side overlap). Nowadays, this phase is conducted in the office by means of a dedicated software, such as Pix4Dcapture or Mission Planner software, after the inspection of the survey area and the definition of the aims of the work. The planning is then transferred to the UAV itself and the flight is carried out autonomously by means of the GNSS and IMU on-board systems (see Section 2.1). During the survey, variables that cannot be considered in the planning phase are meteorological conditions. It is possible to perform flights also under moderate rainy or windy conditions, anyhow, the condition that may mostly affect the survey is sunlight. Illumination conditions should remain homogeneous during the whole acquisition phase, in order to avoid illumination anomalies in the images. In addition, it is advisable to conduct surveys during the central hours of the day, when the sun reaches zenith, to limit the presence of shadows on the ground and minimize the BRDF (Bidirectional Reflectance Distribution Function) effect.

In the survey phase, before data acquisition, calibration of sensors is required, to reduce distortions on image, both geometric and radiometric, and to improve data quality. Geometric corrections are performed by means of panels, namely Ground


(a) (b)

Figure 2.4: *(**a**) Black and yellow panels used as GCPs in a UAV survey with a RGB camera; (**b**) Radiometric calibration targets as visible in a Red channel image.*

Control Points (GCPs), whose geographic coordinates are measured with GNSS systems. These panels, of materials, color and dimension that make them clearly visible by the on-board sensor, operating at the planned height (Figure 2.4a), will be used then in the data processing for georeferencing purposes and for performing camera self-calibration. When working with multi-lenses sensors, GCPs allow to guarantee also high overlapping among images acquired in the diverse spectral channels. As regards radiometry, calibration procedures are necessary, especially when dealing with CIR, multi/hyper-spectral and thermal sensors. Radiometric corrections involve calibration targets, commonly white or gray panel (Figure 2.4b) with known spectral characteristics, used to normalize collected images in relation to illumination conditions and sensor performances. More specifically, calibration panels are adopted to convert pixel values expressed as Digital Numbers (DN) in real reflectance values. Radiometric corrections are particularly recommended in agricultural applications to compare data acquired in different epochs or to produce index maps.

2.4 Data processing

UAV surveys allow to acquire a huge amount of images, with different geometric and spectral characteristics, thus data processing requires specific and methodical techniques. As already discussed in Chapter 1, there is not a standardized workflow for exploiting data collected in agricultural applications. Nevertheless, the common practice involves first the use of photogrammetric techniques in order to geometrically reconstruct the area of interest, then deriving additional features, such as vegetation indices and texture variables, to analyze radiometric characteristics of soils and vegetation, and finally advanced processing, including image segmentation and classification, for retrieving specific information according to application purposes. Data processing main steps are described in the following.

Photogrammetric techniques

As regard geometric processing of UAV imagery, photogrammetric techniques are adopted in order to accurately reconstruct the surveyed area. Photogrammetry consists in defining the position, shape, size and appearance of the objects on the ground, using at least two overlapping images of the objects themselves, taken from different points of view. Considering UAV as platform for images acquisition, several overlapping images are required to cover the entire area of interest and images mosaicking is necessary for 3D area reconstruction. Starting from some points mutually detected on multiple frames, first images are stitched together by means of images matching techniques and then are georeferenced on the coordinates of the GCPs measured during the survey. The main outputs obtainable through photogrammetric techniques are 3D points clouds, Digital Elevation Models (DEMs) and orthophotos. DEMs are digital models representing the altitude of objects. They can be distinguished in Digital Terrain Model (DTM), when referring to the model of the terrain without any objects above it, and Digital Surface Model (DSM), in the case of the model of the heights of all surfaces captured on the images. The orthophoto, on the other hand, is the orthogonal projection on the ground of the mosaic of images, which allows to obtain a scaled representation of reality, without perspective deformations. According to the characteristics of the sensor adopted in the UAV survey, produced orthophotos can be RGB orthophoto, CIR, multi/hyper-spectral or thermal.

Considering the high number of images acquired during UAV surveys, traditional photogrammetric methods have been replaced by algorithms coming from the Computer Vision (CV) world, which are able to process a big amount of images easily and rapidly. In particular all the software used in UAV data processing implement Structure from Motion (SfM). This algorithm allows to generate digital model of the surface of interest, orthophotos and photorealistic 3D reconstructions in assisted or automatic way, even when images blocks acquired by UAV surveys are far from those commonly required for photogrammetric analysis. The main purpose of SfM is to achieve a quick processing and an effective final product, although this includes a loss in the final accuracy and a minor control of the user during the processing steps. Agisoft Metashape (https://www.agisoft.com/), Pix4Dmapper Pro (https://www.pix4d.com/) and MicMac (https://micmac.ensg.eu/index.php/) are photogrammetric software packages dedicated and widely used for UAV imagery processing.

Derived features

Starting from the orthomosaics generated by means of photogrammetric techniques, additional variables can be derived in order to enhance radiometric characteristics of surfaces under survey. Talking about vegetation, a huge improvement can be reached by the use of Vegetation Indices (VIs), computed through mathematical operations among single image channels. VIs allow to synthesize and make easily understandable information derived from each spectral component. According to the sensors adopted during the survey (RGB, CIR, multi/hyper-spectral or thermal sensors), different indices can be calculated by suitably combining the available bands. The mostly used VI is the Normalized Difference Vegetation Index (NDVI), expressed as the difference between the NIR and the Red bands normalized by the sum of these (Rouse Jr et al., 1974). It is generally considered as a proxy of vegetation vigor, because, considering the spectral response of vegetation canopy, a large gap between NIR and Red reflectance values represents a healthy and lush vegetation. The main limitations of using NDVI is that it requires the acquisition of NIR band and cannot be derived from RGB sensors. Another interesting VI is the Crop Water Stress Index (CWSI), used to describe the crop water status and to derive a proxy of crop yield maps, in particular in rainfed environment (Jones et al., 2002). The computation of the CWSI requires the real values of canopy surface temperature, that can be retrieved through an appropriate processing of thermal images generally combined with RGB imagery. In the case studies described in this dissertation, various VIs were adopted, including both RGB-derived and multispectral-derived indices. The VIs employed in each application are properly reported in the respective chapter.

Apart from VIs, other derived variables widespread in remote sensing are texture measures, generated from spatial relationship of pixels. Texture can be defined as the measures of smoothness, coarseness and regularity of an image region (Gonzalez and Woods, 1992). Statistical techniques can be used for the analysis of texture of natural image scenes. The Grey Level Co-occurrence Matrix (GLCM) (Haralick et al., 1973) is computed, counting the occurrence of grey values differences between two pixels at a time, in a single band image. From the GLCM the eight standard Haralick textures can be calculated, namely contrast based features (i.e., contrast, dissimilarity and homogeneity), orderliness based features (i.e., angular second moment and entropy) and statistically based features (i.e., mean, variance and correlation).

Without having to rely on programming languages, many software packages nowadays implement tools for performing simple calculation among rasters. Among those, the most widely used are Geospatial Information System (GIS), both Free and Open Source Software (FOSS), such as QGIS (qgis.osgeo.org) or GRASS (grass.osgeo.org), or commercial software, as ArcGIS (desktop.arcgis.com/en/arcmap), and image analysis software (i.e., ENVI www.harris.com/solution/envi).

Advanced processing

Some image processing techniques are commonly used as a complement of photogrammetry and derived bands computation, in order to address to the specific requirements of the application. In this context, image classification and segmentation are very important in PAg, for vegetation monitoring and mapping. Classification algorithms allow to characterize crop species and identify the presence of weed, while segmentation methods are commonly applied to discriminate objects and extract biophysical parameters. Both approaches are based on remote sensing principles, according to which each surface can be detected by reconstructing its own spectral signature (i.e., surface reflectance as a function of wavelengths). Spectral response of crops and soils can be obtained in a coarser or in a more accurate way, in relation to the number of spectral bands available on the sensor (see Section 2.2).

During image classification, pixels are clusterized according to their radiometric characteristics. This operation can be performed automatically or with the addition of some a-priori information provided by a user. Considering the level of automation of the methods, classification algorithms are divided in *Unsupervised* and *Supervised* methods. Unsupervised algorithms group pixels with similar spectral characteristics into unique clusters according to some statistically determined criteria, while supervised classification is the process of using user defined samples of known informational classes, namely training sets, to classify pixels of unknown identity. Unsupervised methods include K-mean and ISODATA clustering, as well as supervised algorithms comprise Minimum Distance to Mean, Maximum Likelihood and Spectral Angle Mapper classifiers. In addition to the well-known aforementioned methods, in recent years there has been an increase in the use of machine learning techniques in agricultural applications, including in particular Random Forests, Artificial Neural Networks and Support Vector Machine algorithms.

The process of detecting and delineating single features on images is defined as image segmentation. Segmentation methods are mostly used in forestry applications for tree crowns mapping but can be also exploited in agriculture for getting either single plants or single rows information in orchards and vineyards. Starting from simple thresholding algorithms, many examples are available in the literature proposing methodologies for extracting and analysing features of interest on UAV imagery in agriculture.

Advanced processing usually requires a combination of data as input, whether they are geometric, radiometric, original or derived information. Simple algorithms are implemented in GIS and image analysis software, however, it is advisable to create specific processing chains by means of programming languages such as Python (https://www.python.org/), R (https://www.r-project.org/) or Matlab (https://www.mathworks.com/products/matlab.html), in order to fine-tune required parameters and increase the level of automation of processing.

CHAPTER 3

Radiometric consistency of UAV image blocks. – Analysis of Parrot Sequoia datasets

The processing of large datasets that cover areas which need to be acquired by several UAV missions is still a challenging task. As for photogrammetric projects, these types of datasets, composed of various sub-blocks, require a careful assessment of the accuracy of the final products, from both geometric and radiometric points of view. This is even more true when time-series are analyzed; the consistency between data is mandatory in these cases.

While geometry is almost always considered when quality assessment is performed, radiometry is less often investigated but plays a key role in several applications, including precision agriculture (PAg). Although in recent years sensor manufacturers have improved in describing sensor performance and providing tools for performing radiometric corrections (https://forum.developer.parrot.com), the radiometric quality of data is still uncertain. The reliability of spectral information acquired by multispectral sensors mounted on UAVs is not completely clear (BorgognoMondino and Gajetti, 2017). Absolute accuracy might be insufficient for some applications, so that calibration procedures are required (Aasen et al., 2018).

Nowadays equipment vendors are making an effort to supply easy to use HW (Hardware) and SW (Software) so that crop monitoring can be performed by individual farmers. The bundle of Parrot Sequoia (Parrot S.A., Paris, France) and Pix4D (Pix4D S.A., Prilly, Switzerland) is a clear and popular example of this approach.

This case study investigates geometric and radiometric consistency of two overlapping datasets, acquired with Sequoia camera and processed with the bundled software. Geometry was studied to avoid the influence of its inconsistencies on the quality of the radiometry, while radiometry, as well, because it is the main source for agronomic studies. The study site is an area of approximately 36 ha cultivated with rice, in

Pavia province in Northern Italy. Although UAV surveys for PAg typically are multi-temporal, in this study datasets acquired almost at the same time were compared. This is a strength, as the difference assessed in vegetation indices can only be attributable to sensor noise and, possibly, to issues in the radiometric calibration procedure.

The geometric consistency is not assessed by means of a number (generally limited) of check points (CPs), as it is usually done, but by exhaustively evaluating the distance between the whole generated point clouds, with the ICP (Iterative Closest Point) methodology. A dedicated Matlab procedure was specifically developed by colleagues of the University of Pavia (partner of this project), implementing ICP and having some unique features. The geometric consistency is not discussed in this thesis, but it is thoroughly explained in Franzini et al. (2019).

3.1 Materials and methods

3.1.1 Study area and UAV survey

The dataset was acquired with the HEXA-PRO UAV, which is operated by the Laboratory of Geomatics of the University of Pavia and is shown in Figure 3.1a. The vehicle was made by a small Italian company named Restart and has the following main characteristics: 6 engines (290W each one), Arducopter-compliant flight controller, maximum payload of 1.5 kg (partly used by the gimbal, weighting 0.3 kg), flight autonomy of approximately 15 minutes. The UAV was equipped with a Parrot Sequoia camera (see Figure 3.1c). Sequoia has a high-resolution RGB camera with a 4608x3456 pixel sensor, a pixel size of 1.34 μm and a focal length of 4.88 mm; GSD (Ground Sample Distance) is 1.9 cm at 70 m height above ground level (AGL). Sequoia also has four monochrome cameras that are sensitive to the following spectral bands: Green (530-570 nm, G), Red (640-680 nm, R), RedEdge (730-740 nm, RE) and Near-Infrared (770-810 nm, NIR). Their resolution is 1280 x 960, a pixel size of 3.75 μm and a focal length equal to 3.98 mm; GSD is 6.8 cm at the 70 m flying height (AGL), which was adopted for the described survey.

On 13th September 2017, a photogrammetric survey was performed on the Santa Sofia farmstead, near Pavia, Northern Italy (Figure 3.2a). The test-site is a flat area totaling about 36 ha, used exclusively to cultivate rice. The whole acquisition was obtained by five flight missions whose planning is shown in Figure 3.2b, where the optical orthomosaic, used as background, derives from a previous survey. In total, the project is constituted by about 1300 multispectral images, each composed by four bands. The AGL height was 70 m and image overlapping 80% and 60%, along- and across-track, respectively. The Sequoia camera was adopted, as previously mentioned. Twelve markers were placed on the ground and surveyed with the NRTK (Network Real Time Kinematic) GPS mode; VRS (Virtual Reference Station) differential corrections were applied connecting via NTRIP (Networked Transport of RTCM via Internet Protocol) to the GNSS positioning service of "Regione Piemonte and Regione Lombardia" (https://www.spingnss.it/spiderweb/frmIndex.aspx). GCPs coordinates have a planimetric and altimetric accuracy of 2-3 cm and 4-5 cm, respectively. GCPs were constituted by artificial markers having a black and gray diamond shape (Figure 3.1d); markers position is illustrated in Figure 3.2b. At the beginning of each flight, the recommended radiometric calibration procedure was performed by acquiring the calibration

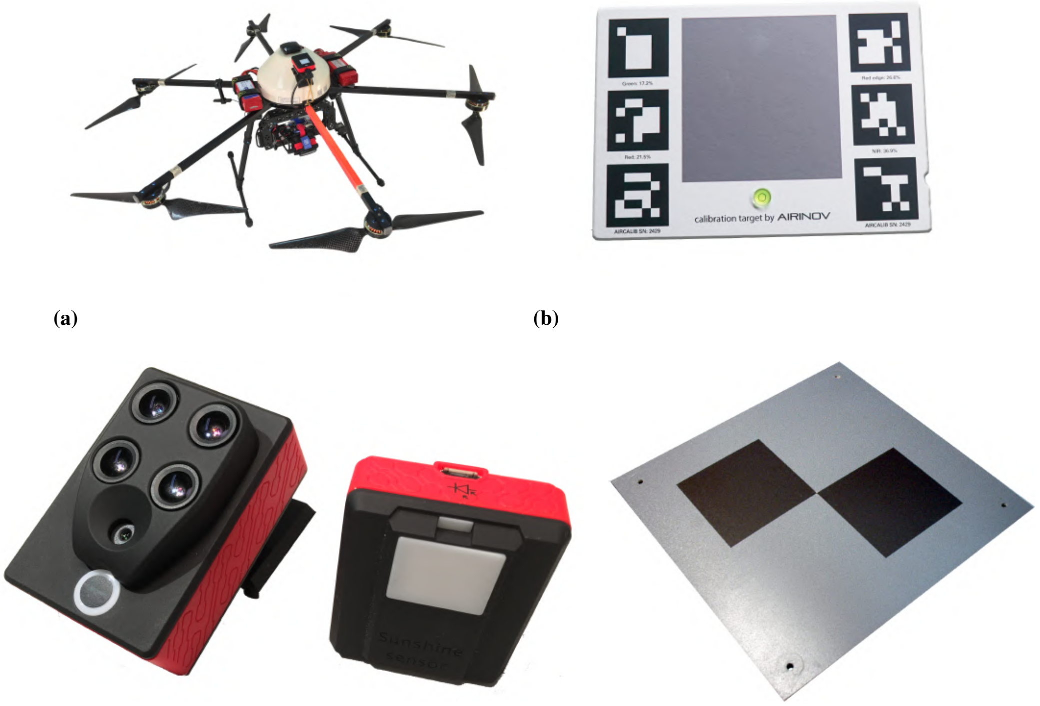

(a) (b) (c) (d)

Figure 3.1: *The equipment operated by the Laboratory of Geomatics of the University of Pavia:* ***a)*** *The HEXA-PRO UAV used for the survey;* ***b)*** *The Airinov calibration target supplied with the camera;* ***c)*** *The Parrot Sequoia camera: the imaging and irradiance sensors are shown;* ***d)*** *An example of the used artificial markers.*

target (Figure 3.1b).

The present work will only focus on flights 3 and 4, as these had a methodological purpose. The overlapping area allowed to deeply analyze geometric and radiometric congruency under several processing scenarios (as described in Section 3.1.2), because it is quite wide (23 ha) and encompasses 4 GCPs (Ground Control Points).

3.1.2 Photogrammetric processing

The photogrammetric project was carried out with Pix4Dmapper Pro, ver. 4.4.9. Only the four multispectral channels were considered, having 6.8 cm GSD; higher resolution RGB imagery was disregarded, as it is recorded in the JPEG format with a high compression factor and has low quality, compared to photogrammetry requirements. The processing followed the usual pipeline (Ronchetti et al., 2018): images alignment, tie points extraction, manual measurement of CPs and GCPs, bundle block adjustment (BBA), generation of dense point clouds, Digital Surface Model (DSM), orthomosaic and reflectance maps. The software allows to use only one set of calibration target images per project, so the photogrammetic processing followed a single-block approach. Four scenarios were depictedbased on georeferentiation methodology and radiometric processing:

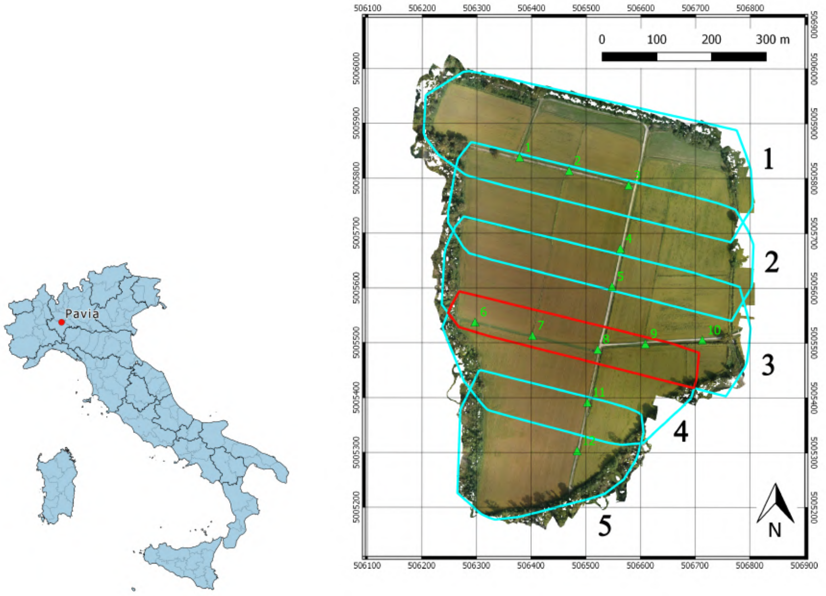

(a) (b)

Figure 3.2: *UAV survey framework:* ***(a)*** *Site location in Italy;* ***(b)*** *The sub-blocks composition: light blue lines represent the flight outlines where the overlapping areas are clearly visible. The one considered in the paper is highlighted in red and includes four GCPs named 6, 7, 8 and 9. GCPs locations are reported with green triangles. Coordinate Reference System (CRS): WGS84/UTM 32N. Central coordinates (E, N): 506500, 5005600.*

1. Direct georeferencing (DG) scenario: no GCPs were inserted in BBA and each sub-block was processed by direct photogrammetry using positions coming for the Sequoia integrated GPS receiver. Scenario A will be used only in geometric assessment.

2. Independent georeferentiation/independent radiometric processing (Ig/Ir) scenario: the two blocks were independently processed in terms of geometry and radiometry. Scenario B will be used both in geometric and radiometric assessment.

3. Independent georeferentiation/joint radiometric processing (Ig/Jr) scenario: this scenario is a variation of the previous one in which orientation parameters were computed for each block independently, as in the second scenario, but the two flights were then merged for dense point cloud and reflectance maps generation. This scenario coincides with the so-called “merge option” in Pix4Dmapper software, and it is the recommended procedure for processing photogrammetric blocks with a large number of images and an overlapping area. It should ensure that radiometric differences caused by a misalignment in the dense point clouds are avoided. Scenario Ig/Jr was used only in radiometric assessment.

4. Joint georeferentiation/independent radiometric processing (Jg/Ir) scenario: the two blocks were jointly orientated, and the obtained exterior orientation parameters were then transferred to a single-block project for generation of dense point clouds and reflectance maps. In this scenario, possible radiometric inconsistencies due to separate computation of interior and exterior orientation parameters

are eliminated. This scenario was used in both geometric and radiometric assessment.

Bundle block adjustment and dense point cloud generation

The bundle block adjustment parameters were set according to the described scenario, since they differ in terms of calibration method and camera optimization. In DG scenario, the calibration method was set to the “alternative” option. This choice is recommended when the surveyed area is flat (as in this case) and there is availability of good image geolocation; for the Sequoia sensor, the used geolocation comes from the on-board GPS receiver, even if its quality is low, as discussed before. For camera optimization, external parameters were all re-estimated, while for the internal ones they were adopted from the camera model that is delivered by Sequoia directly into the EXIF (Exchangeable image file) section of each image. As we knew from the Pix4D technical support, the parameters delivered into the EXIF are individually determined for each item at the factory. Their reliability is good, as reported in (Fernández-Guisuraga et al., 2018), in which the changes between nominal and optimized camera parameters were as low as 0.01%. In Ig/Ir and Ig/Jr scenarios, the calibration method was again set to “alternative”. For camera optimization, since the GCPs were imported and measured on each of the two blocks, both external and internal parameters were optimized. Finally, Jg/Ir is a two-step scenario in which the two blocks were jointly processed, and so the obtained internal and external parameters were used to separately generate the dense point clouds for each block. For the first step (image orientation), the parameters were set as equal to Ig/Ir; for the second step (single-block dense point cloud generation), the calibration method was set to geolocation-based, since accurate positioning and orientation are available from the first step. Besides, in this case, neither interior nor external parameters were optimized because they were directly imported in the first step of the project.

All dense point cloud generation was performed adopting the default options: *Half Image Size* resolution images, point density was set on *Optimal* and a cloud point was accepted only if positively matched in at least three images. The average density is between 11 to 14 points per m^3. In a preliminary test, the *Original Image Size* resolution was evaluated too, but higher point density did not significantly improve the orthophotos and reflectance maps generation; the requirements of precise agriculture are lower in comparison to other applications, such as 3D mapping, and the obtained resolution was considered enough for the research aims.

Orthophoto and reflectance maps generation

Pix4Dmapper allows to generate orthophoto and reflectance maps during step 3 of the processing, together with the computation of the DSM. In this study, products were generated with GSD equal to 0.10 m and project settings were maintained the same for the considered scenarios.

Reflectance maps were generated by setting, in the *Radiometric Processing and Calibration* panel, *Camera and Sun Irradiance* correction. It allows to apply corrections to the camera parameters stored in the image metadata (i.e. vignetting, dark current, ISO), as well as for the sun irradiance information, acquired with the proper sensor (see Figure 3.1c). Images of the calibration target are required for performing corrections.

Hence, during the survey, the prescribed radiometric calibration procedure of the Parrot Sequoia camera was performed and the suitable calibration target (see Figure 3.1b) was imaged several times, with different exposure time. Acquisitions were taken at the beginning of each flight, so that different calibration data were stored for each flight, ensuring similar sky and illumination conditions between calibration images and flight images.

For the *Radiometric Processing and Calibration*, calibration images with the highest value of exposure time were retained and the software automatically detected target on them defining the proper reflectance values for each spectral band that are equal to 0.172, 0.215, 0.266 and 0.369, respectively for Green, Red, RedEdge and NIR.

3.1.3 Radiometric consistency assessment

Radiometric consistency was assessed by computing, pixel by pixel, differences for the co-registered reflectance maps in the overlapping area of photogrammetric blocks 3 and 4. Respective statistics were also analyzed. Considering that Sequoia is a sensor mainly dedicated to agricultural applications, assessment was conducted also for some vegetation index (VI) maps, since they commonly represent a proxy of vegetation parameters to be used for agronomy purposes. VI maps were computed in Matlab, by applying an index formula to proper reflectance maps (Table 3.1).

Table 3.1: *Vegetation Indices (VIs) used in this study.*

Index	Name	Formula	References
NDVI	Normalized Difference Vegetation Index	$\frac{Nir-Red}{Nir+Red}$	Rouse Jr et al. (1974)
GNDVI	Green Normalized Difference Vegetation Index	$\frac{Nir-Green}{Nir+Green}$	Gitelson et al. (1996)
NDRE	Normalized Difference RedEdge Index	$\frac{Nir-RedEdge}{Nir+RedEdge}$	Barnes et al. (2000)
NDVIre	RedEdge Normalized Difference Vegetation Index	$\frac{RedEdge-Red}{RedEdge+Red}$	Gitelson and Merzlyak (1994)
NGRDI	Normalized Green Red Difference Index	$\frac{Green-Red}{Green+Red}$	Gitelson et al. (2002)

For Ig/Ir and Jg/Ir scenarios, maps derived from blocks 3 and 4 were directly compared, while Ig/Jr scenario was checked with respect to the single blocks of Ig/Ir scenario (see Section 3.1.2 for more details about scenario characteristics). From here on, maps are identified with the names “3 Ig/Ir”, “4 Ig/Ir”, “3 Jg/Ir”, “4 Jg/Ir”, “Ig/Jr”, where “3” stands for block 3, and “4” for block 4. DG scenario was not considered for radiometric assessment.

Moreover, since no ground truth was available, the reliability of reflectance and VI maps was evaluated by comparing maps with the one obtained from Sentinel-2 (S2) imagery. Indeed, a Sentinel-2 acquisition two days after the survey (September 19, 2017) was available. Maps derived from the photogrammetric blocks (having a GSD equal to 0.10 m) were upscaled with a nearest-neighbor resampling to 10 m spatial resolution, to match Sentinel-2 imagery resolution. Correlation analysis was applied and statistics were performed on differences in terms of single bands and radiometric indices.

Although a comparison with ground truths calculated with spectroradiometer would have been more effective, a test on compatibility between Sequoia and S2 data is also of scientific relevance, given the growing interest in the integration of data acquired from satellite and UAV platform for environmental applications (Puliti et al., 2018, Dash et al., 2018), including PAg (Matese et al., 2015, Khaliq et al., 2019, Zhang et al., 2019b), both from research and applicative point of view.

3.2 Results

Radiometric consistency was assessed by estimating differences pixel by pixel among corresponding reflectance and VIs maps, in the overlapping area. Results are reported in Section 3.2.1. Moreover, the test on the compatibility of Sequoia maps with Sentinel-2 imagery, performed by means of correlation analysis, is presented in Section 3.2.2.

3.2.1 Assessment of the differences between overlapping blocks

For the three processing scenarios, differences were calculated pixel by pixel among corresponding reflectance and VI maps in the overlapping area. While Ig/Ir and Jg/Ir scenarios were independently evaluated, Ig/Jr scenario was compared to the single blocks of Ig/Ir scenario (see Section 3.1.3). Descriptive statistics for differences calculated on reflectance maps are shown in Table 3.4, and results of VIs maps are reported in Table 3.2, as well as results on VIs maps are reported in Table 3.3. Although differences have similar ranges, it is important to remember that reflectance maps have values in the range [0, 1], while values for VIs maps are in the range [-1, 1].

The computed RMSE values are quite close to zero for all cases, but significant differences among single reflectance maps and VI maps can be stressed, considering minimum and maximum absolute values. In particular, differences with maximum and minimum values above 0.4 are calculated for the NIR maps, differences reach values close to 0.3 for the red-edge map, and lower values are registered for the green and red maps, with minimum and maximum absolute values below 0.2 for the red maps in some cases. A similar behavior is also evident for the VI maps, where the differences calculated on NDVI maps assume lower RMSE values, while maximum and minimum values even greater than 0.5 are calculated for many VIs. The comparison between the statistics computed for Ig/Ir and Jg/Ir scenarios shows that both reflectance and VI map differences reach very similar values.

To assess the significance of the calculated values, the differences are presented in the form of box and whisker plots. Figure 3.3 reports box and whisker plots for differences computed on reflectance maps, while in Figure 3.4 VIs results are shown. The plots do not refer to the Jg/Ir scenario, as similar results are obtained with respect to Ig/Ir scenario.

Table 3.2: *Summary statistics of the differences between reflectance maps in the overlapping area.*

		Green	**Red**	**RedEdge**	**Nir**
3 Ig/Ir-4 Ig/Ir	min	-0.1923	-0.1640	-0.2957	-0.5217
	max	0.2822	0.2194	0.4168	0.5931
	mean	0.0088	-0.0013	0.0268	0.0368
	std	0.0572	0.0272	0.0367	0.1103
	rmse	0.0579	0.0272	0.0454	0.1163
3 Ig/Ir-Ig/Jr	min	-0.0947	-0.1042	-0.2336	-0.3432
	max	0.2538	0.1763	0.3557	0.6642
	mean	0.0166	0.0061	0.0182	0.0482
	std	0.0305	0.0131	0.0208	0.0692
	rmse	0.0348	0.0144	0.0276	0.0843
4 Ig/Ir-Ig/Jr	min	-0.1791	-0.1964	-0.3547	-0.3863
	max	0.1915	0.1696	0.2769	0.5047
	mean	0.0079	0.0075	-0.0086	0.0115
	std	0.0338	0.0195	0.0213	0.0613
	rmse	0.0347	0.0208	0.0230	0.0624
3 Jg/Ir-4 Jg/Ir	min	-0.1826	-0.1761	-0.3217	-0.5519
	max	0.2670	0.1874	0.4511	0.5831
	mean	0.0087	-0.0014	0.0270	0.0365
	std	0.0572	0.0276	0.0446	0.1104
	rmse	0.0579	0.0277	0.0522	0.1163

Table 3.3: *Summary statistics of the differences between VIs maps in the overlapping area.*

		NDVI	**GNDVI**	**NDRE**	**NDVIre**	**NGRDI**
3 Ig/Ir-4 Ig/Ir	min	-0.4431	-0.3859	-0.2651	-0.5629	-0.4726
	max	0.4749	0.5066	0.3567	0.4930	0.6011
	mean	0.0293	0.0064	-0.0003	0.0361	0.0392
	std	0.0242	0.0678	0.0767	0.0616	0.0910
	rmse	0.0380	0.0681	0.0767	0.0714	0.0991
3 Ig/Ir-Ig/Jr	min	-0.3822	-0.2891	-0.2033	-0.4939	-0.3508
	max	0.5734	0.5924	0.4426	0.4208	0.4884
	mean	0.0142	-0.0012	0.0248	-0.0008	0.0245
	std	0.0183	0.0310	0.0513	0.0311	0.0538
	rmse	0.0232	0.0310	0.0570	0.0311	0.0591
4 Ig/Ir-Ig/Jr	min	-0.2675	-0.2200	-0.2502	-0.400	-0.5166
	max	0.3856	0.3130	0.3924	0.4575	0.3907
	mean	-0.0151	-0.0077	0.0252	-0.0370	-0.0146
	std	0.0208	0.0450	0.0418	0.0467	0.0481
	rmse	0.0257	0.0457	0.0488	0.0596	0.0503
3 Jg/Ir-4 Jg/Ir	min	-0.4354	-0.3559	-0.4354	-0.6301	-0.4934
	max	0.5024	0.5452	0.7340	0.6121	0.6811
	mean	0.0293	0.0062	0.0003	0.0359	0.0394
	std	0.0271	0.0689	0.0861	0.0688	0.0942
	rmse	0.0400	0.0691	0.0861	0.0775	0.1021

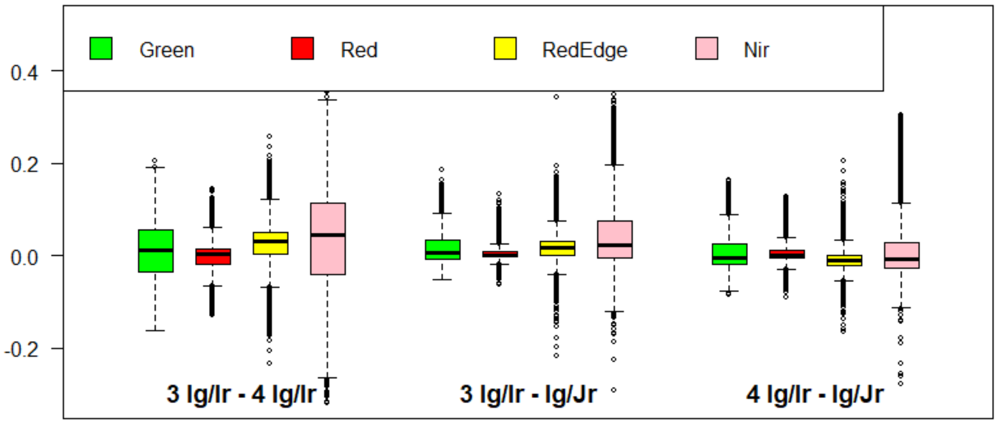

Figure 3.3: *Box and whisker plots of differences computed on different reflectance maps in the overlapping area.*

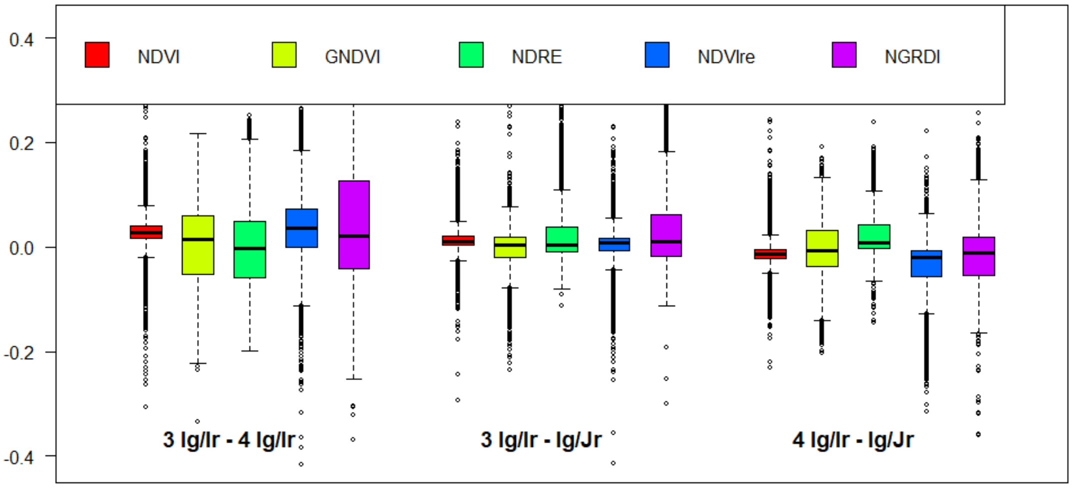

Figure 3.4: *Box and whisker plots of differences computed on different VIs maps in the overlapping area.*

From the plots it is evident that results vary from map to map, but few general considerations can be drawn. Median values are overall around 0, while maximum and minimum values are outside of the confidence intervals and can be considered as outliers. For most cases, the variability of the differences is contained in the range [-0.2, 0.2]; thus, this interval of values is retained as significant for further analysis. The VIs can mitigate the effects of single reflectance maps, specifically the high differences registered for NIR maps are rather compensated in the NDVI maps. Moreover, with respect to the differences computed between single blocks (i.e., 3 Ig/Ir-4 Ig/Ir), results obtained considering Ig/Jr scenario (i.e., 3 Ig/Ir-Ig/Jr and 4 Ig/Ir-Ig/Jr) have narrower confidence intervals.

Spatial distribution of the differences in the overlapping area is shown in Figure 3.5, Figure 3.6 and Figure 3.7. For the sake of brevity, only the most significative results are presented. As a matter of fact, similar results were registered for Ig/Ir and Jg/Ir scenarios. As regarding Ig/Jr scenario, green, NIR, and NDVI maps are shown, since the other maps have a similar spatial behavior.

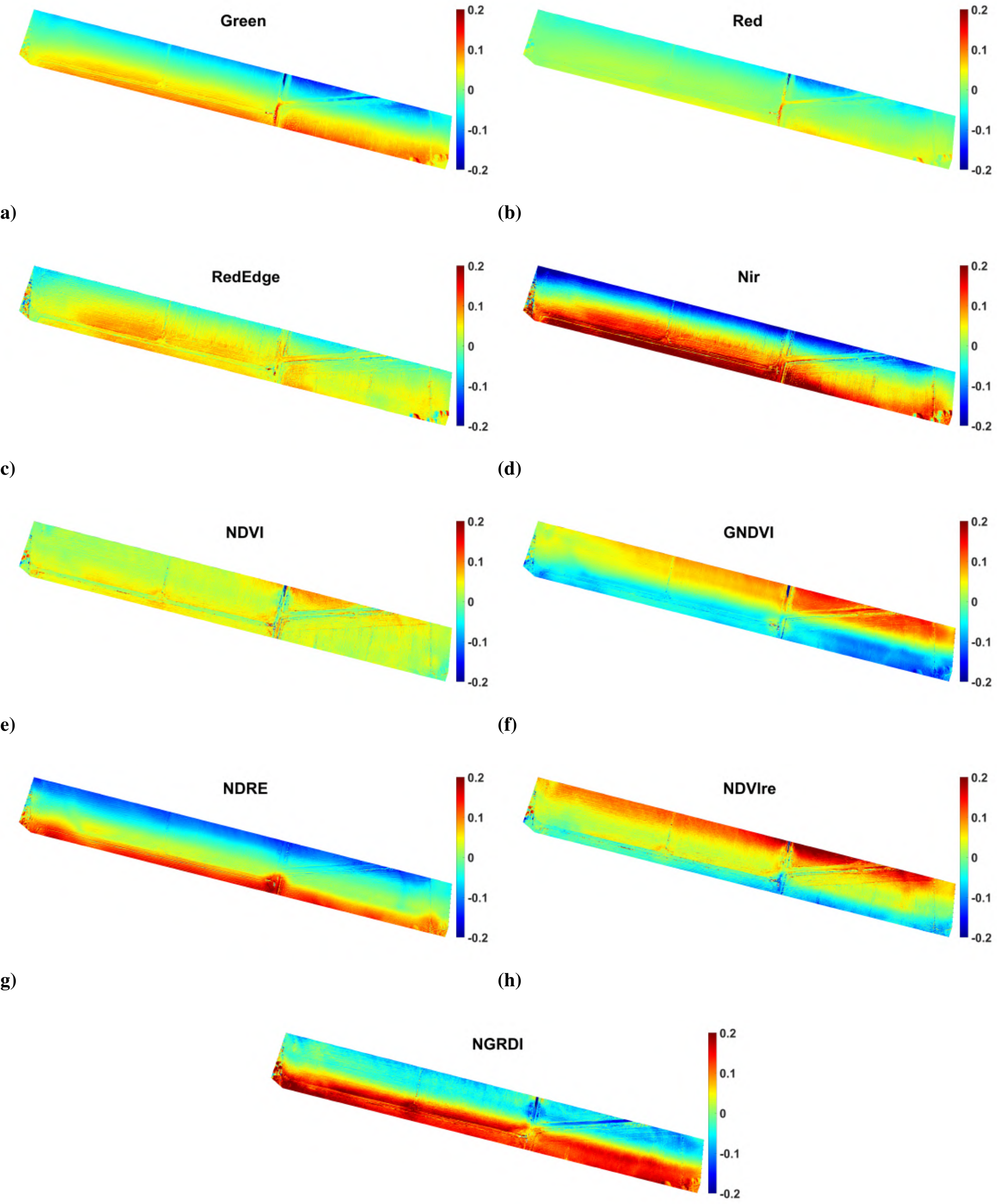

(a) (b) (c) (d) (e) (f) (g) (h) (i)

Figure 3.5: *Spatial distribution of differences in the overlapping area. Ig/Ir scenario: Green **(a)**, Red **(b)**, RedEdge **(c)**, Nir **(d)**, NDVI **(e)**, GNDVI **(f)**, NDRE **(g)**, NDVIre **(h)**, NGRDI **(i)**.*

A clear spatial pattern can be noted from the plots-the reflectance values tend to be overestimated as moving away from the center of the block (i.e., approaching the borders of the block); an analogous effect is visible in VI difference maps. This effect

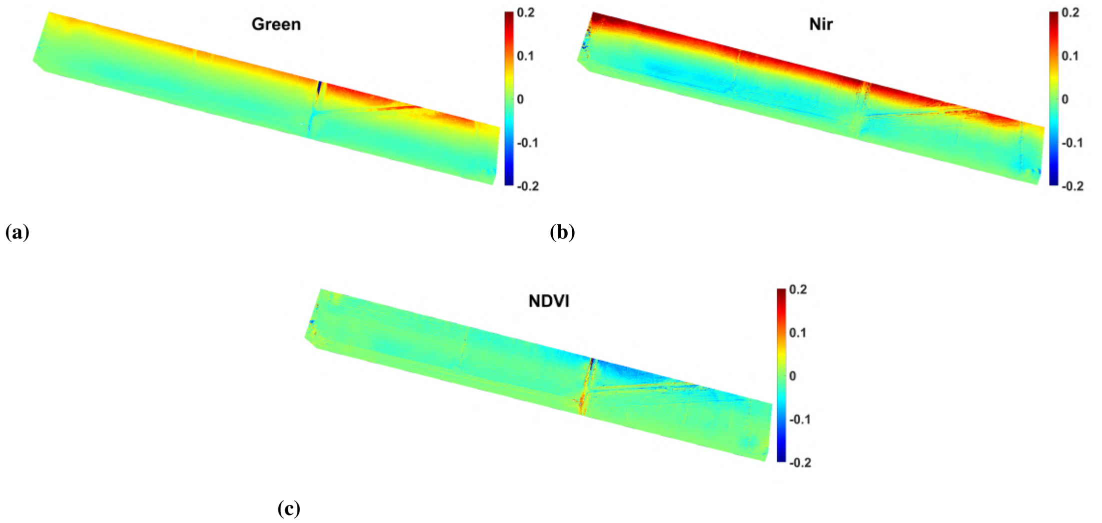

(a) (b)

(c)

Figure 3.6: *Spatial distribution of differences in the overlapping area for Ig/Jr scenario, with respect to block 3: Green* ***(a)****, Nir* ***(b)****, NDVI* ***(c)****.*

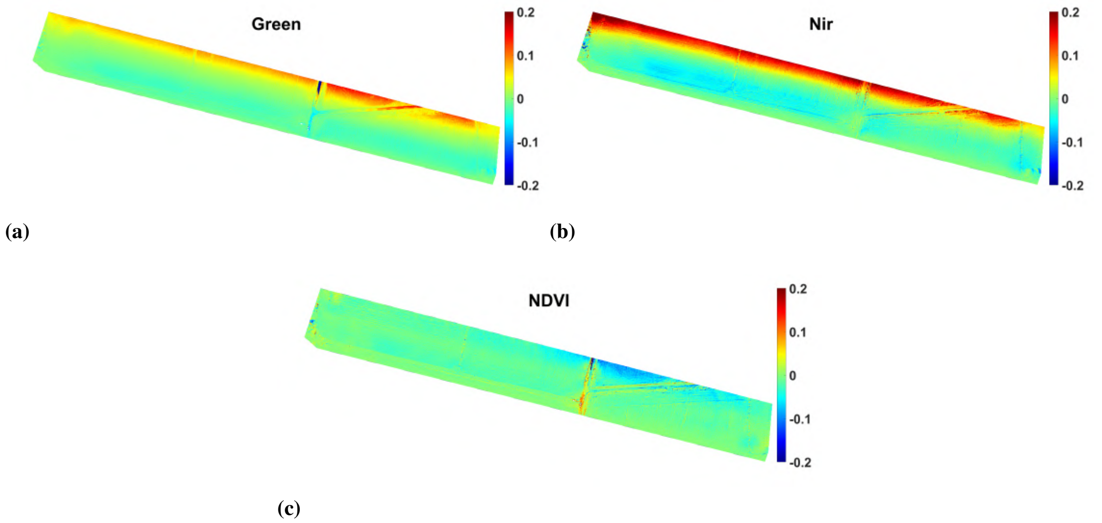

(a) (b)

(c)

Figure 3.7: *Spatial distribution of differences in the overlapping area for Ig/Jr scenario, with respect to block 4: Green* ***(a)****, Nir* ***(b)****, NDVI* ***(c)****.*

is more evident considering the differences calculated between the single blocks of Ig/Ir scenario (Figure 3.5), it is less evident when introducing also Ig/Jr scenario (Figure 3.6 and 3.7). No difference or very small differences are found in NDVI maps for all considered cases, which are uniformly distributed with no specific spatial profile in the overlapping area of blocks 3 and 4.

3.2.2 Comparison with Sentinel-2 imagery

As described in Section 3.1.3, the reliability of Sequoia maps was assessed with respect to Sentinel-2 data to evaluate the feasibility of data integration. First, an upscaling of maps derived from Sequoia imagery was required, then correlation analysis was computed (N = 265 samples). Results for the correlation analysis are reported in Figure 3.8 and maps statistics are summarized in Table 3.4. For the sake of brevity, only results for NDVI are shown. As a matter of fact, other studies are present in the literature focusing on the comparison of NDVI only (Khaliq et al., 2019, Zhang et al., 2019b). Rmse values reported in Table 3.4 were calculated by considering NDVI map from S2 imagery as reference.

Table 3.4: *Summary statistics of the NDVI maps computed from S2 imagery and Sequoia imagery, in the overlapping area.*

		S2	**3 Ig/Ir**	**4 Ig/Ir**	**Ig/Jr**
NDVI	min	0.3197	0.0998	0.0764	0.0221
	max	0.7787	0.8731	0.8926	0.8946
	mean	0.5583	0.6262	0.5945	0.6119
	std	0.0906	0.1323	0.1331	0.1324
	rmse	–	0.1140	0.0984	0.1090

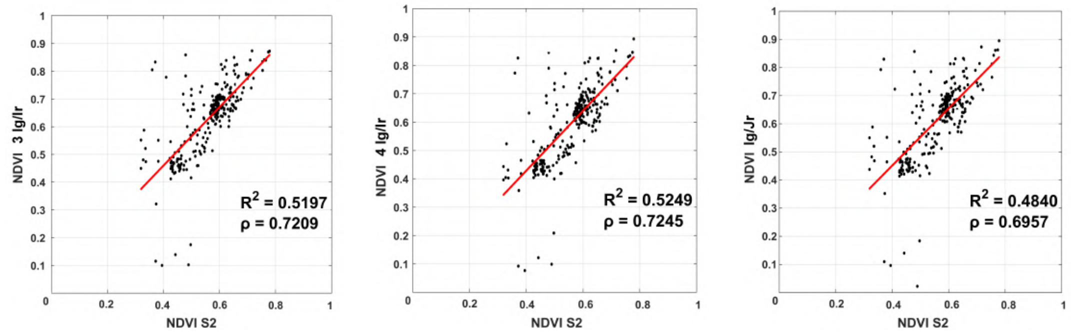

(a) (b) (c)

Figure 3.8: *Scatter plot and regression line for NDVI maps computed on S2 imagery as respect to Sequoia imagery: 3 Ig/Ir **(a)**, 4 Ig/Ir **(b)**, Ig/Jr **(c)**. For each graph, the coefficient of determination (R^2) and the Pearson's correlation coefficients (ρ) are reported (p–value $< 2.2x10^{-16}$).*

The correlation with NDVI map from S2 imagery shows a good correspondence: coefficients of determination are 0.5197 for 3 Ig/Ir, 0.5249 for 4 Ig/Ir, and 0.4840 for Ig/Jr. The NDVI map with the highest correspondence against S2 imagery is the one derived from 4 Ig/Ir data, with Pearson's correlation coefficient ρ and rmse equal to 0.7245 and 0.0984, respectively. Nevertheless, the regression lines show a slight overestimate of Sequoia data compared to S2; NDVI maps from Sequoia imagery report higher values with respect to the S2 map (as also summarized by higher values for max and mean in Table 3.4) and cover wider ranges (lower values for min and higher values for std in Table 3.4).

3.3 Discussion

As already stressed by many authors in the literature (Guo et al., 2019, Mafanya et al., 2018, Honkavaara and Khoramshahi, 2018, Iqbal et al., 2018), radiometric corrections are necessary when using sensors mounted on UAV for PAg, but the ease of use and diffusion is limited. The radiometric processing available in Pix4Dmapper software for the Sequoia camera provides most of the corrections, including vignetting, dark current, exposure time, and sunlight irradiance, but omits other possible causes of radiometric variations (Tu et al., 2018). First, this research points out that radiometric inconsistencies due to differences in the acquisition geometry remain unsolved. Reflectance values of pixels at the borders of the blocks tend to be overestimated, as a consequence of the inclination of the point of view during the photogrammetric survey. From Figure 3.5, it is evident that differences are not uniformly distributed, but present a clear spatial pattern. Higher difference values (absolute values) are measured at the borders of the overlapping area, while the lowest values approach the center of the area. This demonstrates the presence of a high edge effect on the reflectance maps, which must be considered during flights planning. In practical use, it is advisable to plan UAV surveys covering an area wider than the one of interest. Enlarging the survey area should guarantee uniformity in the acquisition geometry even in the edges, otherwise characterized by non-negligible radiometric distortions.

Radiometric differences are not affected by different geometric processing of the blocks, as confirmed by the similar values of the differences computed for Ig/Ir and Jg/Ir scenarios for both reflectance and VI maps (Table 3.2 and Table 3.3).
As can be noted from rmse values reported in the tables, differences calculated for some VI maps are lower than values obtained for reflectance maps, meaning that some indices can decrease inconsistencies of single reflectance bands (Stow et al., 2019).

Considering the Ig/Jr scenario, the differences are moderate with respect to Ig/Ir scenario for both reflectance and VI maps, with mean values overall close to zero. The edge effect is also still evident from the spatial distributions shown in Figure 3.6 and Figure 3.7, however with lower values, as is evident in the box plots in Figure 3.3 and Figure 3.4. As a matter of fact, it should be recalled that the Ig/Jr scenario corresponds to the procedure recommended by Pix4Dmapper software to process large photogrammetric blocks. For adjacent blocks acquired with separate but temporally close flights, the recommended merging option can partially correct the effect of illumination geometry and mitigate radiometric inconsistencies in the overlapping areas between blocks.

There are still uncertainties regarding the obtained absolute values of reflectance and for the derived indices (González-Piqueras et al., 2018), and consequently in the quantitative use of the Sequoia data for the possible calculation of biophysical parameters. From the results reported in this study, it should be noted that in some areas, differences have values close or even larger than 0.2 (absolute value). Therefore, the different processing scenarios have an impact on the results in terms of radiometry. A difference of this magnitude cannot be neglected in the operational phase for precision agriculture applications; even more so if used for multitemporal surveys. As a matter of fact, the map that shows the most homogeneous values in all cases is NDVI, which is widely used in most agriculture applications (Teal et al., 2006, Katsigiannis et al., 2016, Freidenreich et al., 2019).

Regarding the comparison with S2, which is limited in this paper to NDVI, it should be mentioned that despite the analysis being affected by the different geometric resolutions of sensors and acquisition platforms, a significative correlation is found between Sequoia and S2 maps. Following the approach of Khaliq et al. (2019), the Pearson's correlation coefficient can be adopted as a map similarity measure. The obtained coefficients, which are close to 0.7, prove a coherence between the data collected from the different platforms and show similar spatial variability values of NDVI maps, which are to be interpreted as the same behavior in terms of crop vigor (Di Gennaro et al., 2019). Therefore, the compatibility and integration of NDVI maps obtained by Sequoia and Pix4D systems should be feasible along with the Sentinel-2 products.

3.4 Conclusions

Even though producers and developers have made great efforts to enhance them, radiometric corrections leave significant radiometric distortions in orthomosaics obtained by Sequoia and Pix4D systems, which can result in biased absolute values. This study shows that relevant differences are found depending on flight geometry and block processing choices, with differences that can reach 20% of pixel values for single reflectance bands or VIs, thus reducing the effective use in PAg. Moreover, available radiometric corrections do not guarantee uniform accuracy and consistency of results, and this can cause difficulties in comparing surveys carried out on different lightening conditions. Careful planning of the survey, together with proper choices of image processing, can enhance the results. Very high image overlap yields uniformity over a single block, and edge distortions can be reduced by surveying a wider area that includes the study area. Carrying out double grid flights has not been addressed in this case study, but it could be an alternative to reduce edge effects.

Nevertheless, for large surveys that imply the acquisition and processing of separated sub-blocks, the merge option suggested by Pix4D is effective in reducing radiometric inconsistencies in adjacent areas. This fact, together with the high correlation found with S2 products, proves that Sequoia is suitable for agronomic purposes, but great attention must be paid to the planning of the survey and to the data processing.

Therefore, it is necessary to increase the awareness in the use of sensors and semi-automatic data processing to deeply understand the strengths and weaknesses of UAV usage for PAg. In this study, the choice to process the dataset following the proposed scenarios instead of a standard workflow was driven by the apparently impossibility of attributing the corresponding calibration set of images to each block. The new Sequoia+ sensor should bypass this issue because no calibration target is needed; imagery processing exploits a new fully automatic calibration pipeline in Pix4D.

Finally, the applicability of the proposed method can be extended. In this paper, geometric and radiometric consistency was evaluated comparing results obtained from two almost contemporaneous flights, processed following a single-block approach. The same method can be used to evaluate consistency between two or more blocks acquired days or month apart; in other words, the method can be used to assess time-series.

CHAPTER 4

DTM generation with mass-market UAV. – Using a fisheye camera on a vineyard

Precision agriculture (PAg) recommends a sustainable employment of nutrients and water, according to the site-specific crop requirements. In this context, the knowledge of soil characteristics allows to appropriately manage resources, reducing the financial and environmental commitment. Also the topography can influence soil water condition, because elevation differences control the spatial distribution of water on a field (Schmidt and Persson, 2003). The Topographic Wetness Index (TWI), based on the local slope (Sörensen et al., 2006), for example, is a reliable indicator of how topography influences the movement of water and consequently the soil moisture content.

The Digital Terrain Model (DTM) describes the topography in a discrete way, with a given resolution and accuracy, and allows deriving TWI maps (Silva et al., 2014). Moreover, in agriculture applications, the crop growth can be monitored from DTM and Digital Surface Model (DSM), by extracting the Canopy Height Model (CHM), computed as filtered difference of surface and terrain heights (Zarco-Tejada et al., 2014). The level of detail of the spatial analysis can be extracted according to the spatial resolution of the DTM. Therefore, the generation of high-resolution terrain models has great relevance in agriculture.

This case study focuses on the production of high resolution DTM in agriculture by photogrammetric processing with a mass market very light UAV, the Parrot Bebop 2. Particular attention is given to the data processing procedures and to the assessment of the quality of the results. An experimental test has been carried out on a vineyard located in Monzambano, Northern Italy. The interest in the use of small consumer UAV for photogrammetric applications is constantly increasing and more and more often these systems are equipped with fisheye lenses. These cameras are characterized by short focal lengths, coupled with a wide field of view, which requires a non-classical projection model (Perfetti et al., 2017; Kannala and Brandt, 2006). These lenses were firstly embedded in UAV systems mainly for entertainment purposes. However, their use for 3D reconstruction of cultural heritage sites, as well as for precision agriculture applications, has widespread, mainly because of the low-cost, high manoeuvrability and easiness of use of such platforms.

4.1 Materials and methods

4.1.1 Study area and UAV survey

A vineyard located in Olfino di Monzambano (province of Mantova), Northern Italy, has been chosen as study area. It covers about one hectare at the Colombara Farm. The study site is shown in Figure 4.1.

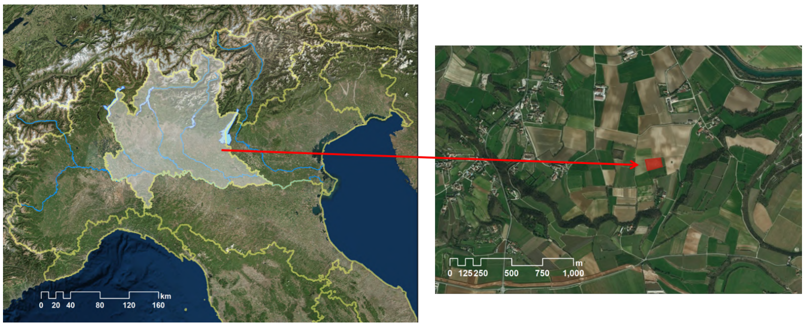

Figure 4.1: *The Monzambano vineyard location: on the left, the Northern Italy centered on Lombardy region (filled in white) where Monzambano is located; on the right, a detailed zoom on vineyard location. Map data: ©Google Satellite.*

The survey has been conducted using a Parrot Bebop 2, a small lightweight and low-cost quadcopter. It is equipped with 14 Mpx fisheye camera, installed with a fixed inclination of 30°. The use of oblique images acquired with these kind of cameras could be very challenging for commercial photogrammetric software packages. Nevertheless, the wide field of view and the tilt angle of the camera can give advantages in agriculture applications because it is possible to investigate the crop not only from nadiral direction, but even from a lateral point of view, to monitor the development of vegetation. The used UAV is characterized by easiness of use and control. It can resist headwinds up to 60 km/h and its flight is quite stable, thanks to the number of sensors installed onboard (namely pressure and ultrasound sensors, GNSS chipset, 3-axis accelerometer, 3-axis magnetometer and 3-axis gyroscope). It can be completely remotely controlled via Wi-Fi connection using a tablet or a smartphone and the flight can be easily planned using the Pix4D Capture App. Because of its low weight, this platform can guarantee a flight autonomy up to 25 minutes.

Consumer UAVs, such as the Bebop 2, are equipped with cameras that delivers high quality images, however the use of fisheye lenses for photogrammetric purposes requires a number of specific attentions because the mapping between object and image points is very different from the one that characterize rectilinear images. Because of that, the classical pinhole camera model cannot be used and different optical projections have to be consider (Perfetti et al., 2017, Barazzetti et al., 2017). Fisheye camera models can be classified considering different type of projections (namely equidistant, equisolid, stereographic and orthographic). However, it is important to point out that apart from the distortion due to the fisheye lenses there are residual distortions that characterize each single lens and are responsible for the discrepancies from the theoretical model. Because of the market widespread of low-cost wide-angles cameras and their use on board UAV platform, fisheye camera models have been added to the most used commercial software packages (e.g. Agisoft PhotoScan Pro and Pix4Dmapper Pro). Moreover, Matlab 2017b introduced a camera calibration procedure dedicated to fisheye lenses.

The survey took place on 14th of December, at the end of the vegetation season, after the pruning of the grapevines. This period of the year was chosen in order to investigate the ground, without any impediment due to the presence of leaves or branches, meaning that for this study the DSM and the DTM can be considered equivalent. In addition, the survey was used as a test for evaluating the performance of the UAV acquisition with Bebop 2 fisheye camera in agriculture, with the aim of carrying out the same procedure during other vegetation seasons for monitoring the growth of the vineyard. An example of image acquired with such a camera is reported in Figure 4.2.

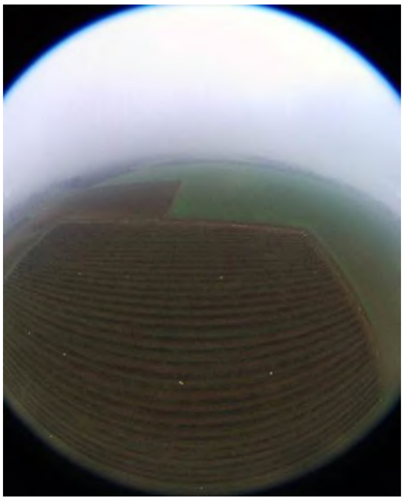

Figure 4.2: *One of the image acquired during the survey.*

A double grid flight was planned with a high longitudinal and transversal overlap, equal to 75% and 70% respectively. The flight height was fixed at 30 m above the ground, ensuring an average Ground Sample Distance (GSD) of about 6 cm.

At the end of the survey a total of 215 images were acquired.A total of 26 black and white (30 cm x 30 cm) and black and yellow panels (50 cm x 50 cm) were placed on the ground and surveyed with a Topcon HiPer SR GNSS receiver (used in Real-Time Kinematic (RTK) mode) in order to obtain the coordinates of the GCPs and Check Points (CPs), which is fundamental to ensure a high geometric accuracy in the generation of the photogrammetric products. Moreover, the coordinates of 15 additional points were acquired with GNSS, in order to generate an independent DTM, through Kriging interpolation, to be considered as reference surface.

In Figure 4.3, the points used as GCPs in the reference scenario are represented in red, while the CPs in yellow, and the additional GNSS points are shown in blue. Both CPs and GNSS points have been used for the generation of the Kriging's interpolated DTM

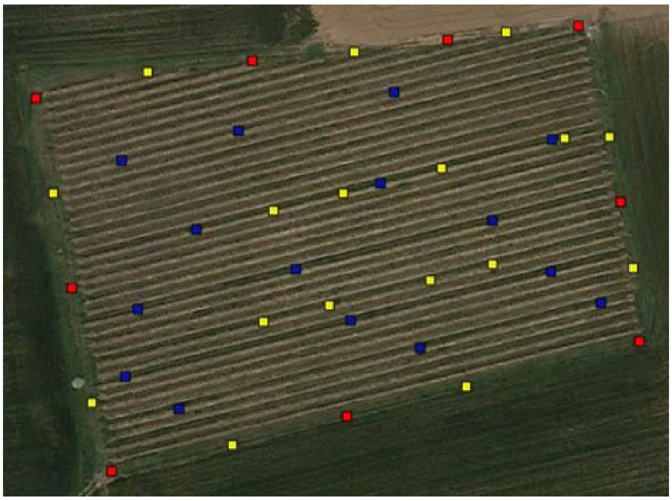

Figure 4.3: *Distribution of points used for the generation of DTM by interpolation and for the photogrammetric process.*

4.1.2 Photogrammetric processing

Two software packages widely used in photogrammetry (Sona et al., 2014), namely Pix4Dmapper Pro and Agisoft Photoscan Pro, have been tested, with the aim to evaluate their performances in case of blocks composed by fisheye images. Moreover, a two-step approach has been realized by pre-processing the images in Matlab 2017b and then performing the bundle block adjustment in Agisoft Photoscan using undistorted rectilinear images. It is worth to notice that these software packages exploit different fisheye mathematical models.

Agisoft PhotoScan fisheye model is based on the general form of the equidistant projection. The residual distortions due to lens imperfections are modelled using an extended version of Brown's model (Duane, 1971) combined with the affinity and shear parameters (El-Hakim, 1986). The resulting equations are:

$$x_d = \frac{f \cdot X}{\sqrt{X^2+Y^2}}\, arctg(\frac{\sqrt{X^2+Y^2}}{Z}) + c_x + \Delta x_{dist} \tag{4.1}$$

$$y_d = \frac{f \cdot Y}{\sqrt{X^2+Y^2}}\, arctg(\frac{\sqrt{X^2+Y^2}}{Z}) + c_y + \Delta y_{dist} \tag{4.2}$$

where f is the focal length, X, Y, Z are the object coordinate of a generic point, c_x, c_y are the coordinates of the principal point and $(\Delta x_{dist}, \Delta y_{dist})$ take into account of radial and tangential distortions as well as affinity and shear parameters.

Also Pix4Dmapper uses an equidistant model but in this case the incidence angle θ is mapped as:

$$\theta = \frac{2}{\pi}\, arctg(\frac{\sqrt{X^2+Y^2}}{Z})\ \ with\ \theta\ \epsilon\ [0,1] \tag{4.3}$$

The relationship between object and image coordinates is modelled as:

$$\begin{pmatrix} x_d \\ y_d \end{pmatrix} = \begin{bmatrix} C & D \\ E & F \end{bmatrix} \begin{pmatrix} \rho \cdot X/\sqrt{X^2+Y^2} \\ \rho \cdot Y/\sqrt{X^2+Y^2} \end{pmatrix} + \begin{pmatrix} c_x \\ c_y \end{pmatrix} \tag{4.4}$$

where $\rho = \theta + p_2\theta^2 + p_3\theta^3 + p_4\theta^4$, p_2, p_3, p_4 are the coefficients of a polynomial function, C,D,E,F are the coefficients that allows to map the undistort image coordinates into the distorted ones (x_d, y_d). The diagonal element of this matrix can be related with the focal length. The fisheye model embedded in Matlab 2017b release is based on the general model for calibrating omnidirectional cameras discussed in Scaramuzza et al. (2006). The mapping function is represented by a Taylor series expansion, whose coefficients are estimated via 4-step least square adjustment. The resultant model for fisheye lenses is described by:

$$x_d = \frac{X}{Z}\left(a_0 + a_2\rho^2 + a_3\rho^3 + a_4\rho^4\right) + c_x \tag{4.5}$$

$$y_d = \frac{Y}{Z}\left(a_0 + a_2\rho^2 + a_3\rho^3 + a_4\rho^4\right) + c_y \tag{4.6}$$

where X,Y, Z are the object coordinates, a_0, a_2, a_3, a_4 are the polynomial coefficients to be estimated during the calibration procedure and ρ is equal to $\sqrt{x^2+y^2}$, with x,y are the ideal projection of the 3D point and c_x, c_y are the coordinates of the principal points.

Different image blocks processing strategies have been tested. First of all, the standard double grid block configuration typical of the Bebop system has been evaluated. In order to assess the configurations with a lower number of images, also separate blocks of images acquired along a single direction have been processed, resulting in one block composed by the stripes parallel to the vineyard rows (96 images), and one block composed by strips orthogonal to the rows direction (119 images). Furthermore, three different GCP / CP configurations were considered. In the first one, a quite standard distribution of the GCPs has been used, placing them both inside and along the perimeter of the investigated area. For the second configuration, the internal points have been excluded from the GCPs in order to evaluate the quality of the photogrammetric solution obtainable in those cases where could be difficult or impossible to access the field. Finally, in the third configuration only 4 GCPs, placed at the corners of the field, have been used. The last configuration simulates the operative case of a quick survey, for a rapid production of DTM and orthomosaics, georeferenced on few GCPs.

Pix4Dmapper Pro

The Bebop system has been developed together with Pix4Dmapper Pro to realize a recommended and standard processing workflow. In fact, this software is able to interpret properly the flight information acquired by the UAV and a good approximation of the embedded camera is stored in its own database. The images have been processed with Pix4Dmapper Pro (version 4.0.25). The tie points search and the estimation of the External Orientation (EO) and Internal Orientation (IO) parameters have been realized using the images at their full resolution, for all the considered scenarios. The dense point clouds have been generated using images with a dimension equal to 1/4 of the original images. Finally, the DTMs have been generated with a ground resolution of 0.40 m.

Agisoft Photoscan Pro

The images have been processed with Agisoft Photoscan Pro (version 1.4.0), following the standard workflow proposed for fisheye cameras, maintaining their full resolution (correspondent to the high alignment quality of the software). A previously estimated set of Internal Orientation (IO) parameters has been used as initial camera calibration. This has been necessary because of the non-coherent pixel size value read by the software from the EXIF file, with respect to the nominal focal length. These approximate parameters have been then refined using PS *optimize stage*. The dense clouds have been generated downgrading the images with a factor equal to 4 (i.e. using the high quality of Agisoft Photoscan Pro), guaranteeing the same level of resolution used by Pix4Dmapper. Also in this case, the DTMs have been generated with a ground resolution of 0.40 m, for all the considered scenarios.

Matlab 2017b + Agisoft Photoscan Pro

A two-step procedure has been tested for evaluating the effect of pre-processing the fisheye images and transforming them into undistorted rectilinear images. A new set of functions that allows to calibrate fisheye images and correct them from lens distortions have been embedded in Matlab 2017b. After a dedicated calibration procedure (realized using the Matlab chessboard pattern), undistorted rectilinear images have been generated, together with the parameters of a virtual perspective camera that produce those images. These images have been processed in Agisoft Photoscan Pro, maintaining the same level of resolution previously illustrated. Because any UAV system suffers impacts during take-off and landing, a self-calibration has been performed in Agisoft Photoscan Pro by using the *optimize stage*. Even if the area covered by the rectilinear images is smaller with respect to the fisheye ones, the image overlapping stays still quite high (>9), which does not affect the completeness of the generated 3D models. The DTMs have been generated with a ground resolution of 0.40 m.

Bundle block adjustment results

The quality of the photogrammetric solution has been evaluated considering the residuals of the CPs, for all the scenarios. The results are shown in Table 4.1. They are all in line with the requested tolerance, indeed the highest 3D residuals are of the order of 0.07 m in the worst case. From here on, Pix4Dmapper Pro is defined as P4, Agisoft Photoscan Pro as PS and the processing with Matlab 2017b and Agisosoft Photoscan Pro is identified as MPS.

Considering the different flight configuration, it is quite evident that the better results have been obtained for the double grid configuration, with 3D residuals of the order of 0.03 m for all the evaluated software packages, and horizontal residuals around 0.015 m. This is quite reasonable because such flight path ensures the strongest acquisition geometry, which reflects in a better intersection of the homologous rays.
Moreover, it is quite evident that the use of internal GCPs has no meaningful impact on the final accuracy. As expected, the use of only four corner GCPs slightly reduces

Table 4.1: *Residuals on the CPs after bundle block adjustment.*

Software packages	Flight configuration	N° GCP	E [m]	N [m]	h [m]
P4	double grid	13	0.016	0.015	0.021
P4	double grid	9	0.014	0.017	0.028
P4	double grid	4	0.027	0.025	0.032
P4	along row	13	0.041	0.028	0.017
P4	along row	9	0.042	0.030	0.028
P4	cross row	13	0.040	0.038	0.019
P4	cross row	9	0.039	0.036	0.025
PS	double grid	13	0.013	0.015	0.019
PS	double grid	9	0.012	0.016	0.019
PS	double grid	4	0.022	0.020	0.024
PS	along row	13	0.031	0.021	0.012
PS	along row	9	0.027	0.023	0.016
PS	cross row	13	0.029	0.034	0.024
PS	cross row	9	0.028	0.030	0.023
MPS	double grid	13	0.016	0.016	0.022
MPS	double grid	9	0.015	0.018	0.024
MPS	double grid	4	0.021	0.019	0.023
MPS	along row	13	0.060	0.037	0.016
MPS	along row	9	0.058	0.036	0.018
MPS	cross row	13	0.017	0.026	0.037
MPS	cross row	9	0.018	0.021	0.025

accuracy in all double grid cases.

For both MPS and P4 the worst results have been obtained for the block composed only by the images acquired along the vineyard rows. Instead, for PS there is slight worsening for the block composed by the images acquired orthogonal to the vineyard rows, especially along N and h coordinates.

4.1.3 Kriging interpolation

The reference DTM has been obtained by interpolating 15 points, whose coordinates have been measured with GNSS-RTK. This low number of observations has been considered sufficient for the estimation of the DTM because the investigated area is quite flat, without significant topography variation. The DTM has been obtained by interpolation using the Kriging method, in the version implemented in the Geostatistical Wizard of ArcMap (version 10.5). The use of a geostatistical method has been preferred to the use of a deterministic methods (such as Inverse Weighted Distance, spline etc.) because it provides also a standard map error, that shows the uncertainty related to the predicted values (Burrough et al., 2015). In the absence of a precise DTM generated through an Aerial Laser Scanner survey, the reference DTM has been created using the ordinary Kriging, which assumes that there is an unknown constant mean value and that the phenomenon is continuous in the space. These assumptions can be considered correct in case of a field characterized by a flat topography, without a pronounced trend. Of course, the model created with an interpolation procedure tends to be flatter with respect to the DTMs generated from photogrammetry, because it does not capture local spatial variability (e.g. minor ground furrows). The resulting interpolated model is shown in Figure 4.4, while the standard error map is reported in Figure 4.5. The hypothesis of almost flat field is respected, as the maximum variation in 150 m (along the diagonal of the field) is less than 1.5 m. Moreover, errors are lower than 0.03 m for most of the area; as expected the highest error values are located along the edges.

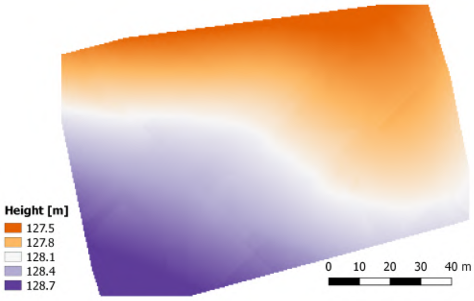

Figure 4.4: *The DTM created by Kriging interpolation.*

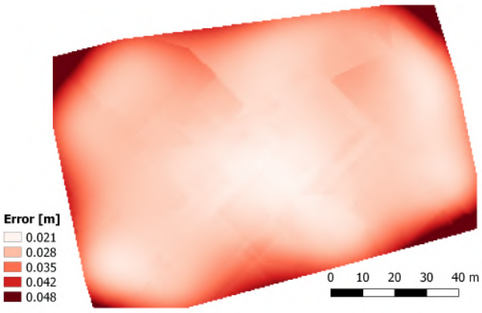

Figure 4.5: *Kriging error prediction map.*

4.2 Results

As a first general remark, it can be stated that all photogrammetric process strategies gave satisfactory results, as even the worst accuracies are around 0.06 m, that for agricultural applications is by far sufficient. All the DTMs, obtained with different image block configurations, number of GCPs and software packages, have been compared with the reference one, generated by Kriging interpolation. This DTM is considered as reference because point interpolation describes the main behavior of height field, neglecting the high frequency details due to lines and interlines of the vineyard. For the sake of brevity, only few comparisons are here analyzed and deeply discussed, choosing the better cases. Crossing the information that double grid blocks have produced the better accuracies, and at the same time the use of GCPs in the middle of the field have not improved results, we can consider as *best result*, for each processing type (MPS, PS or P4) the block formed with double grid and 9 GCPs on the border.

In Figure 4.6, the differences between the reference DTM and the photogrammetric models obtained with different software packages are shown. It is quite evident, that the computed differences underline the presence of the furrows for all the cases. This is

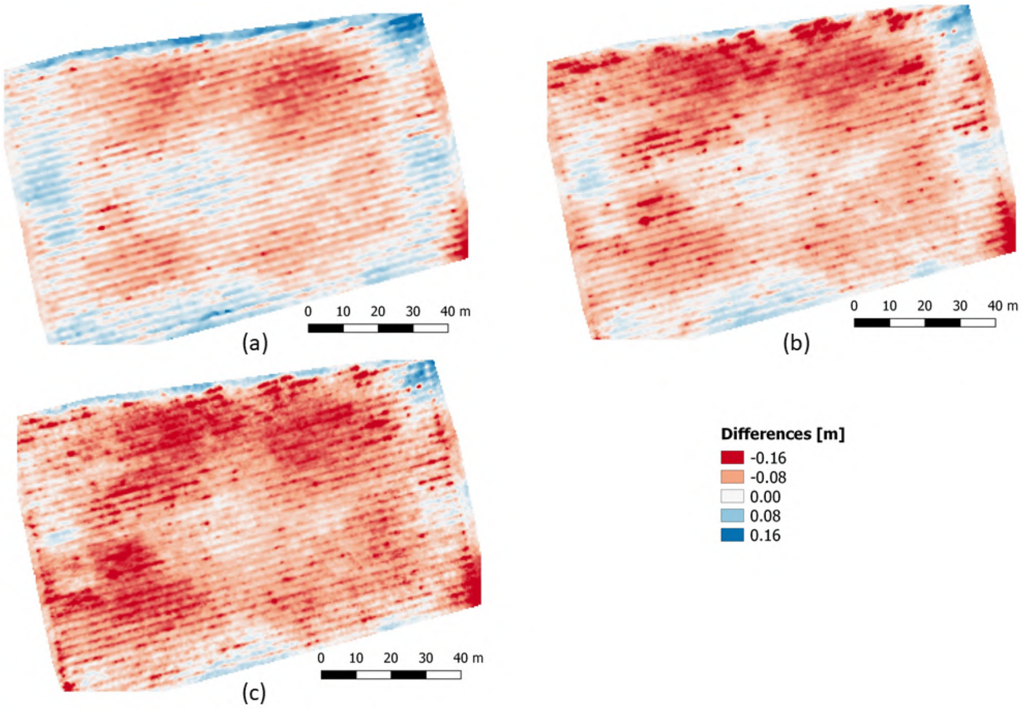

Figure 4.6: *Differences between the computed DTM for the 9 GCPs scenario:* ***a)*** *P4,* ***b)*** *PS,* ***c)*** *MPS.*

because the photogrammetric models represent the terrain with a higher level of detail, while the interpolated model is smoother and correctly represents only low frequency phenomena. Moreover, all the computed maps are characterized by a common spatial pattern, which reflects the spatial distribution that can be observed in the error prediction map, generated during the Kriging interpolation (see Figure 4.4). The highest differences between the reference DTM and the photogrammetric ones are of the order of 0.2 m (absolute values). Table 4.2 reports mean and standard deviation values for the computed differences. The values show a good agreement among the models. Considering that the standard deviations assume the same values for all the cases, P4 model is the most similar to the reference one. This can be due to the better performance of this software, with processing options specifically designed for Parrot Bebop fisheye imagery. Even if, a certain level of smoothing due to interpolation is inevitably introduced by each software packages during DTM generation, it has been noticed that P4 point clouds were in general smoother than point clouds generated with PS and MPS. This is probably due to the fact that tie-points search is performed by using a sky-mask, which avoid creating erroneous matchings that increase the roughness of the computed point cloud.

Table 4.2: *Means and standard deviations of the DTM differences.*

	μ [m]	σ [m]
P4	-0.025	0.048
PS	-0.053	0.048
MPS	-0.069	0.049

The smooth behaviour of DTM produced by Kriging interpolation is evident even in the section, shown in Figure 4.7. The photogrammetric models well describe the terrain profile with the high frequency component given by the presence of furrows and lines. In addition, the profile confirms that the DTM generated by P4 software is the closest to the reference one.

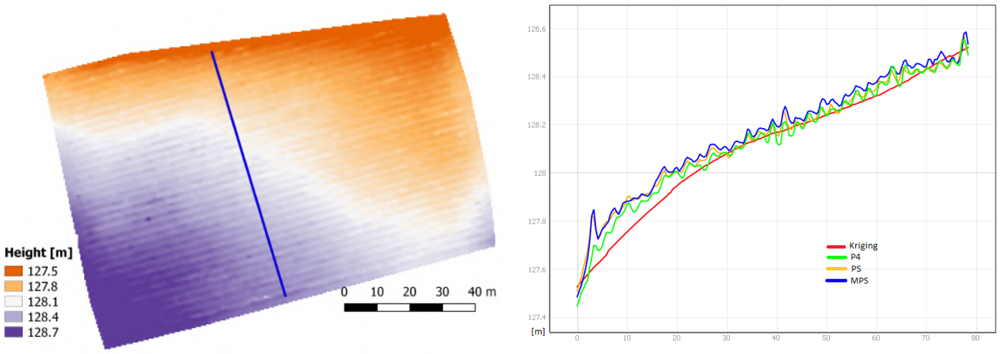

(a) **(b)**

Figure 4.7: *(**a**) DTM generated with P4 software and extracted section (blue line); (**b**) terrain profiles extracted from the different DTMs.*

4.3 Conclusions

This case study investigates the use of Parrot Bebop 2 fisheye camera for generating very high resolution DTM to be employed for precision agriculture purposes, as well as prescription irrigation maps. All the tested strategies have given good results and this study has been useful for defining best practices for surveying and processing optimization.

It is feasible to obtain accurate DTMs without any GCPs placed inside the field, as long as GCPs are in sufficient number for the photogrammetric process and well distributed all around the surveyed area. Image pre-processing, aimed at removing fisheye distortion to produce standard frame images, is not necessary and not advantageous in terms of computational time. Regarding Agisoft Photoscan Pro, recent releases of the software can deal with fisheye cameras, but high quality processing is not worthy in terms of requested time with respect to obtained accuracies. Double grid flight configuration should be preferred to single direction flight. In order to reduce the acquisition and processing time, it should be considered to reduce the number of strips and images. This implies a reduction in transversal and longitudinal overlaps (Ajayi et al., 2017). The GSD high variability through a single image and the real overlapping areas must be carefully taken into account. To check the accuracies obtainable with this strategy, further processing tests should be performed, by forming image blocks selecting one every two images, and one every two strips.

CHAPTER 5

Crop row detection to optimise on-farm irrigation management

In the context of Precision Agriculture (PAg), particular attention is given to the optimization of on-farm irrigation management, since water resources for agricultural use have become scarcer in recent decades due to the combined effect of climate change and increased competition between different water uses (WWAP/ UN-Water, 2018, Pachauri et al., 2014). Additionally, in many areas, the growing crop water requirement and the reduction of rainfall during the cropping season led to the need to irrigate crops traditionally not irrigated (Costa et al., 2016). In fact, due to the increase in extreme weather events, irrigation is becoming an important tool to guarantee adequate quality standards to agricultural products (Castellarin et al., 2011).

The optimization of on-farm irrigation management, particularly variable rate drip irrigation systems, is based on the spatial variability of soil and crop properties. UAV imagery is used in PAg to monitor this variability and produce crop maps. When a row crop is the object of investigation, UAV imagery must be post-processed to identify and extract crop row from soil background and weeds. Different studies can be found in the literature, proposing (semi)automatic methods, using image-processing techniques on a single-band image, Vegetation Indices (VIs), or Digital Elevation Models (DEMs), to detect crop canopy (Pádua et al., 2018a). Poblete-Echeverría et al. (2017) compared the performance of four classification methods, including standard and well-known methods (i.e. K-means and VIs thresholding) and machine learning methods (i.e. Artificial Neural Networks (ANN), and Random Forest (RF)), for vine canopy detection using ultra-high resolution RGB Imagery acquired with a conventional camera mounted on a low-cost UAV. Marques et al. (2019) presented an UAV-based automatic method to detect chestnut trees, by using RGB and CIR orthomosaics combined with the canopy height model. In Li et al. (2019), potato plant objects were extracted from bare soil using Excess Green Index and Otsu thresholding methods.

This case study focuses on the crop row detection and extraction by analysing and post-processing images acquired through UAV. Different methodologies were tested and compared, as well as several segmentation methods, such as supervised classifications, Bayesian segmentation and algorithms developed ad hoc for this purpose. Extraction algorithms were applied both on geometric products (i.e., DEM) and VIs, and the assessment of the methods was performed on different crop types, including grapevine, pear and tomato. As a remark, this study is inserted in a project, namely NUTRIPRECISO, realized in cooperation with the University of Milan, aimed at developing and disseminating the new management practices of PAg.

5.1 Materials

5.1.1 NUTRIPRECISO project

“Precision fertilization and irrigation techniques in fruit-viticulture and horticulture”, namely NUTRIPRECISO (RDP-EU, measure 1.2.01, Lombardy Region), is a two-years project supported by PSR (Programma di Sviluppo Rurale) Lombardia 2014-2020 Operation 1.2.01 “Information and demonstrative projects”, which started in November 2017 as a collaboration among the Department of Agricultural and Environmental Sciences-Production, Landscape, Agroenergy (DiSAA) of the University of Milan, the Department of Civil and Environmental Engineering (DICA) of the Politecnico di Milano, and CREA (Consiglio per la ricerca in agricoltura e l’analisi dell’economia agraria). The aim of the project is to design, realise and manage variable rate drip irrigation systems in vineyards, orchards and horticultural crops. The project is addressed to the various stakeholders involved in the agricultural process, i.e. farmers, agronomists, agricultural machinery drivers. Therefore, demonstrative and educational activities are part of the project, in order to let the agricultural world know the PAg techniques and their implementation methods in fruit-growing, viticulture and horticulture.

5.1.2 Study sites

Three different types of crops have been investigated in the NUTRIPRECISO project: grapevine, pear, and tomato; therefore, three different areas have been chosen as study sites, to be representative for each crop. According to the project specifications, the three sites have been selected in the Lombardy Region. The location of the vineyard is shown in Figure 4.1, while the pear orchard and tomato sites are reported in Figure 5.1. In the following, the main characteristics of the three study sites are described.

Vineyard

The vineyard involved in the project is located in Olfino di Monzambano, province of Mantova, Northern Italy (see Chapter 4). The soil of the site is composed by sand, silt and clay, and the climatic condition are warm and mild with important rainfall (mean annual value: 816 mm *(climate-data.org)*), that provide favourable conditions for the grapevine to grow. The vineyard has an extent of around one hectare and is characterized by the presence of Chardonnay grapes, with rows height and width of about 1.3 m and 0.6 m, respectively, and the distance between rows is about 2.4 m.

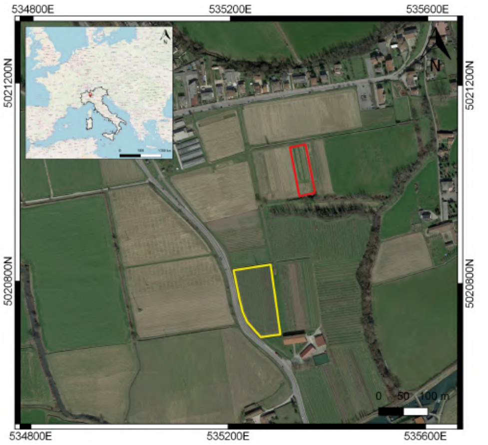

Figure 5.1: *The experimental sites located in Montanaso Lombardo (LO): in yellow the pear orchard, in red the tomato field; Coordinate Reference System (CRS): WGS84/UTM zone 32 N. Map data: ©OpenStreetMap contributors.*

Pear orchard

The pear orchard selected for this study is part of the experimental farm of University of Milan, located in Arcagna locality, Montanaso Lombardo (province of Lodi, LO). The area is characterized by warm and mild climatic condition (mean temperature: 13°C), with important rainfalls throughout the year (mean annual value: 897 mm *(climate-data.org)*); the soil is loam, more clayey in deep horizons. The orchard has an extension of about one hectare, and four different pear varieties are cultivated, namely Williams, Abate, Kaiser and Conference variety, distributed in 17 rows with inter-rows distance of about 2 m.

Tomato field

The third site included in the project is an area of about one hectare cultivated with industrial tomato “Pietra Rossa F1”, inside the CREA ORL, at Montanaso Lombardo (LO). The soil of the site is loam (sand, silt and clay), while climatic conditions are the same of the ones above-described for the pear orchard site. Tomatoes plants are few centimeters height and are cultivated in parallel rows of 0.5 m width, and distance between rows of about 1.5 m.

5.1.3 UAV surveys and photogrammetric processing

Two UAV surveys were conducted on each study site, during the agricultural season of 2018. For each site, in the first survey, the Parrot Bebop 2 was used to acquire RGB images, as well as the Sequoia camera mounted on the Parrot Disco to collect multispectral imagery during the second survey. The photogrammetric processings of all the surveys were performed with Pix4Dmapper Pro software (version 4.1.1). The details of the surveys and their processing are described in the following sections.

Vineyard

The RGB survey of the vineyard took place on 28th June 2018, while the multispectral one, six days later on the 4th July. The flight height of the Parrot Bebop 2 used in the RGB survey was set to 40 m (AGL), while the Parrot Disco flew at 60 m (AGL) during the multispectral survey. The same overlaps among images were fixed for the two surveys: longitudinal overlapping equal to 80% and transversal equal to 70%. An amount of 130 and 560 images were collected during the RGB and multispectral survey, respectively. According to sensors characteristics (i.e., Parrot Bebop 2 fisheye camera and Sequoia camera), the final GSD of the acquired images was about 0.1 m for both cases. As suggested in Ronchetti et al. (2018), the coordinates of 9 GCPs were measured with the GNSS receiver Leica Viva GS14 (Leica Geosystems, Heerbrugg, Switzerland) in Network Real Time Kinematic (NRTK) mode, to ensure the georeferencing of the photogrammetric products with high accuracy. According to the results of the study described in Chapter 4, eight GCPs were distributed all around the perimeter of the vineyard, while the nineth target was placed in the middle of the field (Figure 5.2).

At the end of two independent photogrammetric processings, performed with Pix4Dmapper Pro software, a Digital Surface Model (DSM), a RGB orthophoto and a four bands multispectral orthophoto were produced, with GSD of around 0.1 m, to exploit for the crop row detection. The DSM generated after the multispectral survey had lower quality than the RGB one, therefore avoided from further analysis. Table 5.1 summarises the residuals on GCPs after photogrammetric processing, while in Figure 5.3 DSM and orthophotos of the vineyard are shown.

Figure 5.2: *Ground Control Points (GCPs) distribution for the surveys on the vineyard. Map data: ©Google Satellite.*

Pear orchard

In the pear orchard site, the RGB and multispectral surveys were conducted on 26th June and 2nd July, respectively. The characteristics of the flights were the same of the surveys performed on the vineyard site: longitudinal overlap among images equal to 80%, transversal overlap equal to 70%, flight height set at 40 m and 60 m for the multirotor UAV and the fixed-wings UAV, respectively, thus ensuring a GSD of the

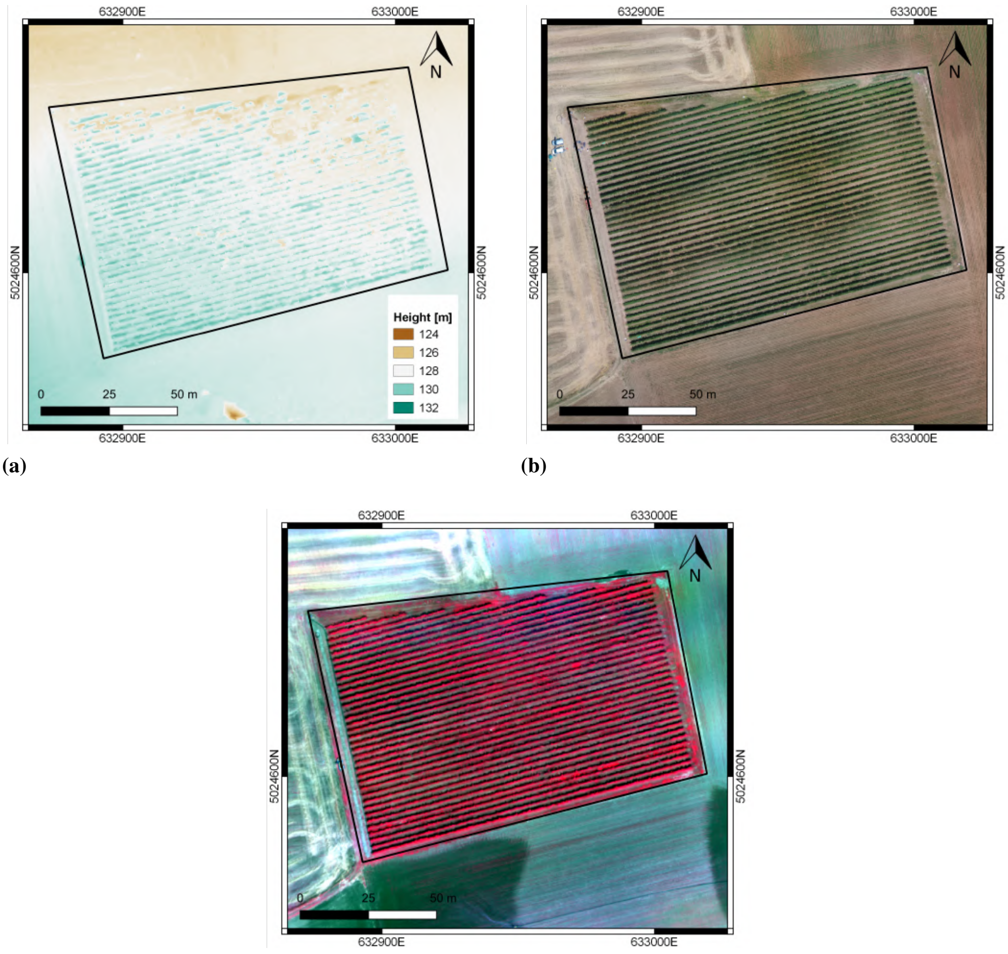

(a) (b) (c)

Figure 5.3: *Vineyard site: DSM (**a**) and orthophoto (**b**) produced through photogrammetric processing of RGB dataset; false color orthophoto (**c**), generated from the multispectral dataset.*

Table 5.1: *Vineyard site: residuals on the GCPs after bundle block adjustment.*

Label	Easting [m]	Northing [m]	height [m]
v1	-0.029	-0.008	0.088
v2	-0.007	-0.012	-0.012
v3	-0.025	-0.030	-0.063
v4	0.008	0.025	0.062
v5	0.015	0.005	0.000
v6	0.022	-0.013	0.024
v7	0.030	-0.013	0.027
v8	0.020	-0.015	-0.086
v9	0.012	0.008	0.012
RMSE	**0.021**	**0.016**	**0.052**

images of about 0.1 m. 147 images were acquired during the RGB survey, while 540 during the multispectral one. During the UAV flights, seven targets were placed on the terrain to be used as GCPs, well distributed all around the orchard, as shown in Figure 5.4. As the case of the vineyard, the DSM and the orthophotos were produced in Pix4Dmapper Pro with a spatial resolution of 0.1 m (Figure 5.5). The residuals on the GCPs computed after the photogrammetric workflow are reported in Table 5.2.

Figure 5.4: *Ground Control Points (GCPs) distribution for the surveys on the pear orchard. Map data: ©Google Satellite.*

Table 5.2: *Pear orchard site: residuals on the GCPs after bundle block adjustment.*

Label	Easting [m]	Northing [m]	height [m]
p1	-0.050	-0.017	0.007
p2	-0.032	-0.004	-0.017
p3	0.018	-0.060	0.021
p4	0.028	-0.089	0.113
p5	0.003	0.023	-0.290
p6	0.100	0.053	0.018
p7	-0.085	0.003	0.054
RMSE	**0.056**	**0.047**	**0.119**

Tomato field

Given the proximity of the two sites, the tomato field was surveyed on the same days as the pear orchard, with the same equipment and flight characteristics. During the RGB survey, 96 images were acquired, as well as 388 images came from the multispectral flight. From these datasets, one DSM and two orthophotos, having a GSD equal to 0.1 m, were generated after bundle block adjustment in Pix4Dmapper Pro. The various photogrammetric products were georeferenced by means of six GCPs, whose centre coordinates were measured with GNSS-RTK on the dates of the surveys. The distribution of the GCPs on the tomato site and their computed residuals are shown in Figure 5.6 and Table 5.3, respectively. The photogrammetric products are reported in Figure 5.7.

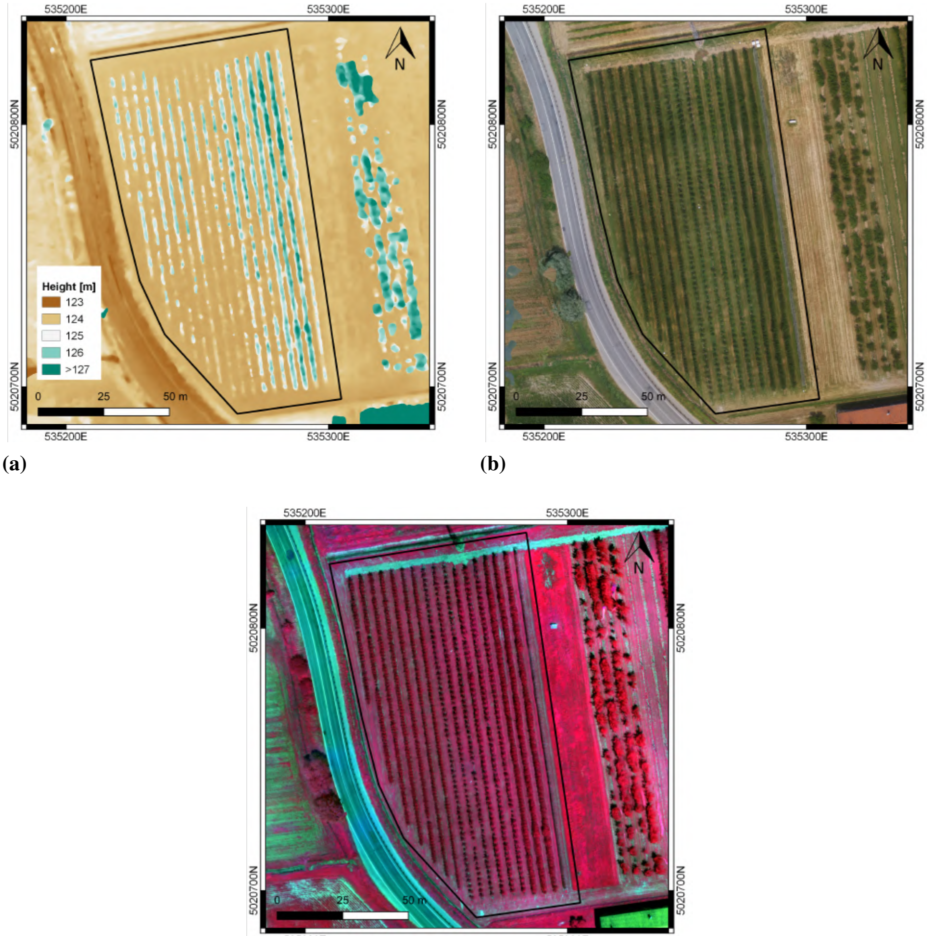

(a) (b)

(c)

Figure 5.5: *Pear orchard site: DSM (**a**) and orthophoto (**b**) produced through photogrammetric processing of RGB dataset; false color orthophoto (**c**), generated from the multispectral dataset.*

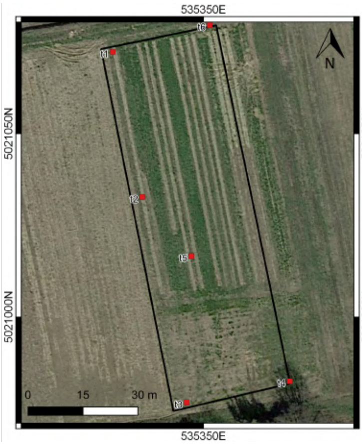

Figure 5.6: *Ground Control Points (GCPs) distribution for the surveys on the tomato site. Map data: ©Google Satellite.*

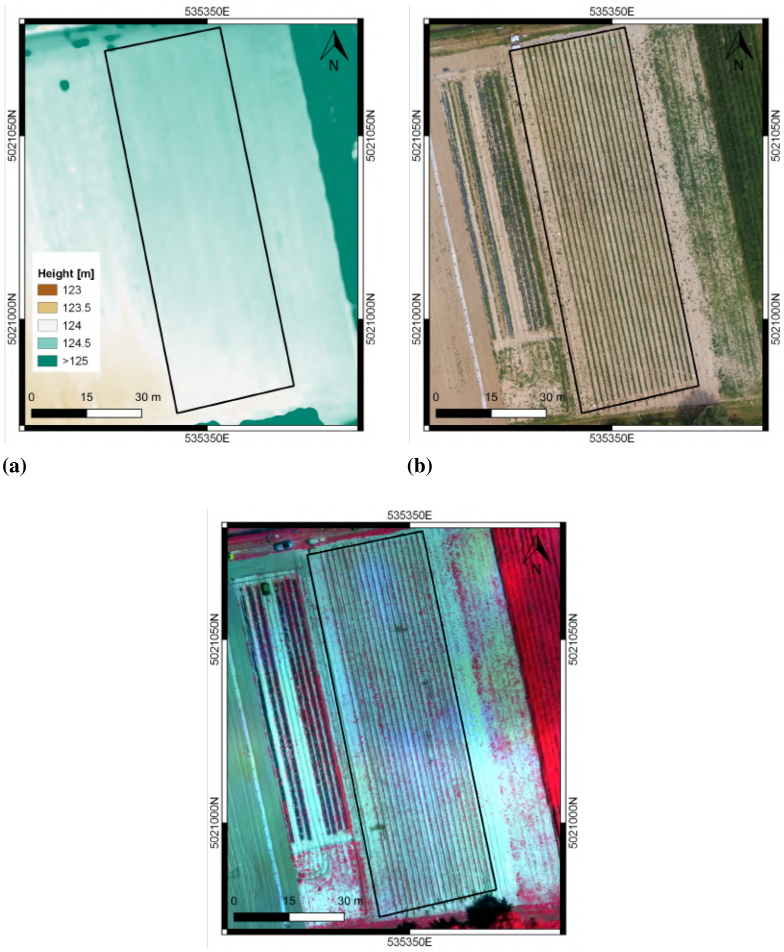

(a) (b) (c)

Figure 5.7: *Tomato site: DSM (**a**) and orthophoto (**b**) produced through photogrammetric processing of RGB dataset; false color orthophoto (**c**), generated from the multispectral dataset.*

Table 5.3: *Tomato site: residuals on the GCPs after bundle block adjustment.*

Label	Easting [m]	Northing [m]	height [m]
t1	-0.098	0.071	-0.101
t2	0.095	0.068	0.046
t3	0.028	0.71	0.077
t4	-0.026	-0.127	-0.054
t5	-0.019	-0.154	0.149
t6	-0.053	-0.038	0.114
RMSE	**0.062**	**0.096**	**0.097**

5.2 Crop row detection methods

To differentiate between crop canopy and background is particularly challenging. Nevertheless, the variety of crop types considered in this study leads to exploit many different methods with diverse inputs for extracting crop rows. In the following Sections, five different detection methods are proposed; some of them were taken from existing literature, while two methods, labelled as *Thresholding algorithms*, were developed ad hoc for the purposes of the project.

In order to achieve the best possible crop mask to be used to identify crop rows on orthophotos, Vegetation Indices (VIs) were chosen as inputs of the detection methods, as already proposed by many authors (Poblete-Echeverría et al., 2017, Pádua et al., 2018b, Marques et al., 2019). Considering vegetation, most of those indices take into account Red (R) and Nir reflectance bands (ρ_λ): the greater is the difference between ρ_R and ρ_{Nir}, the greater is the amount of green and healthy vegetation in that particular pixel. Among all the possible VIs, only those composed of spectral bands that sensors involved in the surveys could provide, were used in this study (Table 5.4).

To fully exploit the proposed methods, also the DSM and RGB orthophoto were individually used as inputs. This ensures that the methods are still operational, even in the cases where only imagery resulting from UAVs which only supports RGB sensors is available, as for the Parrot Bebop 2.

Table 5.4: *Vegetation Indices (VIs) used in this study.*

Index	Name	Formula	References
NDVI	Normalized Difference Vegetation Index	$\frac{Nir-Red}{Nir+Red}$	Rouse Jr et al. (1974)
SR	Simple Ratio	$\frac{Nir}{Red}$	Birth and McVey (1968)
SAVI	Soil-Adjusted Vegetation Index	$\frac{Nir-Red}{Nir+Red+L}\,(1+L)$	Huete (1988)
ARVI	Atmospherically Resistant Vegetation Index	$\frac{Nir-RB}{Nir+RB}$ where: $RB = Red - \gamma(Blue - Red)$	Kaufman and Tanre (1992)
ExG	Excess Green	$2(Green) - (Red + Blue)$	Woebbecke et al. (1995)
G%	Normalized Green Channel Brightness	$\frac{Green}{Red+Green+Blue}$	Richardson et al. (2007)

5.2.1 Thresholding algorithms

These algorithms were developed by starting from Weiss and Baret (2017), who proposed a method for crop rows extraction by using as input the 3D Points Cloud. Both methods were generated in Matlab 2017b, and are simply based on the concept that high pixel values correspond to crop row.

Local Maxima Extraction

This method aims to generate a binary raster, where non-null values refer to the presence of the crop canopy. First, the input raster is divided into square cells (macro-cells), then inside each macro-cell a percentage of pixels with the highest values is selected. It is a semi-automatic algorithm, where the user has to define the dimensions of the cell and the percentage value.

This method is sensitive to the user's choices: in particular, the macro-cell dimension should be selected in order to include both crop and ground pixels, thus being close to the distance between rows or slightly larger. Macro-cell size should be neither too small nor too big with respect to the distance between rows. If it is too small, a wrong selection of pixels is performed whatever the chosen percentage is. When the cell includes only crop pixels, whatever percentage not equal to 100% causes an under-estimation of crop pixels; on the other side, when the cell overlaps only ground pixels, they would be selected as crop pixels, thus producing an over-estimation in the crop mask. The over-estimation arises also when the dimension of the macro-cell is too big, because the probability of selecting pixels belonging to the ground increases with the chosen cell size.

Threshold Selection

This method produces a binary crop mask, by selecting as crop pixels all pixels with values higher than a mean value. The challenging part of this algorithm is the definition of this mean reference value. When both DSM and DTM of the area are available, the CHM could be derived and zero could be considered as the reference value, while in other cases (i.e. VIs as input, no availability of an accurate DTM) it should be determined as described here below.
Starting from the input raster, create a smoothed raster with a moving window average filter. Subtract the smoothed raster to the input raster and define on the differences a threshold to be considered as the reference mean value. Pixels with values greater than the threshold are retained as crop. Even in this algorithm, the user intervention is twofold, choosing the dimensions of the moving window and the value of the threshold, and could cause problems of under/over-estimation of crop canopy pixels.

5.2.2 Classification algorithms

Two well-known classification algorithms were exploited in this study, K-means clustering and Minimum Distance to Mean (MDM) classifier, to be representative of both unsupervised and supervised classification algorithms. Both methods were applied in QGIS (version 3.4), to allow users not familiar with programming languages to run the algorithms thanks to a dedicated user-friendly GUI (Graphical User Interface).

K-means Clustering

It is a well-known algorithm for hard unsupervised thematic classification (MacQueen et al., 1967). The clustering made by K-means is based on the minimization of the objective function $f(\Omega)$, defined as the Euclidean distance of samples of a cluster from respective centroid.

The number of classes (K) is known a priori. Once K is defined, the method consists of three iterative steps. In the first step, for each class k_i, a centroid is automatically chosen. The rest of the data are assigned to k clusters based on the minimum distance criterion. The Euclidean distances of each sample from the centroids are computed and, in the second step, the sample is assigned to the cluster for which the computed distance is minimum. In the last step, centroids are re-calculated and all the samples are re-assigned. This step is iterated until the clustering converges to a stable solution, namely when centroids of clusters do not change meaningfully.

The final configuration is stable and does not depend on the initial position of centroids arbitrarily selected. The initial configuration only influences the number of iterations necessary to reach the convergence.

Minimum Distance to Mean Classifier

This method finds the mean values of all the training sets and classifies all the image pixels according to the class mean they are closest. The process is performed for all image pixels, one at a time. Bounds are determined using statistics derived from the training sets and the used distance is the Euclidean one.

As all supervised algorithms, a crucial phase of MDM classifier is the selection of the training samples. They are used to compute class spectral signatures, therefore must be representative of all the classes. In this study, training samples were defined by visual inspections of the UAV images and grouped in two macro-classes: *crop canopy* and *background*, which includes weeds, soil and shadow pixels.

5.2.3 Bayesian segmentation

This method relies on the Bayesian approach, where any uncertainty can be considered *random variables*, that are fully described by probability distributions (Ross, 2003). Given the vector of data *y* and the vector of parameter *x*, the conditional distribution of parameters is described by the Bayes theorem (Bayes, 1763):

$$P(x|y) = \frac{P(x,y)}{P(y)} = \frac{P(y|x)P(x)}{P(y)} \tag{5.1}$$

where:
$P(x|y)$ is called *posterior probability* and describes the new level of knowledge of the unknown parameters *x* given the observed data *y*.
$P(y)$ is a *normalization constant* used to impose that the sum of $P(y|x)$ for all possible x is equal to 1.
$P(x)$, instead, represents the *prior probability* distribution. It describes the knowledge of the unknown parameters *x* without the contribution of the observed data.
$P(y|x)$ is defined as *likelihood* and is a function of *x*. It describes the way in which the a-priori knowledge is modified by data and depends on the noise distribution.

The terms in equation 5.1 can be adapted to match the purpose of this study, the detection of crop rows: the posterior probability is the probability of a pixel to be part of the class *crop canopy* or *background*, the prior probability is defined starting from mean and standard deviation values, a-priori assigned to each class, and the likelihood is described by a Gaussian distribution, in which the parameters are mean and standard deviation of the two classes:

$$P(y_i|x_i) = \frac{1}{\sigma_{x_i}\sqrt{2\pi}} exp\left(-\frac{(y_i - \mu_{x_i})^2}{2\sigma_{x_i}^2}\right) \tag{5.2}$$

The final goal of Bayesian approach can be identified in finding the optimal parameters *x* that maximize the posterior probability distribution $P(x|y)$. This is called

Maximum a Posteriori (MAP) estimate (Geman and Geman, 1984) and it is defined as:

$$x^{MAP} = \arg\max_{x} P(x|y) \tag{5.3}$$

In crop row detection, it consists in assigning a unique class to each pixel of the image, depending on the posterior probabilities estimated for each pixel. In order to obtain outputs less affected by pixel noise, smoothing filters or image adjustment can be applied on input raster.

5.3 Results

Considering all the detection methods, their parameters and all the possible input rasters, the number of crop mask potentially available is very high. For the vineyard site, 191 outputs were tested, 166 and 104 for the pear orchard and tomato site, respectively. For the sake of brevity, only the best masks, representing each detection method, are here reported and compared. An exhaustive analysis of all the tests performed is described in Marino and Marotta (2019).

The assessment of the results was performed by computing error matrices and classification accuracies (Overall Accuracy (OA), User's Accuracy (UA), and Producer's Accuracy (PA)), on some validation samples manually identified on orthophotos. In particular, the quality of the crop detection was defined according to the value of PA of the class *crop canopy*: the greater is the PA, the lower is the probability to omit crop pixels, therefore to under-estimate the detected crop rows.

5.3.1 Vineyard

For the vineyard site, the parameters of each detection method which arose the best results are reported in Table 5.5.

Table 5.5: *Vineyard site: parameters for the best results of each detection method.*

Method	Input	User's choices
Local Maxima Extraction	G%	cell size: 5 m percentage: 30%
Threshold Selection	DSM	cell size: 3 m threshold: 0.3
K-means Clustering	RGB orthophoto	classes: 6
MDM Classifier	RGB orthophoto	classes: 2
Bayesian Segmentation	2G_RBi, Gaussian filter (σ = 3)	Background: μ=0.2, σ=0.2 Crop canopy: μ=0.7, σ=0.25

For the computation of the error matrices, 104 polygons (N pixels = 42732) were defined for the class *crop canopy* and 97 polygons (N pixels = 64309) for the class *background.* In Table 5.6 the accuracies of the five selected best results are summarised, as well as a detail of each crop mask is shown in Figure 5.8.

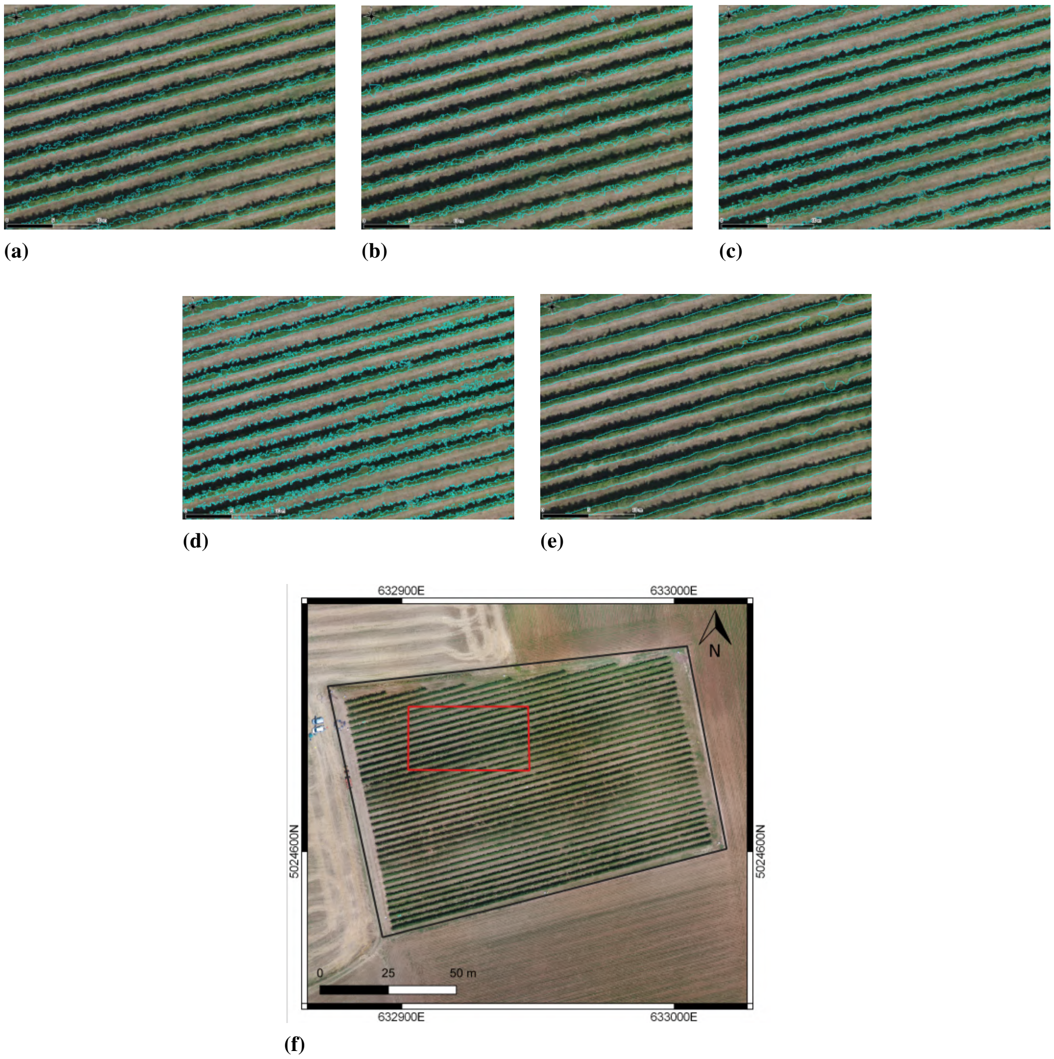

Figure 5.8: *Vineyard site: crop row detection results for (**a**) Local Maxima Extraction, (**b**) Threshold Selection, K-means Clustering (**c**), MDM Classifier (**d**) and Bayesian Segmentation (**e**). Figures refer to the area included in the red box in (**f**).*

Table 5.6: *Vineyard site: assessment of the best results of each detection method.*

Method	**OA**	**PA Crop canopy**	**UA Crop canopy**
Local Maxima Extraction	0.94	0.95	0.91
Threshold Selection	0.76	0.41	0.99
K-means Clustering	0.82	0.73	0.80
MDM Classifier	0.87	0.84	0.83
Bayesian Segmentation	0.96	0.97	0.94

5.3.2 Pear orchard

The parameters for the best results of each detection method for the pear orchard, are summarised in Table 5.7.

Table 5.7: *Pear orchard site: parameters for the best results of each detection method.*

Method	Input	User's choices
Local Maxima Extraction	DSM	cell size: 4 m percentage: 40%
Threshold Selection	DSM	cell size: 4 m threshold: 0
K-means Clustering	RGB orthophoto	classes: 5
MDM Classifier	RGB orthophoto	classes: 2
Bayesian Segmentation	NDVI, Gaussian filter (σ = 3)	Background: μ=0.8, σ=0.04 Crop canopy: μ=0.93, σ=0.04

The error matrices were computed starting from a validation set composed by 37 polygons (N pixels = 44889) for the class *crop canopy* and 34 polygons (N pixels = 62378) for the class *background*. The five selected best results and their respective accuracies are presented in Figure 5.9 and in Table 5.8.

Table 5.8: *Pear orchard site: assessment of the best results of each detection method.*

Method	OA	PA Crop canopy	UA Crop canopy
Local Maxima Extraction	0.92	0.88	0.93
Threshold Selection	0.95	0.97	0.92
K-means Clustering	0.95	0.90	0.99
MDM Classifier	0.87	0.68	0.99
Bayesian Segmentation	0.94	0.91	0.95

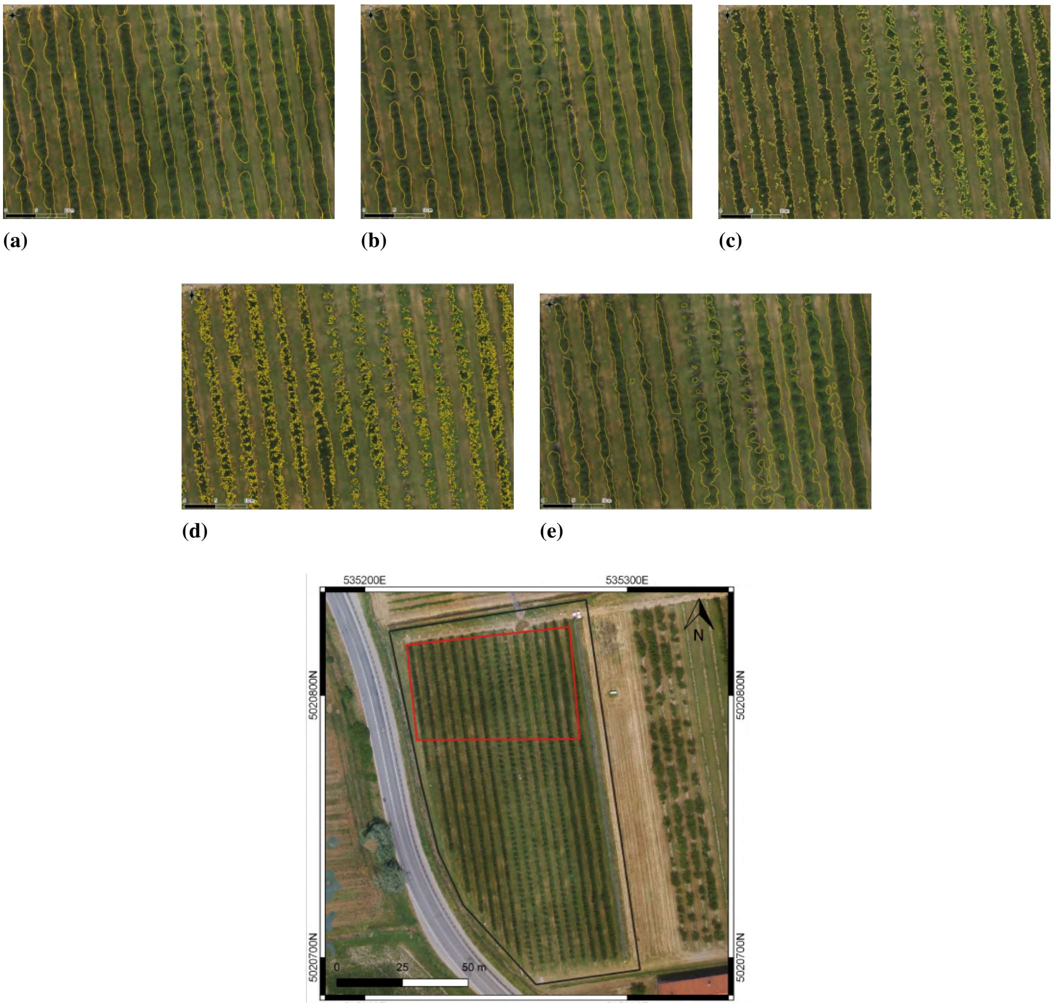

(a) (b) (c) (d) (e) (f)

Figure 5.9: *Pear orchard site: crop row detection results for (**a**) Local Maxima Extraction, (**b**) Threshold Selection, K-means Clustering (**c**), MDM Classifier (**d**) and Bayesian Segmentation (**e**). Figures refer to the area included in the red box in (**f**).*

5.3.3 Tomato field

Table 5.9 reported the parameters chosen for each detection method, which gave the best crop mask outputs.

Table 5.9: *Tomato field site: parameters for the best results of each detection method.*

Method	Input	User's choices
Local Maxima Extraction	G%	cell size: 3 m percentage: 30%
Threshold Selection	DSM	cell size: 4 m threshold: 0
K-means Clustering	SAVI + NDVI	classes: 5
MDM Classifier	SAVI + NDVI	classes: 2
Bayesian Segmentation	2G_RBi, Histogram adjustment	Background: μ=0.05, σ=0.15 Crop canopy: μ=0.65, σ=0.35

The assessment of the results for the tomato site was performed on 52 polygons (N pixels = 81290) for the class *crop canopy* and 42 polygons (N pixels = 155296) for the class *background*. The accuracy values are presented in Table 5.10, while Figure 5.10 shows the crop detection for the five selected methods.

Table 5.10: *Tomato field site: assessment of the best results of each detection method.*

Method	OA	PA Crop canopy	UA Crop canopy
Local Maxima Extraction	0.98	0.94	0.98
Threshold Selection	0.97	0.87	0.99
K-means Clustering	0.93	0.93	0.79
MDM Classifier	0.90	0.60	0.92
Bayesian Segmentation	0.98	0.91	0.98

5.4 Discussion

As general findings, it can be stated that all the methods tested in this study perform well for crop row detection, with OA close or even greater than 0.9. The vineyard site seems to be the most challenging (OA values lower than 0.9 for some methods), due to concurrent presence of weed, bare soil and shadow in the inter-row distance, while

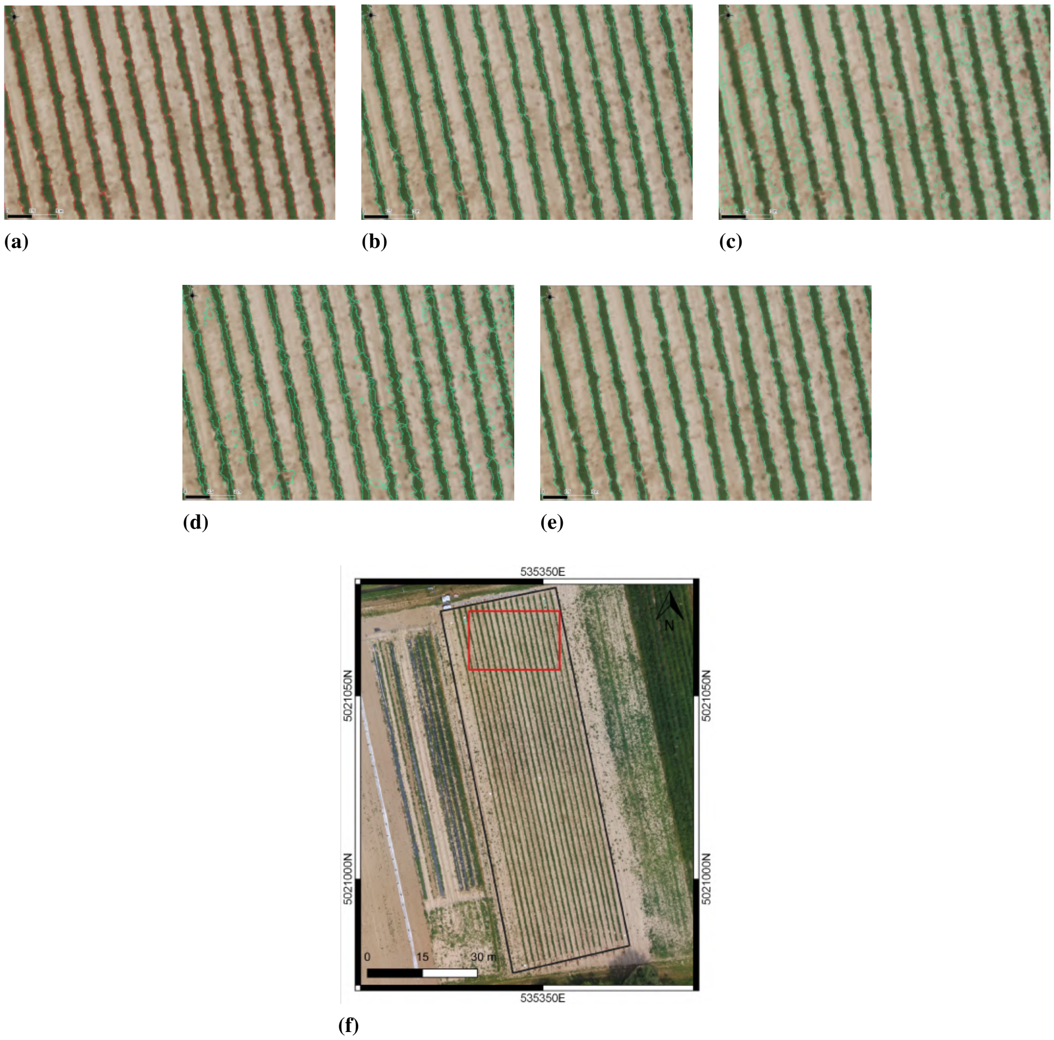

Figure 5.10: *Tomato field site: crop row detection results for (**a**) Local Maxima Extraction, (**b**) Threshold Selection, K-means Clustering (**c**), MDM Classifier (**d**) and Bayesian Segmentation (**e**). Figures refer to the area included in the red box in (**f**).*

the high contrast between bare soil and crop canopy facilitates the crop detection in the tomato site (OA values always higher than 0.9).

Local Maxima Extraction (LME) and Bayesian Segmentation (BS) overall return the best outputs in terms of accuracies values, but with different performances in terms of time-cost and parameters setting. The first method is faster and choosing a cell size comparable with the rows distance, or slightly larger, and a percentage of maxima between 30% and 40% can produce high quality results in all cases. The latter requires a high level of a-priori knowledge and parameters have to be ad-hoc fine-tuned with a time-consuming trial and error approach. Threshold Selection (TS) algorithm needs to be run with an accurate DSM and has bad performances on fields characterised by a relevant slope, as demonstrated by the low accuracy values registered in the vineyard site (OA = 0.76). In hilly fields and non flat areas, to use of a real CHM is necessary and cannot be bypassed by the creation of a smoothed raster. Classification algorithms are easy to run, especially in the QGIS implementation, and widely used in Remote Sensing, but cannot reach, in all cases, the same level of accuracy as the other methods. In addition, these algorithms require considerable human intervention, either in the labelling phase, as the case of the K-means Clustering, or in the delineation of the training samples, as for starting the MDM Classifier.

Regarding input rasters, DSM, RGB orthophotos and VIs obtained as combination of RGB bands are the most adopted in the selected methods. Only the cases of BS on the pear orchard site and classification algorithms for tomato site require NDVI and NDVI joint with SAVI to obtain the best results. Therefore, NIR information does not give any particular additional value in crop row detection and RGB sensors can perform accurate canopy extraction, as already demonstrated by other authors (Poblete-Echeverría et al., 2017, Weiss and Baret, 2017), saving time and cost of the UAV surveys and processing.

According to crop characteristics, specific considerations can be stressed out for each single crop.

In the case of vineyard, it is important to maintain the continuity of the crop row, when detecting the crop canopy. This characteristics is enhanced in the BS, as shown in Figure 5.8e, also thanks to the Gaussian filter applied to the input raster before launching the algorithm. The continuity of the vine rows is also guaranteed by using the LME algorithm as detection method (Figure 5.8a), apart from some rare and sparse pixels. Nevertheless, the two aforementioned methods registered the highest accuracies values, in particular PA values: 0.97 and 0.95 for BS and LME, respectively, considerably greater than the PA values of the other detection methods. The major issue of detecting vine rows is the presence of shadows, weeds and bare soil in the inter-rows distance. Our results demonstrate that the shadow problem makes the classification methods practically unusable on vineyard. In Figure 5.8c and 5.8d, it is clearly visible how the pixels at the edges of the shadow areas are detected as crop pixels. Classification algorithms are unable to separate the vine canopy from its shadow on the terrain, resulting in an overestimation of the crop rows (UA values around 0.8).

In the orchard, pear trees are planted quite distant one from the other (in our study site around 1.5 m), therefore a good detection has to identify single plants rather than rows. In these terms, Classification algorithms return the best results, as visible in Figure 5.9c and 5.9d and confirmed by the highest values of UA practically equal to 1 (Table 5.8). On the other hand, these detection methods also return the most noisy outputs and underestimate the presence of pear trees in the orchard, in particular the MDM classifier with a PA equal to 0.68. The height of the trees favors their extraction from the background, also in presence of weeds in the inter-row distance. To fully exploit this characteristics, it is advisable to use the DSM as input of the whatever detection method, particularly the Threshold Selection algorithm gives the best outcomes in the pear orchard site, with PA value for the class *crop canopy* of 0.97. Unlike the vineyard site, no issues due to the presence of shadows on the terrain were evident in the pear orchard site.

As already mentioned, the tomato field site has the highest accuracy values for the crop detection, thanks to the regular alternation of bare soil and vegetation canopy. The OA values for all the tested methods are higher than 0.9, LME algorithm, BS and K-means also return PA values above 0.9, while the PA of the TS method is slightly lower than 0.9 due to the use of the DSM as input for starting the algorithm. The plants have an height of few centimeters, comparable to image GSD, therefore the errors in the photogrammetric processing (column *height* in Table 5.3) in this specific case affected the results of the canopy detection.

Precision viticulture is already widespread in the world and recent articles have demonstrated the added value that remote sensing from UAV platforms can give to this sector (BorgognoMondino and Gajetti, 2017). Hence, numerous studies can be found in the literature dealing with vine canopy extraction (Weiss and Baret, 2017, Poblete-Echeverría et al., 2017, Cinat et al., 2019, De Castro et al., 2018a). The results presented in this work have accuracy values similar to those available in the literature. From the best of author's knowledge, very few studies have already been published related to the detection of pear trees in orchards or tomato canopy, thus hampering the availability of reference values to compare the outputs. The assessment of the reliability of the illustrated results was based on similar case studies present in the literature. The detection of pear plants was performed with accuracy values slightly lower than the results obtained by Dong et al. (2020), in two orchards in China, but close to the outcomes of the chestnut trees extraction described in Marques et al. (2019). The high values found for the tomato site are in agreement with the results presented in Li et al. (2019), about the estimation of crop emergence in potatoes.

The potential utility of this study in Precision Agriculture is high. The methods here described allow to derive from UAV imagery vegetation properties specifically related to canopy characteristics. In Figure 5.11, 5.12 and 5.13, NDVI maps for the three analysed study sites are shown: on the left, the original maps, while on the right the canopy maps generated after the extraction of crop rows. This information could be used in Precision Agriculture applications for mapping vegetation stress status, or to optimise on-farm irrigation management. As an example, in the following Chapter (6) the use of crop row detection method to delineate Site-Specific Management Zones (SSMZs) maps on a vineyard will be described.

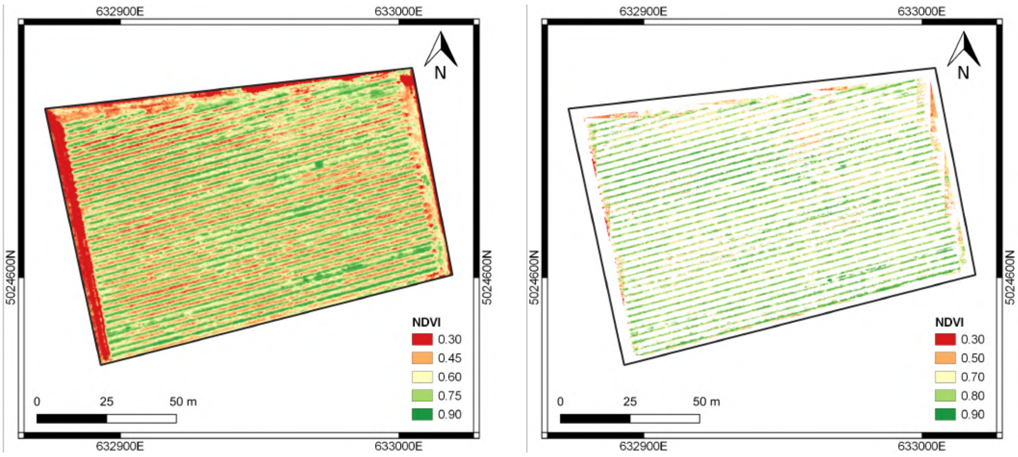

(a) (b)

Figure 5.11: *Vineyard site: NDVI map before (**a**) and after (**b**) the crop rows extraction.*

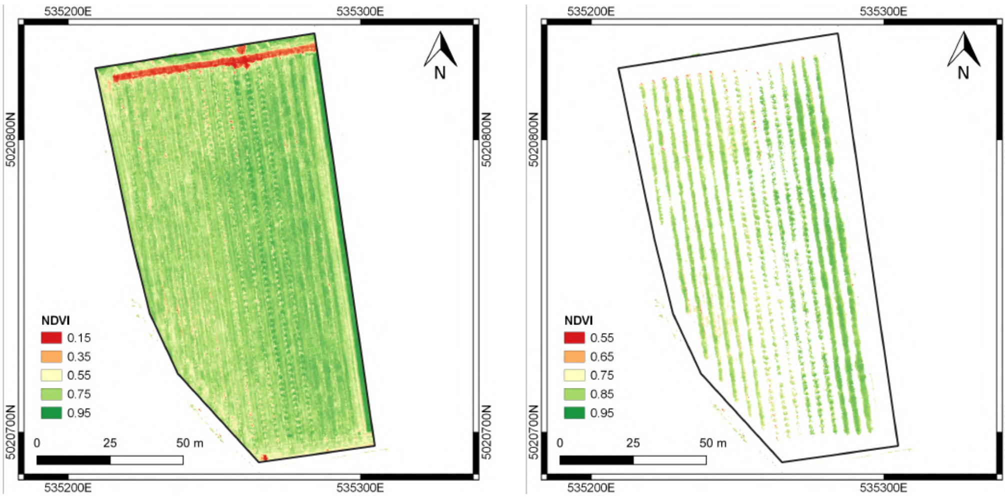

(a) (b)

Figure 5.12: *Pear orchard site: NDVI map before (**a**) and after (**b**) the crop rows extraction.*

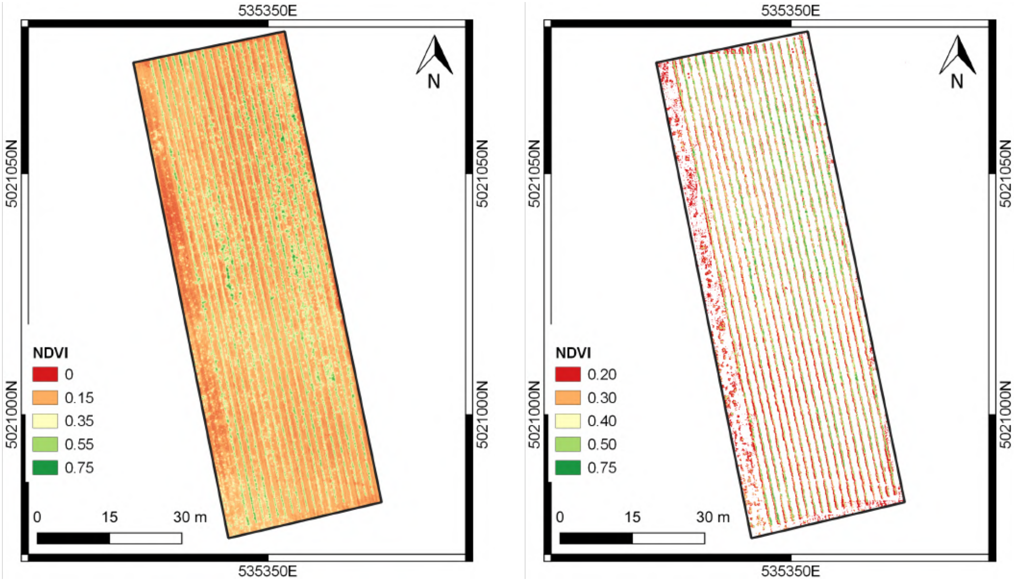

(a) (b)

Figure 5.13: *Tomato field site: NDVI map before (**a**) and after (**b**) the crop rows extraction.*

5.5 Conclusions

This case study demonstrates that it is possible to perform crop row detection from high resolution UAV imagery, for different crop variety, including vineyard, orchard and horticulture. DSM, RGB or multispectral orthophotos can be used as input for the detection methods, in particular the DSM performs better with crop characterised by high heights (i.e., grapevine and pear), even in presence of inter-row weed, but it should be avoided to detect horticultural crops (i.e., tomato). Commercial RGB sensors give high accuracy values for crop row detection, therefore for this purpose it is not necessary to perform surveys mounting more expensive multispectral cameras, if no additional infrared information is required. Nevertheless, in presence of shadows produced by the crop canopy on the terrain, indices based on NIR band and classification algorithms can lead to an overestimation of the crop rows.

Although all methods need some level of human intervention, among all, the Local Maxima Extraction algorithm, ad hoc developed within this study, allows to have the best compromise in terms of time-cost, automation and quality of the results. Bayesian segmentation applied on VIs performs better than the other methods in presence of bare soils, but it is dependent on a-priori information.

Finally, these detection methods could be used to derive specific information on crop canopy to be used to optimise on-farm irrigation management.

CHAPTER 6

Data fusion for delineating Site Specific Management Zones. – An experiment on a vineyard

Site-specific management of water and nutrients in PAg requires the delineation in the field of sub-regions with similar soil and crop characteristics affecting crop yield, namely Site Specific Management Zone (SSMZ) (Nawar et al., 2017). Intensive and relatively time-saving measurements of soil electrical conductivity (EC) through geophysical proximal soil sensors are among the most frequently used approaches in PAg to delineate SSMZs (Corwin et al., 2003, Morari et al., 2009, Moral et al., 2010, Van Meirvenne et al., 2013, Neupane and Guo, 2019). Statistical procedures (Pascucci et al., 2018) are used to classify the EC maps derived by interpolation of the geophysical data, resulting in few sub-field zones to be managed separately. EC maps are considered to delineate SSMZs because EC is influenced by a combination of soil physical-chemical properties affecting crop yield, including soluble salts, clay content and mineralogy, soil water content, bulk density, organic matter, and pH.

Ancillary data acquired by spectral sensors in the visible (VIS), near-infrared (NIR) and thermal infrared (TIR) regions shall be combined with EC data to characterize the soil spatial variability (Corwin, 2008) and to improve the delineation of SSMZs (López-Lozano et al., 2010, Scudiero et al., 2013). Indeed, NIR reflectance from soil has been correlated with many soil properties, including total C, total N, water content and texture (Chang et al., 2001, Rossel et al., 2006. The most recent literature stresses the importance to consider multi-sensor data to optimally delineate SSMZs (Shaddad et al., 2016, Castrignanò et al., 2017, Scudiero et al., 2018, Anastasiou et al., 2019, Martínez-Casasnovas et al., 2018). An approach to improve the delineation of SSMZ by considering multi-sensor data describing both crop and soil variability is illustrated in De Benedetto et al. (2013). In non-flat areas, as often in cases of vineyards, also topography can influence soil water condition (see Chapter 4) and consequently crop yield and field zonation; in this situation SSMZ delineation may be improved by integrating geophysical soil monitoring data with topography data (Priori et al., 2013).

In this case study, it is presented the implementation of data fusion procedures to delineate a SSMZ map in a vineyard of 1.5 ha located in Franciacorta (province of Brescia, Italy), since this information is crucial for the elaboration of irrigation prescription maps to be used for the design and/or the management of variable-rate irrigation systems. In particular, the study shows how the different types of data which can be involved in the SSMZ delineation are acquired and analysed, and finally integrated through a data fusion approach. To assess the reliability of the SSMZ maps obtained from different types of data, each of them was compared with data acquired with a thermal infrared (TIR) survey carried out in a hot and dry period of the agricultural season 2017, in a phase of the crop phenology during which the vine is normally most sensitive to water stress.

6.1 Materials and methods

6.1.1 Study area

The experimental site is a rainfed vineyard of 1.5 ha located in Franciacorta (Erbusco, 575813 E, 5050828 N, Northern Italy), a rolling hills area south-east of the Iseo Lake (Figure 6.1).

Figure 6.1: *The experimental site; Coordinate Reference System (CRS): WGS84/UTM zone 32 N. Map data: ©OpenStreetMap contributors.*

Soils of this site are sandy-loam in texture, according to the regional 1:250.000 soil map (http: //www.geoportale.regione.lombardia.it). They belong to the land system of "intermediate moraine deposits". In this area, the typic Paleudalf coarse loamy and poorly gravelly soils (CZO1), are associated with more skeletal soils, very deep, with moderately faster permeability and drainage (VBO1) (Usda, 2004).

In the Franciacorta region, the climate is continental, with the lake providing a mitigating effect in both summer and winter. Considering the average monthly values of the main agrometeorological variables registered at the Erbusco station (part of the Lombardy regional monitoring network), located 2 km far from the experimental site, for the period 2008-2018, it can be observed that the minimum and maximum monthly rainfall occur respectively in July (70 mm) and October (85 mm), while the minimum and maximum daily air temperatures vary, respectively, from 7°C in October to 20°C in July, and from 16°C in October to 32°C in July. Figure 6.2 shows the behavior of the main agrometeorological variables recorded at the Erbusco station during the experimental period June-August 2017.

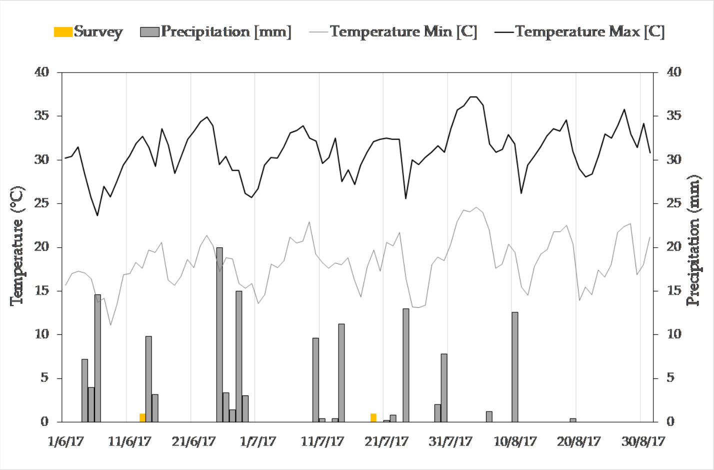

Figure 6.2: *Precipitation and temperature daily data collected at the agrometeorological station of Erbusco, during the experimental period from June to August 2017.*

6.1.2 Experimental surveys

Different types of data were collected in the vineyard to describe all the factors affecting crop yield, related to the hydrological condition of the soil, as well as to the crop vigor and water status. The soil properties were detected through an electro-magnetic induction (EMI) sensor, while the topography of the vineyard and the crop properties were investigated through multispectral and thermal sensors mounted on UAV. Various combinations of these data (i.e. data fusion) were analyzed, to assess their effectiveness in improving the delineation of the SSMZs aimed at optimizing the crop yield (see Section 6.1.3 for more details).

Soil survey through EMI sensors

The soil variability was detected through an EMI survey on 14th June 2017, when the soil water content might be considered close to the field capacity (FC), few days after a three-day period of rainfall that resulted in 26 mm of rain (Figure 6.2).

The geophysical data were collected with the multi-frequency EMI sensor Profiler EMP-400 (GSSI Inc., Nashua, NH USA). The EMI sensor worked with up to three different frequencies from 1 to 16 kHz (15 kHz, plus at most two other frequencies), corresponding to decreasing Depths of Exploration (i.e. DoE). Two frequencies were selected for the survey, 15 kHz (DoE about 1.5 m) and 10 kHz (DoE about 2.5 m), to explore the soil in contact with the vineyard's root system, which is usually 2-3 m deep. The data were acquired along parallel rows with an interdistance of 10 m, while vineyard rows have an interdistance of 2 m. In the portions of the fields characterized by gravelly soils the EMI measurements showed not to be valid, since the EC values were found to be negative. This extreme soil texture was more present in the upper part of the soil profiles (investigated with the sensor operating at higher frequencies), and showed to have a lower weight as the depth increases.

Vegetation and topography survey through UAV multispectral and thermal imagery

Vegetation survey was conducted by means of an aerial campaign with sensors mounted on an UAV. The survey took place on 19$^{\text{th}}$ July 2017, under sunny and clear blue-sky conditions. The daily average air temperature was 26°C, with a maximum value of 31°C during the central hours of the day. The survey was conducted during the veraison phenological stage, in which the crop is more sensitive to crop water stress.

The UAV employed for the survey was the HexaKopter (MikroKopter, Moormerland, Germany). It is a multirotor equipped with six brushless motors, it weighs about 1.2 kg, including batteries, and its maximum transportable payload is equal to 0.5 kg. It can be remotely controlled and programmed for automatic navigation through the free and open source Mission Planner software (http://ardupilot.org/planner/index.html). Its maximum transmission range is about 200 m and the flight duration is limited to 10 minutes.

The UAV was equipped with three different sensors, in order to collect imagery in different portions of the electromagnetic spectrum: VIS (450 - 720 nm), NIR (800 - 1000 nm) and TIR (7000 - 14000 nm). The Survey2 camera (MAPIR, San Diego, CA, USA) was used for VIS acquisitions, while a modified SJ4000 camera (SJCAM, Shangxue Technology Park, Putian, Shenzhen, China) was used to collect NIR imagery. Both instruments are low cost and light-weight cameras, with a CMOS sensor of maximum size 16 Mpx. TIR data were collected by the thermal camera OPTRIS PI400 (Optris Gmbh, Berlin, Germany), with a spectral response in the range 7.5 - 13 μm. The thermal camera acquires data in radiometric video sequences format (.RAVI). For the photogrammetric processing, single frames with resolution equal to 382 x 288 px are subsequently extracted from the video. Technical specifications of the three sensors used for the vegetation survey are reported in Table 6.1.

Table 6.1: *Technical specifications of the three cameras used for the vegetation survey.*

	Survey2	**SJ4000**	**OPTRIS PI400**
Acquisition	VIS	NIR	TIR
Focal length (mm)	4.35	4.35	8
Sensor size (mm)	4.86 x 3.64	4.86 x 3.64	9.55 x 7.2
Sensor size (px)	4032 x 3024	4032 x 3024	382 x 288
Pixel size (μm)	1.2	1.2	25
Field of View (FOV)	82°	82°	62° x 49°
Output format	JPEG image	JPEG image	RAVI video
Weight (g)	64	64	380

According to the UAV payload, two flights were required to collect images with the three sensors. During the first flight, the UAV mounted the Survey2 and the SJ4000 cameras simultaneously, in order to acquire a multispectral dataset. Considering sensors characteristics and study area, flight planning included six strips at an altitude of

60 m above ground level (AGL), with forward and side overlaps equal to 80% and 65%, respectively. Two blocks of data (VIS and NIR) were acquired, each amounting 164 images with ground resolution, namely Ground Sample Distance (GSD), equal to 0.017m. The adopted plan for the multispectral flight is reported in Figure 6.3.

During the second flight, the UAV mounted the OPTRIS PI400 to collect data of vegetation temperature. The video sequences were acquired with nadiral orientation at a constant speed of 2.7 m/s and at the altitude fixed to 55 m AGL. The derived images had a GSD of about 0.150 m and forward and side overlaps equal to 80% and 40%, respectively. The georeferencing and the accuracy of the photogrammetric products were achieved by means of some targets used as Ground Control Points (GCPs), whose center coordinates were measured through a Global Navigation Satellite System (GNSS) receiver. The GNSS receiver Leica Viva GS14 (Leica Geosystems, Heerbrugg, Switzerland) in Network Real Time Kinematic (NRTK) mode was used in this study, with horizontal and vertical accuracies of 2-3 cm and 5 cm, respectively. Different types of targets were used for multispectral and thermal surveys: 16 black and white plastic square panels (30 cm x 30 cm) were employed for the multispectral survey, while 16 polystyrene square panels (60 cm x 60 cm), covered with aluminum foil and marked with a copper cross to enhance the central point were used for the thermal survey. In order to have an optimal distribution of GCPs, the targets were placed both all around the perimeter of the vineyard, on the ground, and inside the investigated area, on the top of the vineyard poles to ensure their visibility. Moreover, some targets with known reflectance and thermal characteristics were imaged, to perform radiometric calibration of VIS-NIR data and atmospheric correction of TIR images. According to Labbé et al. (2012), 4 polystyrene square panels (60 cm x 60 cm), covered with plastic, where used for the atmospheric correction of the thermal images. The panels, two white panels (i.e. cold target) and two black panels (i.e. hot target) were placed outside the investigated area in two different positions.

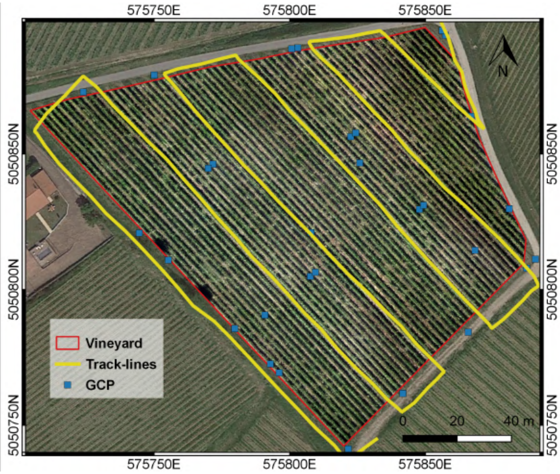

Figure 6.3: *Flight track-lines for multispectral images acquisition and Ground Control Points (GCPs) distribution. Map data: ©Google Satellite.*

6.1.3 Methodological approach to delineate SSMZs through data fusion

Different types of data − geophysical data acquired through EMI sensors, and topographic and crop data acquired through the multispectral VIS-NIR sensors mounted on the UAV − were variously combined to delineate SSMZs. A data fusion approach was considered, by applying multivariate statistical methods (i.e., Principal Component Analysis, PCA) to integrate the different types of data. Precisely, the PCA was applied to the maps elaborated from geophysical and VIS-NIR data as explained in Section 6.2.1. Moreover, the CWSI map was elaborated from the imagery acquired through the TIR sensor mounted on UAV. CWSI was calculated as expressed in the following formula:

$$CWSI = \frac{T_s - T_{wet}}{T_{dry} - T_{wet}} \tag{6.1}$$

where T_s is the crop surface temperature, T_{wet} is the lower boundary of crop temperature corresponding to the water status of a leaf with stomata fully open and a maximum transpiration rate, T_{dry} is the upper boundary of crop temperature corresponding to the water status of a non-transpiring leaf with stomata completely closed.

The CWSI map was used to assess the effectiveness of the SSMZ delineation obtained from different combination of data even though crop yield maps are usually considered for this purpose. In this study, in absence of this type of information, the CWSI map was used as a proxy of the crop yield map. As a matter of fact, the crop water status (described through the CWSI) is assumed to be the main environmental factor affecting crop yield in this rainfed vineyard. Areas in CWSI map with low values (i.e. good crop water status) were expected corresponding to areas with high soil water contents (i.e. high EC values and/or high NDVI values and/or low topographic slope values).

Particularly, the effectiveness of the data fusion approach to enhance the delineation of SSMZs was assessed by applying the methodology hereinafter explained and illustrated in Figure 6.4. Two separated areas were defined within the vineyard, because of the occurrence of not valid EMI measurements for gravelly soils (Section 3.1.2). In the first area (called “a”), characterized with valid EMI measurements, geophysical and VIS-NIR data were available; in the second area (called “b”), characterized with not valid EMI measurements, only VIS-NIR data were available. For each area, maps produced from different combinations of data were fused by applying PCA. Consequently, the SSMZs were elaborated (for each area, “a” and “b”) from the integrated maps produced through PCA (i.e. maps of the Principal Components, PCs) by applying Cluster Analysis (CA) through the Management Zone Analyst (MZA) software (Fridgen et al., 2004). MZA implements an unsupervised fuzzy classification method and determines the optimal number of SSMZs through the minimization of both the indices Normalized Classification Entropy index (NCE) and Fuzziness Performance Index (FPI); the NCE measures the degree of disorganization among zones (the larger the NCE, the higher is the amount of disorganization), the FPI measures the degree of separation between zones (the larger the FPI, the stronger is the membership sharing between zones). Specifically, the CA was applied considering only the PC maps representing most of the variability of the input maps.

For the area “a”, the following three cases were analyzed: (1) only geophysical data were considered: the SSMZs were delineated based on the EC maps relative to different soil depths; (2) geophysical data were considered together with the topographic data obtained from VIS-NIR imagery: elevation and slope maps as well as EC maps referred to different soil depths were used to delineate SSMZs; (3) the complete dataset including also crop data was considered: the SSMZs were delineated by integrating the NDVI map with all the previously illustrated maps. NDVI map was elaborated from VIS-NIR imagery, as the index is defined as the normalised difference between NIR and Red bands (Rouse Jr et al., 1974).

For the area "b", the following two cases were analyzed: (1) the topographic data obtained from VIS-NIR imagery were considered: elevation and slope maps were used to delineate SSMZs; (2) the complete dataset, including topographic and crop data, was considered: the SSMZs were delineated by integrating the NDVI map with elevation and slope maps.

For each case, the SSMZ map was validated through a comparison with the CWSI map. The accuracy of the correspondence between SSMZ and CWSI map was analysed considering the distributions of the CWSI values within each SSMZ.

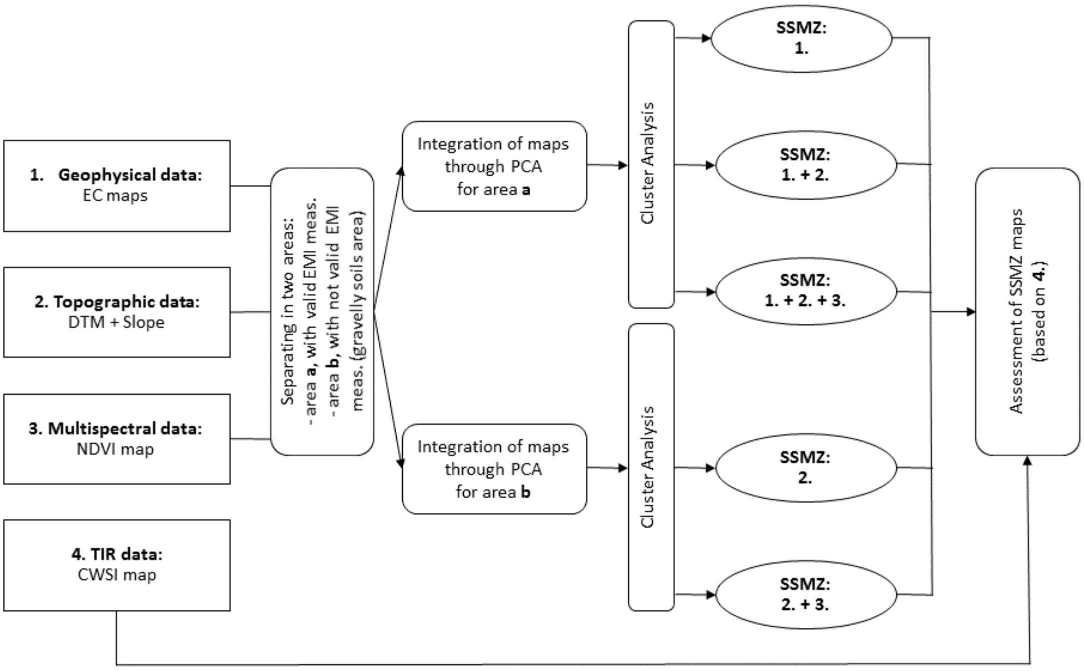

Figure 6.4: *Scheme of the methodological approach adopted in this study.*

6.2 Results

6.2.1 Soil, vegetation and topography mapping

EC maps

The EC measurements obtained for each frequency used with the EMI sensor (15 kHz and 10 kHz) were interpolated on a grid with 2 m pixel size. Two EC maps were obtained (Figure 6.5), each one relative to a different DoE corresponding approximatively to 1.5 m and 2.5 m, respectively. Red color area (area "b") in each map of Figure 6.5 corresponds to gravelly soils, for which the EMI measurements were not valid, because of the very low EC values characterizing those soils. In these zones, negative EC values were obtained from the EMI survey. The total extent of these areas decreases with the increasing DoE.

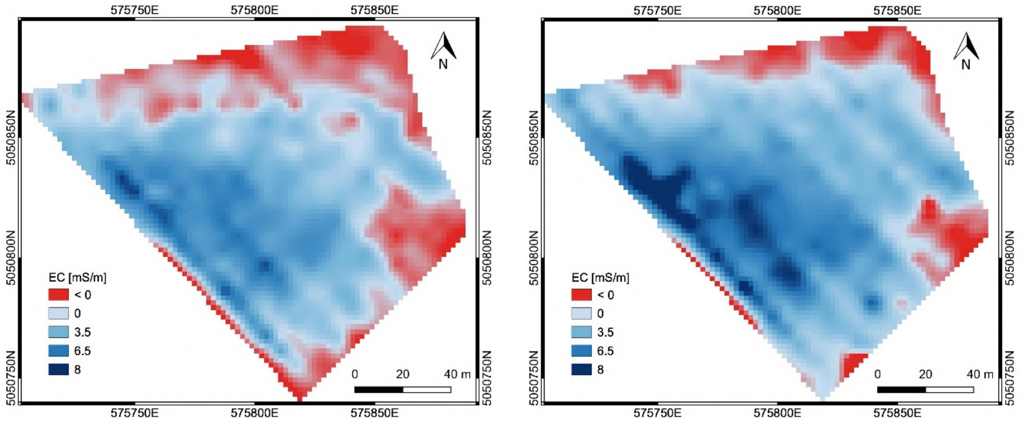

(a) (b)

Figure 6.5: *The obtained EC maps (mS/m): (**a**) frequency 15 kHz, corresponding to a DoE of 1.5 m; (**b**) frequency 10 kHz, corresponding to a DoE of 2.5 m. Red color area (area "b") corresponds to gravelly soils (EMI measurement not valid).*

Topography and slope maps

The VIS and NIR imagery blocks were processed through standard photogrammetric workflow (Ronchetti et al., 2018) with the Agisoft Photoscan Professional software version 1.2.6. Finally, the Digital Surface Model (DSM) was produced with spatial resolution equal to 0.05 m, representing the height model for both vegetation and soil.

In order to reconstruct the soil topography, vegetation pixels were detected and removed from the DSM. Vegetation detection was performed on DSM by using an algorithm developed by the authors, which assumes that pixels with higher elevation values correspond to vegetation, widely discussed in Chapter 5. The algorithm detects as vegetation pixels, all pixels which values are greater than a user-defined threshold within a moving window. In a second step, vegetation pixels were subtracted from the DSM, thus producing a model representing the height of the terrain, namely the Digital Terrain Model (DTM) of the study area. Figure 6.6 shows the DSM and the DTM of the vineyard, obtained after photogrammetric processing and vegetation detection and removal, respectively. The final DTM reported in Figure 6.6b, obtained after the application of a moving average smoothing filter, has a spatial resolution of 2 m.

Slope and contour line maps were derived from the DTM, by using the *Raster Terrain Analysis* functions in QGIS version 3.2. A fixed interval of 1 m was set for the generation of the contour lines, while the slope map was computed as the gradient of the terrain model, having the same spatial resolution of the DTM (i.e. 2 m). Final results are shown in Figure 6.7.

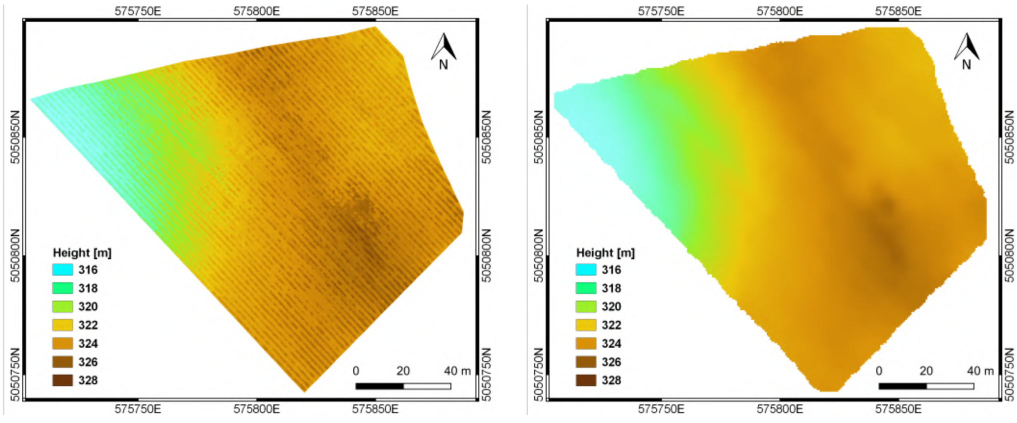

(a) (b)

Figure 6.6: *DSM (**a**) and DTM (**b**) produced through photogrammetric processing of multispectral (VIS-NIR) dataset.*

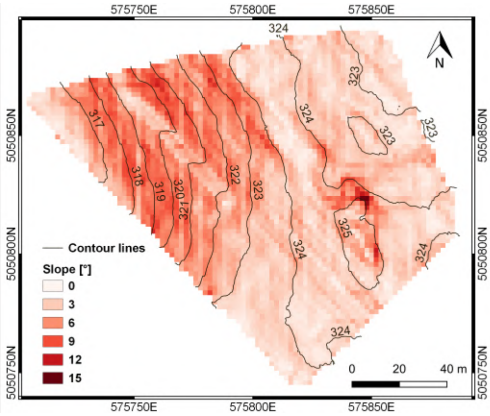

Figure 6.7: *Slope map and contour lines derived from the DTM.*

Vegetation indices maps (NDVI and CWSI)

Multispectral VIS-NIR and TIR imagery were used to compute the vegetation indices NDVI and CWSI, commonly adopted to describe vegetation vigor and crop water status respectively.

VIS-NIR orthomosaic was generated in Digital Number (DN) with a spatial resolution of 0.05 m, then converted in reflectance values, through the radiometric calibration obtained with an empirical line correction approach (Smith and Milton, 1999). Images of the radiometric targets were used to compute the linear regression coefficients of the DN values against the reflectance values from the target surface. The orthomosaic corrected through the radiometric calibration was used to obtain the NDVI map. Moreover, soil was masked out, to avoid the inclusion of soil pixels in the vegetation maps. The soil mask was created by extracting pixels that were not considered to be vegetation, as described in Section 6.2.1. Figure 6.8 shows NDVI maps before and after the soil pixel removal. From the graphs showing the frequency distribution of the NDVI maps (Fig. 6.8b and 6.8d), it is evident that the most of the pixels with NDVI values lower than 0.7 – corresponding to soil and inter-row weed – could be removed and only vegetation pixels (NDVI values greater than 0.7) were retained. The CWSI map was obtained from the TIR orthomosaic. The TIR orthomosaic (with spatial resolution equal to 0.15 m) was generated through a specific procedure for TIR images. This procedure, including single frames extraction, format conversion and photogrammetric processing, is described in detail in Tucci et al. (2019). Atmospheric correction of the obtained TIR orthomosaic was performed by using the thermal images of the cold and hot targets, representing respectively the minimum (T_{min}) and the maximum (T_{max}) temperature values within the investigated area. The temperature of the targets was recorded at the ground level as well. These temperature values, acquired at flight height and at ground level, were used to derive an atmospheric model (Labbé et al., 2012) successively applied to the TIR orthomosaic to obtain the crop surface temperature (called crop surface TIR orthomosaic hereinafter). CWSI map was calculated as in Equation 6.1. The values T_{wet} and T_{dry} were initially determined by an empirical approach reported in many studies (Meron et al., 2003, Cohen et al., 2005, Gonzalez-Dugo et al., 2013, Gerhards et al., 2018). The value T_{dry} was calculated by using the current T_{air} plus 5 °K (Möller et al., 2006, Ben-Gal et al., 2009, Alchanatis et al., 2010), while the value T_{wet} was calculated as the mean of the coolest 5% vegetated pixels in the crop surface TIR orthomosaic. As for the NDVI map, soil was masked out from the

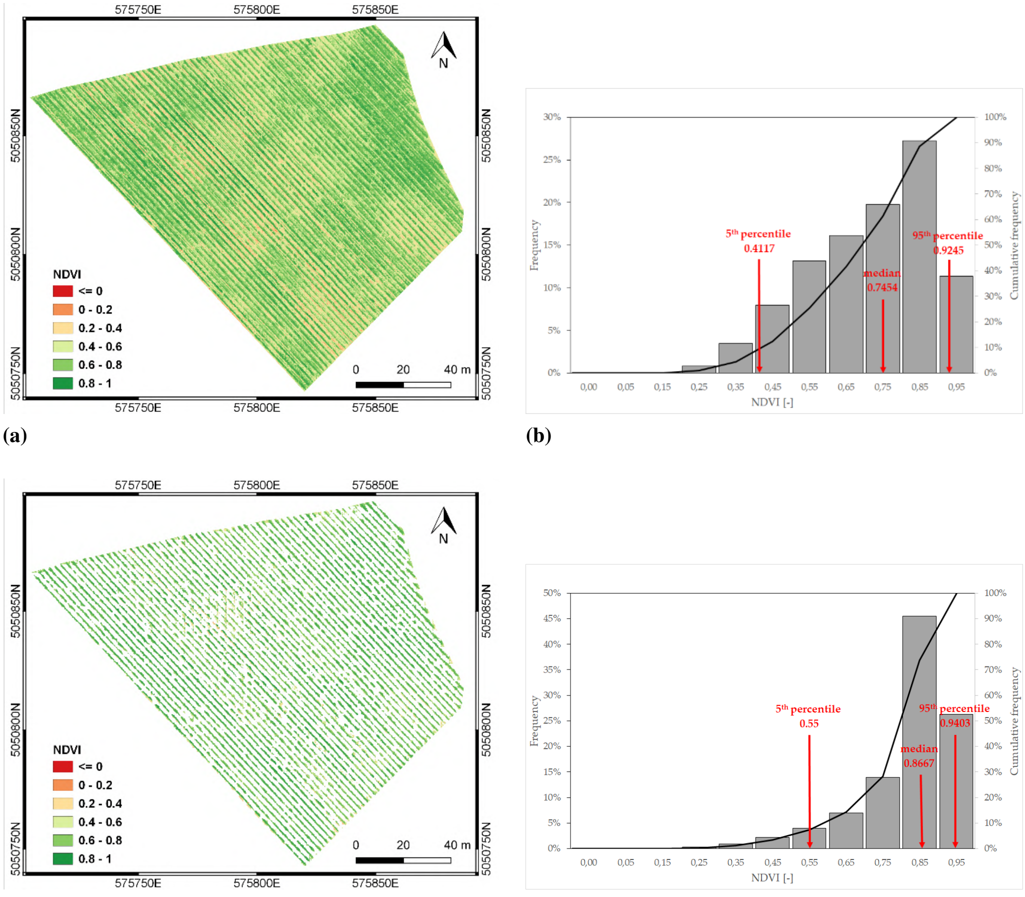

(a) (b) (c) (d)

Figure 6.8: *NDVI map before (**a**) and after (**c**) soil masking, together with their respective frequency distribution (**b**) and (**d**).*

crop surface temperature map. Figure 6.9 illustrates the CWSI maps before and after soil pixels removal. Both maps show a zone with values greater than 1, due to the presence of pixels with surface temperature higher than T_{dry}. This could be due to the fact that, in this study, T_{air} (31°C) was the average hourly temperature registered during the central hours of the day (from 1:00 p.m. to 2:00 p.m, solar time) at the Erbusco agro-meteorological station, placed 2 km away from the experimental site and positioned over a standard grass surface as indicated by WMO (World Meteorological Organization). In order to estimate a more reliable value for T_{dry}, the same approach used for T_{wet} was adopted: T_{dry} was calculated based on the temperature histogram (Park et al., 2017, Veysi et al., 2017, Bian et al., 2019) as the mean of the hottest 5% vegetated pixels in the crop surface TIR orthomosaic. The derived CWSI map, successively used in this study, is shown in Figure 6.10.

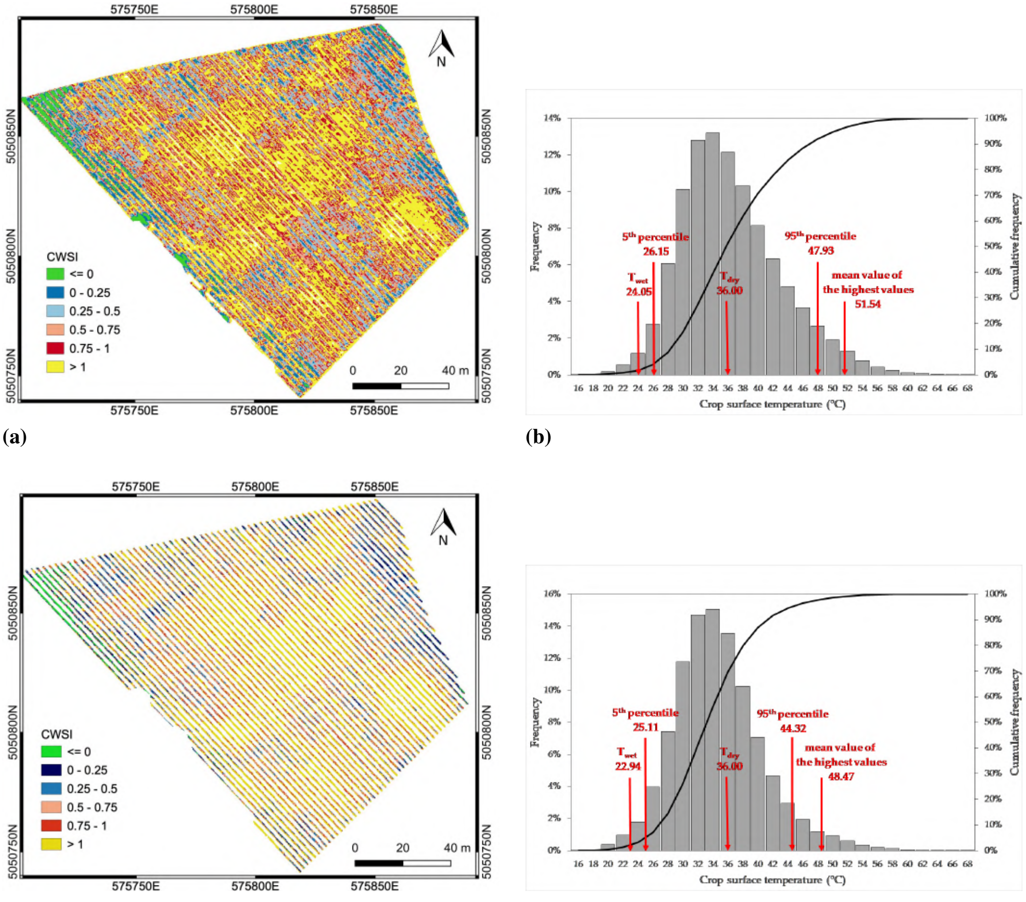

(a) (b)

(c) (d)

Figure 6.9: *CWSI map before (**a**) and after (**c**) soil masking. The frequency distribution of the crop surface temperatures, with the illustration of T_{wet} and T_{dry} values calculated according to the empirical approach described in Section 6.2.1, is reported for each case (**b**, **d**).*

6.2.2 SSMZ mapping

Firstly, the SSMZ map was elaborated from EC maps only (Section 6.2.2). Afterwards, topography and crop information were integrated with the EC maps through

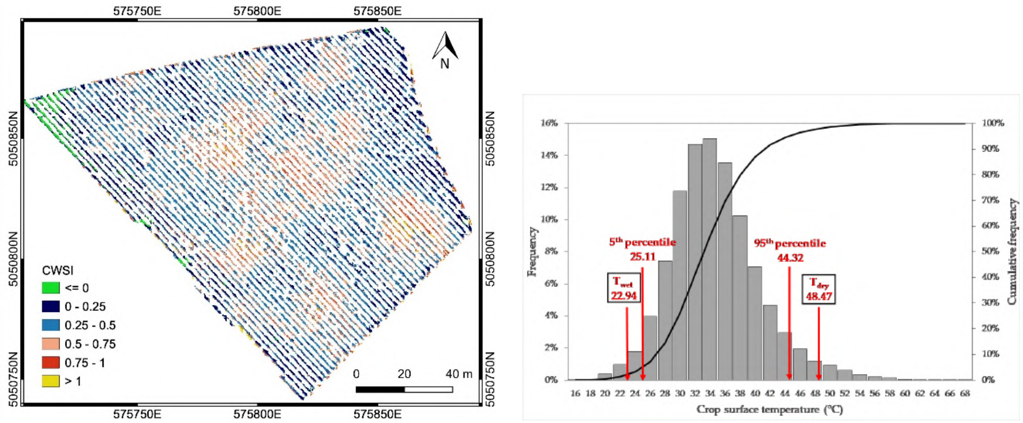

(a) **(b)**

Figure 6.10: *CWSI map after soil masking (**a**), derived considering the T_{wet} and T_{dry} values calculated as the mean of the coolest 5% and the hottest 5% vegetated pixels in the crop surface TIR orthomosaic, respectively. The frequency distribution of the crop surface temperatures is also reported (**b**).*

PCA, to improve the SSMZ map (Sections 6.2.2 and 6.2.2). The Pearson's correlation coefficients were computed separately for areas "a" and "b", respectively among the EC, DTM, Slope and NDVI values calculated at the grid nodes used to interpolate the EC data (2 m pixel size), with valid EMI measurements (Table 6.2), and among the DTM, Slope and NDVI values calculated at the nodes of the same grid, with not valid EMI measurements (Table 6.3). All the coefficient values are statistically significant with level 0.001 (p-value < $5x10^{-4}$). Moreover, the Moran Index was calculated to describe the spatial autocorrelation of the variables and the spatial cross-correlation between the variables. The values, calculated separately for areas "a" and "b", considering the nodes respectively inside and outside the vineyard's area with valid EMI measurements, are reported respectively in Tables 4 and 5. The Moran Index values were always statistically significant with level 0.001 (p-value < $5x10^{-4}$). The univariate Moran Index calculated for the different variables was always positive and greater than 0.60, showing a high spatial autocorrelation of all the variables. The bivariate Moran Index (between variables) describes the correlation based on the relationships between each point and the neighborings. According to Chen (2015), the correlation described through the Pearson's coefficients can be decomposed in two components, related to a direct correlation without distance effect and an indirect correlation based on the distance effect. Consequently, the difference between the Pearson's coefficient and the Moran Index quantifies the direct correlation component. For the two datasets described in Tables 6.4 and 6.5, this difference was always less than 0.03 in absolute value, equal to the 25% of the correlation coefficient at most, except for the correlation between the variables EC-15kHz and EC-10kHz (Table 6.4) and between the variables DTM and Slope (Table 6.5). These results highlighted the relevant contribution of the spatial pattern in cross-correlation.

Delineation of SSMZs from EC maps

The two EC maps relative to frequencies 15 kHz and 10 kHz, calculated within area "a" considering only the valid EMI measurements (i.e., not negative EC values), were analyzed through the PCA. The SSMZ map (Figure 6.11) was obtained by applying CA to the first PC, explaining about 96% of the variability of both EC maps. Three SSMZs were delineated within area "a"; another SSMZ (red color) was defined, corresponding to area "b" characterized with not valid EMI measurements (i.e., negative EC values) occurred for gravelly soils (Figure 6.5). SSMZs from 1 to 4 (Figure 6.11) correspond to decreasing EC values.

Table 6.2: *Pearson's correlation coefficients among the variables used to delineate SSMZ, estimated considering the grid nodes with valid EMI measurements (area "a").*

	EC-15 kHz	**EC-10 kHz**	**DTM**	**Slope**	**NDVI**
EC-15 kHz	1	0.93[1]	-0.20[1]	0.23[1]	-0.22[1]
EC-10 kHz		1	-0.29[1]	-0.26[1]	-0.21[1]
DTM			1	-0.40[1]	-0.19[1]
Slope				1	-0.07[2]
NDVI					1

Table 6.3: *Pearson's correlation coefficients among the variables used to delineate SSMZ, estimated considering the grid nodes with not valid EMI measurements (area "b").*

	EC-15 kHz	**EC-10 kHz**	**DTM**	**Slope**	**NDVI**
EC-15 kHz	-	-	-	-	-
EC-10 kHz		-	-	-	-
DTM			1	-0.40[1]	-0.12[2]
Slope				1	-0.08[3]
NDVI					1

Table 6.4: *Moran Index among the variables used to delineate SSMZ, estimated (using GeoDa software, by Luc Anselin) considering the grid nodes with valid EMI measurements (area "a").*

	EC-15 kHz	**EC-10 kHz**	**DTM**	**Slope**	**NDVI**
EC-15 kHz	0.82[2]	0.79[2]	-0.20[2]	0.23[2]	-0.24[2]
EC-10 kHz		0.81[2]	-0.28[2]	0.27[2]	-0.22[2]
DTM			0.99[2]	-0.40[2]	-0.19[2]
Slope				0.63[2]	-0.07[2]
NDVI					0.76[2]

SSMZ and CWSI maps were compared. High EC values (i.e. high soil water contents) were expected to correspond with low CWSI values (i.e. good crop water status). Instead, areas with high CWSI values, denoting crop water stress, were included in the SSMZ 1 (characterized by high EC values), while, viceversa, areas with low CWSI values were present in the SSMZ 4 (very low EC values). The analysis showed that for the

---

[1] p-value < $5x10^{-5}$;

[2] p-value < $5x10^{-4}$;

[3] p-value < $5x10^{-3}$

Table 6.5: *Moran Index among the variables used to delineate SSMZ, estimated (using GeoDa software, by Luc Anselin) considering the grid nodes with not valid EMI measurements (area "b").*

	EC-15 kHz	**EC-10 kHz**	**DTM**	**Slope**	**NDVI**
EC-15 kHz	-	-	-	-	-
EC-10 kHz		-	-	-	-
DTM			0.96^2	-0.59^2	-0.15^2
Slope				0.69^2	-0.09^2
NDVI					0.66^2

study vineyard, physical-chemical soil properties described by the EC values where not sufficient to explain the crop water status. As matter of fact, the spatial pattern of the SSMZs is quite different from that one of the zones in the CWSI map correspondent to low index values (from 0 to 0.5) and high index values (from 0.5 to 1).

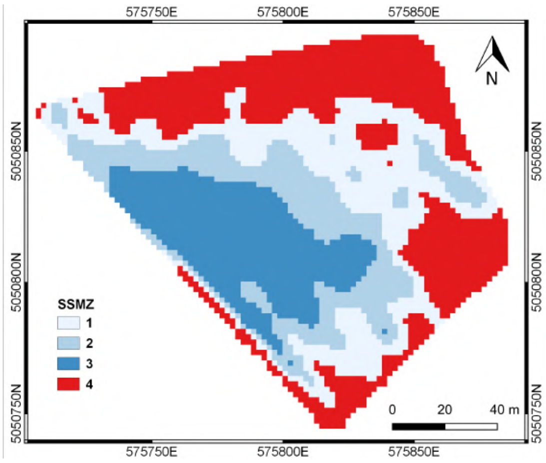

Figure 6.11: *The SSMZ map obtained from the EC maps relative to frequencies 15 kHz and 10 kHz. SSMZ from 1 to 4 corresponds to decreasing EC values; in particular, SSMZ 4 corresponds to negative EC values, due to gravelly soils.*

Data fusion: delineation of SSMZs from slope and EC maps

The combined effect of soil properties (i.e. EC values) and field topography (i.e. elevation and slope) was investigated to improve the delineation of SSMZs, looking for a better correspondence with the spatial distribution of the zones in CWSI map with low and high index values. EC, elevation and slope maps were analyzed through PCA. The SSMZ map was obtained by applying CA to the first and second PCs explaining most of the variability of all the considered maps. Particularly, PCA and CA were applied separately to the area "a" with valid EMI measurements, corresponding to SSMZs from 1 to 3 in Figure 6.11, as well as to the gravelly soil area "b", corresponding to SSMZ 4 in Figure 6.11.

In the former area, four SSMZs (numbered from A1 to A4 in Figure 6.12a), were delineated considering EC, elevation and slope maps. In the latter area, three SSMZs (numbered from B1 to B3 in Figure 12a) were recognized taking into account only elevation and slope maps. The resulting SSMZ map is shown in Figure 6.12a. This map, even though improved with respect to that obtained from EC maps only (Figure 6.11), could not completely explain the spatial variability detected in the CWSI map. Indeed, as illustrated also in Figure 6.13 showing the distributions of the CWSI values within each SSMZ, the SSMZs A1 and A2 (high EC values) corresponded to low CWSI values (as expected), as well as for the SSMZ B1 and part of the SSMZ B2; on the other hands, SSMZs A3 and A4 included areas with both low and high CWSI values (not expected due to the low EC values), as for the cases of SSMZ B3 and part of B2. This behavior highlighted how the zonation shown in Figure 12a did not consider all the factors affecting the crop water status.

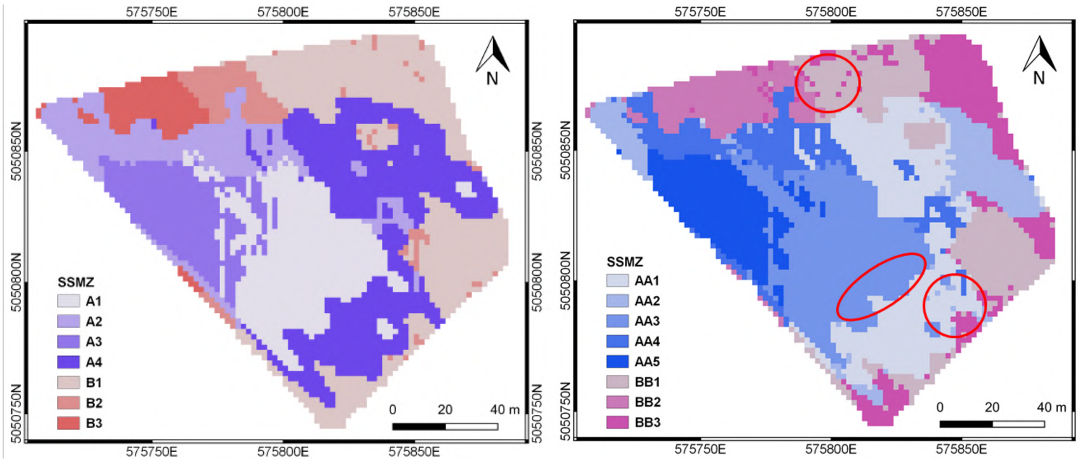

(a) **(b)**

Figure 6.12: *The SSMZ map obtained from: (**a**) EC, elevation and slope maps; (**b**) EC, elevation, slope and NDVI. In (**b**), red circles highlight the presence of small areas with low CSWI values in areas overall characterized by high CWSI values.*

Data fusion: delineation of SSMZs from soil maps (slope and EC maps) and NDVI map

Finally, also the variability of crop vigor (described by the NDVI map) was taken into account to produce a more reliable SSMZ map, with better correspondence to the zones in the CWSI map characterized by high (from 0.5 to 1) and low values (from 0 to 0.5) of the index. EC, elevation, slope and NDVI maps were analyzed through PCA and CA. Following the same approach considered in the Section 6.2.2, the SSMZ map was obtained by applying PCA and CA firstly to data available within the area “a” with valid EMI measurements, and afterwards to data available within the area “b” characterized by gravelly soils.

For area “a”, CA was applied to the first three principal components PC^{a_1}, PC^{a_2} and PC^{a_3} (Table 6.6), obtained from the EC, elevation, slope and NDVI maps: PC^{a_1} represented mainly the physical-chemical soil properties (correlation coefficients with EC greater than 0.90), and partly the DTM (correlation coefficient equal to -0.48); PC^{a_2} represented the topography (correlation coefficients with DTM and Slope equal to 0.72 and -0.45 respectively); PC^{a_3} represented both the topography (correlation coefficient with Slope equal to -0.61) and the crop vigor (correlation coefficient with NDVI equal to 0.59) which are negatively correlated (see Table 6.2). For area “b”, CA was applied

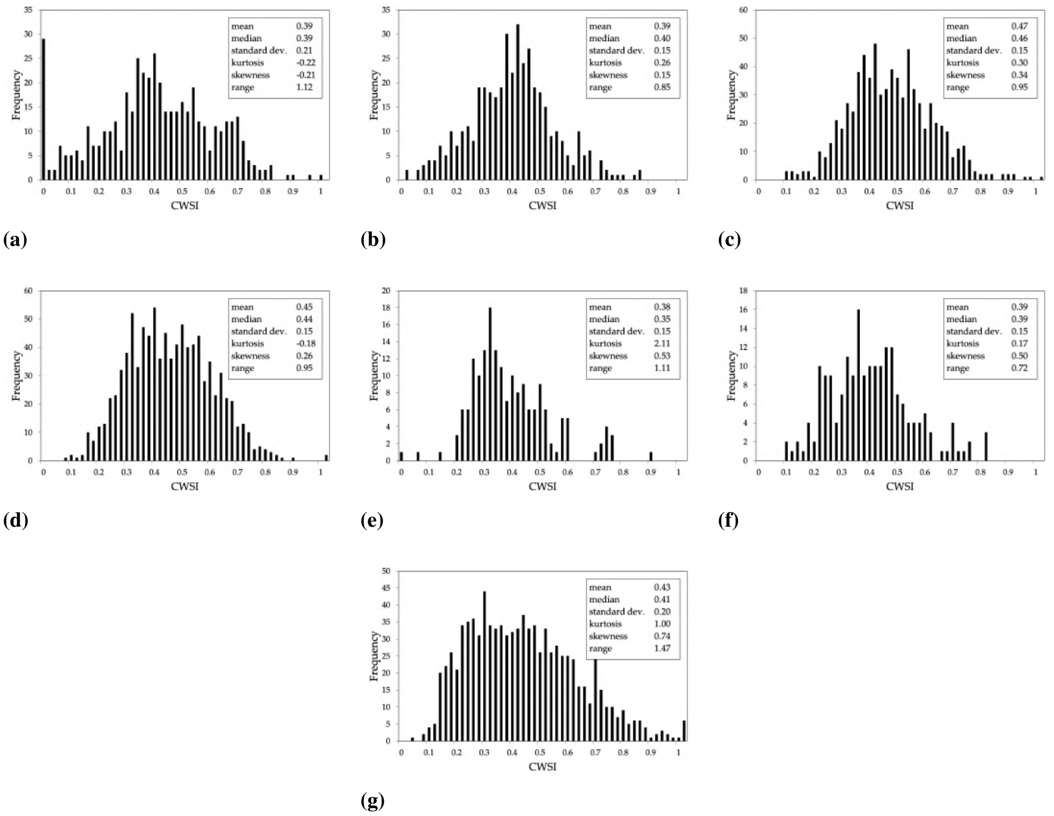

Figure 6.13: *Distribution of the CWSI values within each SSMZ shown in Figure 6.12a:* ***(a)*** *SSMZ A1,* ***(b)*** *SSMZ A2,* ***(c)*** *SSMZ A3,* ***(d)*** *SSMZ A4,****(e)*** *SSMZ B1,* ***(f)*** *SSMZ B2,* ***(g)*** *SSMZ B3.*

to the first two principal components PC^{b_1} and PC^{b_2} (Table 6.7), obtained from the elevation, slope and NDVI maps: PC^{b_1} represented the topography (correlation coefficients with DTM and Slope equal to -0.89 and 0.88 respectively); PC^{b_2} represented the crop vigor (correlation coefficient with NDVI equal to 0.99).

Within areas “a” and “b”, respectively, five SSMZs (numbered from AA1 to AA5) were delineated from EC, elevation, slope and NDVI maps, and three SSMZs (numbered from BB1 to BB3) were delineated considering only elevation, slope and NDVI maps. The resulting SSMZ map is shown in Figure 6.12b. The SSMZs AA1-AA3 , BB1 and BB3 corresponded to low CWSI values, while SSMZs AA4, AA5, and BB2 mostly corresponded to high CWSI values, except for the three small areas highlighted with the red circles in Figure 6.12b. As matter of fact, the SSMZ delineation in Figure 6.12b improved respect to that one shown in Figure 6.12a, as illustrated in Figure 6.14: i) the mean and the standard deviation of the CWSI values within SSMZ AA1 decreased, while SSMZs AA5 (corresponding to SSMZ A4 in Figure 6.12a) mostly included high CWSI values, with an increased mean value respect to that one for CWSI values within SSMZ A4 in Figure 6.12a; ii) also the mean of the CWSI values within SSMZs AA3 increased respect to the value for SSMZ A1 in Figure 6.12a; iii) the SSMZ BB2 is characterized with the highest mean of the CWSI values; iv) the SSMZ BB3 mostly included low CWSI values (the mean and the standard deviation of the CWSI values within this SSMZ decreased respect to the values for SSMZ B3 in Figure 6.12a).

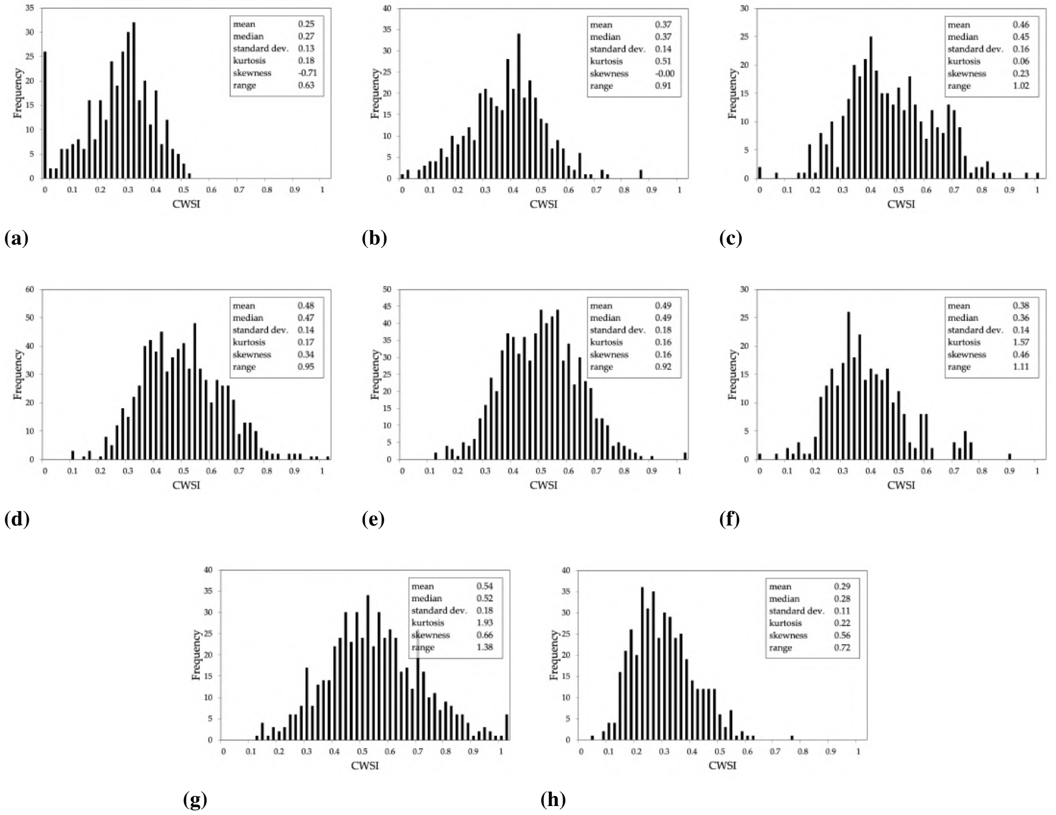

Figure 6.14: *Distribution of the CWSI values within each SSMZ shown in Figure 6.12b:* ***(a)*** *SSMZ AA1,* ***(b)*** *SSMZ AA2,* ***(c)*** *SSMZ AA3,* ***(d)*** *SSMZ AA4,****(e)*** *SSMZ AA5,* ***(f)*** *SSMZ BB1,* ***(g)*** *SSMZ BB2,* ***(h)*** *SSMZ BB3.*

Finally, the integration of the NDVI data allowed the delineation of SSMZs each corresponding to low or high CWSI values (except for the three small areas highlighted with the red circles in Figure 6.12b).

The spatial distributions of the PCs (Figure 6.15 and 6.16) explain which factors prevailed in the SSMZ delineation through CA. The SSMZs AA1-AA3 were mainly determined by soil properties (EC data, described by PC^{a_1}), while the SSMZ AA4, as well as the SSMZs BB1 and BB2, were mainly determined by topography (DTM and Slope data, described by PC^{a_2} for the case of SSMZ AA4, and by PC^{b_1} for the case of SSMZs BB1 and BB2). The SSMZs AA5 and BB3 were mainly determined by crop vigor (NDVI data, described by PC^{a_3} for the case of SSMZ AA5, and by PC^{b_2} for the case of SSMZ BB3).

Table 6.6: *Results of PCA applied in the area "a": variance of the principal components considered in CA and correlation coefficients with the variables used to delineate SSMZ.*

	Variance	Cumulative Var.	EC-15 kHz	EC-10 kHz	DTM	Slope	NDVI
PC^{a_1}	2.26	45%	0.90	0.93	-0.48	0.52	-0.27
PC^{a_2}	1.29	71%	0.25	0.18	0.72	-0.45	-0.69
PC^{a_3}	0.87	88%	0.28	0.26	0.03	-0.61	0.59

Table 6.7: *Results of PCA applied in the area "b": variance of the principal components considered in CA and correlation coefficients with the variables used to delineate SSMZ.*

	Variance	Cumulative Var.	DTM	Slope	NDVI
PC^{b_1}	1.56	52%	-0.89	0.88	-0.06
PC^{b_2}	1.03	87%	-0.14	0-0.20	0.99

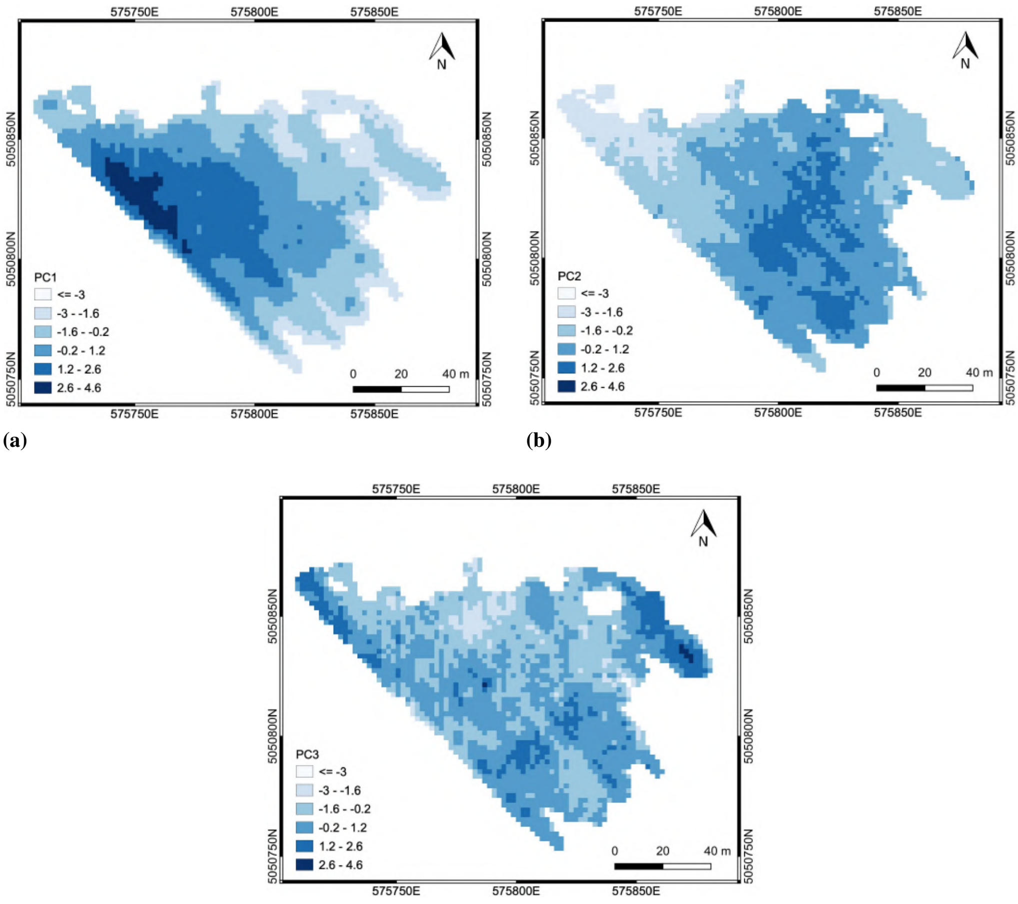

(a) **(b)**

(c)

Figure 6.15: *Results of the PCA applied in the area "a": spatial distribution of* **(a)** *PC^{a_1},* **(b)** *PC^{a_2},* **(c)** *PC^{a_3}.*

Moreover, Tables 6.8 shows the correlation between CWSI and the variables (elevation, slope and NDVI) used to integrate the EMI measurements in order to improve the reliability of the SSMZ map obtained from only EC data. Correlation with NDVI was the highest (p-values less than 5x10^{-4}), highlighting how NDVI data were able to explain the CWSI spatial variability within the whole field area. As matter of fact, for NDVI the difference between the Pearson's coefficient and the Moran Index, quantifying the direct correlation component independent from the spatial variability, is almost -0.30, while this component is almost zero for the other variables.

---

[1] p-value < 5x10^{-5};

[2] p-value < 5x10^{-4};

[3] p-value > 0.1

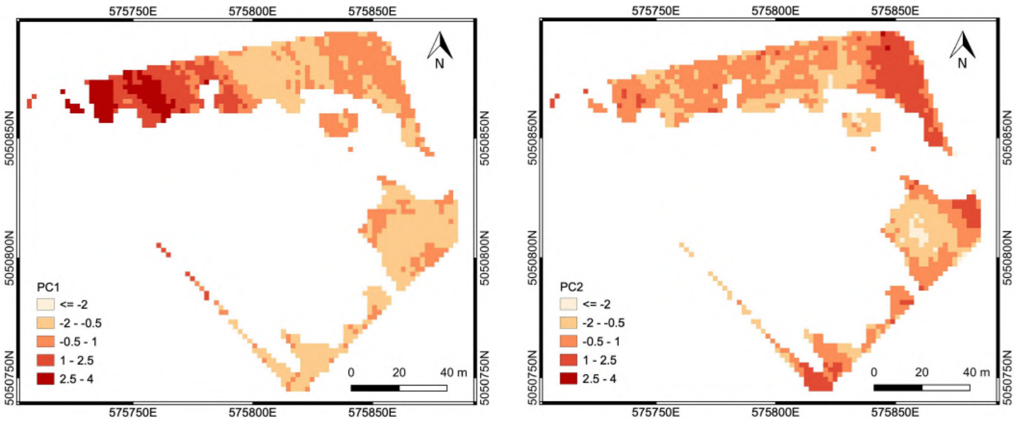

(a) **(b)**

Figure 6.16: *Results of the PCA applied in the area "b": spatial distribution of* ***(a)*** *PC^{b_1},* ***(b)*** *PC^{b_2}.*

Table 6.8: *Results of PCA applied in the area "b": variance of the principal components considered in CA and correlation coefficients with the variables used to delineate SSMZ.*

	DTM	**Slope**	**NDVI**
Pearson's coefficient	0.29^1	0.02^3	-0.71^1
Moran index	0.29^2	0.02^2	-0.52^2

6.3 Discussion

Obtaining a reliable SSMZ map is of practical relevance for farmers, since this map is an important tool to actuate variable rate practices in PAg, in term of both designing and managing application systems (e.g. for the water and nutrient management). As matter of fact, the delineated SSMZs are zones where the factors influencing the crop yield (i.e. soil, topography, and micro-climate) result in affecting the crop water status and vigour in a different way. These factors need to be adequately described through thematic maps, to allow the delineation of SSMZs through their combination.

This study proposed a fusion approach integrating different thematic maps (EC, DTM, slope and NDVI maps) to compute a SSMZ map, whose effectiveness was assessed considering a CWSI map. The approach was applied in a rainfed vineyard to obtain a SSMZ map useful for the design and the management of a variable rate irrigation system. By actuating a variable rate irrigation accordingly to the SSMZ map, farmers would achieve a twofold result: first, to obtain a higher and more uniform production and second, to optimize the water use.

Interesting general discussion points that emerge from the results of this study are the following:

1. the SSMZ map can vary greatly its spatial configuration depending on the information layers used for its production, it is therefore necessary to conduct more research aimed at understanding which information it may be appropriate to include, based not only on the prevailing factors affecting the crop yield, but also on the purpose for which the SSMZ map is being developed (e.g., nutrient management, water management);

2. the addition of the topographic information to the soil data included in the EC maps leads the SSMZ map to have a spatial distribution more similar to that shown by the CWSI map; it can be deduced that in a vineyard in slope conditions, the topographic information together with the soil distribution information are able to explain part of the variability illustrated in the vegetation maps;
3. in the specific case of this study (i.e., rainfed vineyard in severe water stress conditions), NDVI data were able to explain the CWSI spatial variability within the whole field area; indeed, the NDVI map showed a strong correlation with the crop water status (CWSI);
4. while information on soil properties and topography are not very variable over time, crop data may vary from year to year if soils and topography are not the only factors conditioning their distribution; it would therefore be necessary to repeat the study for several years to verify the stability over time of the spatial distribution of crop data;
5. if the SSMZ map is to be used to design a rigid variable-rate irrigation system (i.e., drip irrigation system subdivided into different irrigation sectors), considering that the geometry of the irrigation system (and consequently the irrigation amounts distributed) cannot be changed from year to year, it is even more important to verify the stability over time of the spatial distribution of crop data, and if therefore it makes sense to consider them in the delineation of the SSMZs.

6.4 Conclusions

Recent literature suggests that integrating EC information with elevation and slope maps, as well as with crop indices describing the crop vigor, can improve the delineation of SSMZs in vineyards. This was demonstrated in this study, focusing on the fusion of EC maps obtained by an EMI geophysical survey and VIS-NIR data collected through UAV-mounted cameras, to optimally delineate SSMZs in a rainfed vineyard. In the study, in absence of a spatially distributed crop yield map, the crop water status detected during the grape's veraison phenological stage was assumed to summarize the effect of the principal environmental factors acting on the crop production; consequently, the CWSI map was used as a proxy of the crop yield map itself.

The obtained results stressed how the crop water status in the study vineyard was actually affected significantly not only by the physical-chemical soil properties (described by the EC maps), but also by the elevation and slope of terrain. Moreover, the NDVI map allowed to include in the analysis time-dependent factors influencing the production (i.e. interaction among soil, topography, micro-climate and vegetation). In fact, for the study vineyard, a good correspondence between the spatial pattern of SSMZ and CWSI maps was achieved only by integrating the NDVI data to the other types of data. Consequently, at least for the study case, a reliable SSMZ map to be used to design and manage irrigation within the vineyard showed to require the availability of both 'stable-over-time information', related to soil properties and topography, and 'time-dependent information', related to the crop development. In this study, crop information was available only for the 2017 season, but a good practice to obtain reliable SSMZ maps would require the acquisition of crop data during different seasons.

CHAPTER 7

Conclusions and Perspectives

This dissertation gave a better understanding of advantages and limitations of performing UAV surveys for precision agriculture applications, mainly focusing on crop monitoring and management. Several open points were addressed, starting from the analysis of sensors, vehicles and flight strategies, passing through the study of methodologies for effective parameters extraction, up to the proposal to integrate UAV imagery with geophysical data acquired from ground-based platforms. The illustrated case studies derive from real practical needs that occurred during the PhD period. Starting from these it was possible to find solutions to the problems encountered and recommend guidelines for conducting UAV surveys in the agricultural sector. From each case study it was possible to extract important recommendations and the main guidelines are reported below.

A careful planning of the survey is relevant in any applications, together with proper choices during image processing. When working with multispectral sensors, radiometric calibration of data is required, anyhow it is recommended to assess accuracy of the calibration before using results, because significant radiometric distortions may be left. Radiometric errors are more evident especially on the edges of the acquired blocks, therefore to reduce this effect it is advisable to plan to survey a wider area that includes the area under investigation. Semi-automatic processing methods must be used with awareness, knowing their limitations and weaknesses.

To facilitate the spread of UAV surveys in agriculture, it is worth knowing that mass market very-light UAV can also be used, even if equipped with fisheye cameras. Recent advances in processing techniques compensate geometric distortions on images, in order to obtain high quality products. To optimize costs and times of the surveys, double grid flight configurations should be preferred to single direction flights, and placing any GCPs inside the field would not affect quality of final results, as long as the minimum number of necessary points is reached and that they are well distributed all around the surveyed area.

Precision Agriculture applications require to derive specific information on crop canopy. Vegetation parameters can be easily extracted from products generated by means of UAV imagery processing, whether they are DSM, RGB orthophotos or Vegetation Indices maps. Different methods have been developed aiming at detecting vegetation canopy and differentiating from soil background. The performances of the methods are generally good but vary greatly according to the characteristics of the input data, the level of automation of the algorithm and the peculiarities of the crops analyzed. Compared to orchards and horticultural crops, the extraction of rows in vineyards presents the greatest challenges, due to the concurrent presence of bare soil, weeds, and shadows in the inter-rows distance.

For responsible management of agronomic resources, the delineation of SSMZs can be improved by integrating EC information derived from ground-based sensors with elevation, slope and crop vigor maps retrieved from UAV surveys. To design and manage irrigation systems, it is required to collect information related to soil properties and topography, stable over the time, and time-dependent factors related to the crop development along the growing season, obtainable by means of very-high resolution UAV multispectral and thermal imagery.

Although several aspects have been addressed, the reported case studies are not exhaustive, and few problems have not been thoroughly investigated. Concerning data acquisition, this thesis has not dealt with the analysis of the optimal flight parameters for conducting surveys, namely image overlaps and flight height. Following a conservative approach, in the presented UAV surveys it was assumed that overlaps between images were always greater than 60% and flight heights fixed in order to guarantee a GSD of few centimeters. A recent study (Seifert et al., 2019) has demonstrated that flight parameters can influence surface reconstruction in forestry applications, it would be worthy to evaluate their effects also in agriculture. Regarding data processing, none of the reported studies specifically focused on BRDF corrections, despite being a topic of interest among researchers (Wierzbicki et al., 2018, Honkavaara and Khoramshahi, 2018). An open point remains what added value can bring performing BRDF corrections for operational uses in agriculture. Finally, this thesis refers only to applications with the concurrent use of UAV and satellite imagery. Further actions could be to study solutions to encourage the combined use of data acquired from both satellite and UAV platforms, in order to exploit the potential of both remote sensing systems. UAV surveys could be used on selected sites as training samples to calibrate satellite images and then enlarge the extension of the area under investigations. Other possible applications could be performing targeted UAV surveys on fields in which satellite data have highlighted some critical issues. In this direction, it is necessary that there is georeferencing and radiometric coherence between the collected data. The main issue to be solved is to make two such different data comparable, through the fusion of images with very different spatial resolutions. The launch of Sentinel-2 mission five years ago has increased research interest in this area and the first methodological proposals have been put forward (Zhao et al., 2019, Di Gennaro et al., 2019, Nonni et al., 2018, Martin et al., 2018). The next research activities will be certainly addressed to these perspectives.

List of Acronyms

AGL	Above Ground Level
B	Blue
BBA	Bundle Block Adjustement
BRDF	Bidirectional Reflectance Distribution Function
BS	Bayesian Segmentation
CA	Cluster Analysis
CHM	Canopy Height Model
CIR	Color InfraRed
CP	Check Point
CV	Computer Vision
CWSI	Crop Water Stress Index
DEM	Digital Elevation Model
DG	Direct Georeferencing
DN	Digital Number
DoE	Depths of Exploration
DSM	Digital Surface Model
DTM	Digital Terrain Model
EC	Electrical Conductivity
EM	ElectroMagnetic
EMI	ElectroMagnetic Induction
EO	External Orientation
FOSS	Free and Open Software System
FPI	Fuzziness Performance Index
G	Green
GCP	Ground Control Point
GIS	Geospatial Information System
GLCM	Grey Level Co-occurence Matrix
GNSS	Global navigation Satellite System
GPS	Global Positioning System
GSD	Ground Sample Distance

GUI	Graphical User Interface
ICP	Iterative Closest Point
IMU	Inertial Measurements Units
INS	Ineratial Navigation System
IO	Internal Orientation
LiDAR	Light Detection And Ranging
LME	Local Maxima Extraction
MDM	Minimum Distance to Mean
MZA	Management Zone Analyst
NCE	Normalized Classification Entropy
NDVI	Normalized Difference Vegetation Index
NIR	Near-InfraRed
NRTK	Network Real Time Kinematic
OA	Overall Accuracy
PA	Producer's Accuracy
PAg	Precision Agriculture
PC	Principal Component
PCA	Principal Component Analysis
R	Red
RE	RedEdge
RGB	Red-Green-Blue
RMSE	Root Mean Square Error
RS	Remote Sensing
S2	Sentinel-2
SfM	Structure from Motion
SSMZ	Site Specific Management Zone
TIR	Thermal InfraRed
TS	Threshold Selection
TWI	Topographic Wetness Index
UA	User's Accuracy
UAV	Unmanned Aerial Vehicle
VI	Vegetation Index
VIS	Visible

Bibliography

Aasen, H., Honkavaara, E., Lucieer, A., and Zarco-Tejada, P. J. (2018). Quantitative remote sensing at ultra-high resolution with uav spectroscopy: a review of sensor technology, measurement procedures, and data correction workflows. *Remote Sensing*, 10(7):1091.

Adão, T., Hruška, J., Pádua, L., Bessa, J., Peres, E., Morais, R., and Sousa, J. (2017). Hyperspectral imaging: A review on uav-based sensors, data processing and applications for agriculture and forestry. *Remote Sensing*, 9(11):1110.

Ajayi, O. G., Salubi, A. A., Angbas, A. F., and Odigure, M. G. (2017). Generation of accurate digital elevation models from uav acquired low percentage overlapping images. *International Journal of Remote Sensing*, 38(8-10):3113–3134.

Alchanatis, V., Cohen, Y., Cohen, S., Moller, M., Sprinstin, M., Meron, M., Tsipris, J., Saranga, Y., and Sela, E. (2010). Evaluation of different approaches for estimating and mapping crop water status in cotton with thermal imaging. *Precision Agriculture*, 11(1):27–41.

Anastasiou, E., Castrignanò, A., Arvanitis, K., and Fountas, S. (2019). A multi-source data fusion approach to assess spatial-temporal variability and delineate homogeneous zones: A use case in a table grape vineyard in greece. *Science of The Total Environment*, 684:155–163.

Atzberger, C. (2013). Advances in remote sensing of agriculture: Context description, existing operational monitoring systems and major information needs. *Remote sensing*, 5(2):949–981.

Barazzetti, L., Previtali, M., and Roncoroni, F. (2017). Fisheye lenses for 3d modeling: Evaluations and considerations. *ISPRS - International Archives of the Photogrammetry, Remote Sensing and Spatial Information Sciences*, XLII-2/W3:79–84.

Barnes, E., Clarke, T., Richards, S., Colaizzi, P., Haberland, J., Kostrzewski, M., Waller, P., Choi, C., Riley, E., Thompson, T., et al. (2000). Coincident detection of crop water stress, nitrogen status and canopy density using ground based multispectral data. In *Proceedings of the Fifth International Conference on Precision Agriculture, Bloomington, MN, USA*, volume 1619.

Bayes, T. (1763). Lii. an essay towards solving a problem in the doctrine of chances. by the late rev. mr. bayes, frs communicated by mr. price, in a letter to john canton, amfr s. *Philosophical transactions of the Royal Society of London*, (53):370–418.

Ben-Gal, A., Agam, N., Alchanatis, V., Cohen, Y., Yermiyahu, U., Zipori, I., Presnov, E., Sprintsin, M., and Dag, A. (2009). Evaluating water stress in irrigated olives: correlation of soil water status, tree water status, and thermal imagery. *Irrigation Science*, 27(5):367–376.

Bian, J., Zhang, Z., Chen, J., Chen, H., Cui, C., Li, X., Chen, S., and Fu, Q. (2019). Simplified evaluation of cotton water stress using high resolution unmanned aerial vehicle thermal imagery. *Remote Sensing*, 11(3):267.

Bibliography

Birth, G. S. and McVey, G. R. (1968). Measuring the color of growing turf with a reflectance spectrophotometer 1. *Agronomy Journal*, 60(6):640–643.

BorgognoMondino, E. and Gajetti, M. (2017). Preliminary considerations about costs and potential market of remote sensing from uav in the italian viticulture context. *European Journal of Remote Sensing*, 50(1):310–319.

Boschetti, M., Busetto, L., Ranghetti, L., Haro, J. G., Campos-Taberner, M., and Confalonieri, R. (2018). Testing multi-sensors time series of lai estimates to monitor rice phenology: Preliminary results. In *IGARSS 2018-2018 IEEE International Geoscience and Remote Sensing Symposium*, pages 8221–8224. IEEE.

Burrough, P. A., McDonnell, R., McDonnell, R. A., and Lloyd, C. D. (2015). *Principles of geographical information systems*. Oxford university press.

Caruso, G., Zarco-Tejada, P. J., Gonzalez-Dugo, V., Moriondo, M., Tozzini, L., Palai, G., Rallo, G., Hornero, A., Primicerio, J., and Gucci, R. (2019). High-resolution imagery acquired from an unmanned platform to estimate biophysical and geometrical parameters of olive trees under different irrigation regimes. *PloS one*, 14(1).

Castellarin, S. D., Bucchetti, B., Falginella, L., and Peterlunger, E. (2011). Influenza del deficit idrico sulla qualità delle uve: Aspetti fisiologici e molecolari. *Italus Hortus*, 18(1):63–79.

Castrignanò, A., Buttafuoco, G., Quarto, R., Vitti, C., Langella, G., Terribile, F., and Venezia, A. (2017). A combined approach of sensor data fusion and multivariate geostatistics for delineation of homogeneous zones in an agricultural field. *Sensors*, 17(12):2794.

Chang, C.-W., Laird, D. A., Mausbach, M. J., and Hurburgh, C. R. (2001). Near-infrared reflectance spectroscopy–principal components regression analyses of soil properties. *Soil Science Society of America Journal*, 65(2):480–490.

Chen, Y. (2015). A new methodology of spatial cross-correlation analysis. *PloS one*, 10(5):e0126158.

Cinat, P., Di Gennaro, S. F., Berton, A., and Matese, A. (2019). Comparison of unsupervised algorithms for vineyard canopy segmentation from uav multispectral images. *Remote Sensing*, 11(9):1023.

Cohen, Y., Alchanatis, V., Meron, M., Saranga, Y., and Tsipris, J. (2005). Estimation of leaf water potential by thermal imagery and spatial analysis. *Journal of experimental botany*, 56(417):1843–1852.

Colomina, I. and Molina, P. (2014). Unmanned aerial systems for photogrammetry and remote sensing: A review. *ISPRS Journal of photogrammetry and remote sensing*, 92:79–97.

Corwin, D., Lesch, S., Shouse, P., Soppe, R., and Ayars, J. (2003). Identifying soil properties that influence cotton yield using soil sampling directed by apparent soil electrical conductivity. *Agronomy Journal*, 95(2):352–364.

Corwin, D. L. (2008). Past, present, and future trends in soil electrical conductivity measurements using geophysical methods. *Handbook of agricultural geophysics*, pages 17–44.

Costa, J., Vaz, M., Escalona, J., Egipto, R., Lopes, C., Medrano, H., and Chaves, M. (2016). Modern viticulture in southern europe: vulnerabilities and strategies for adaptation to water scarcity. *Agricultural Water Management*, 164:5–18.

Dash, J., Pearse, G., and Watt, M. (2018). Uav multispectral imagery can complement satellite data for monitoring forest health. *Remote Sensing*, 10(8):1216.

De Benedetto, D., Castrignanò, A., Rinaldi, M., Ruggieri, S., Santoro, F., Figorito, B., Gualano, S., Diacono, M., and Tamborrino, R. (2013). An approach for delineating homogeneous zones by using multi-sensor data. *Geoderma*, 199:117–127.

De Castro, A., Jiménez-Brenes, F., Torres-Sánchez, J., Peña, J., Borra-Serrano, I., and López-Granados, F. (2018a). 3-d characterization of vineyards using a novel uav imagery-based obia procedure for precision viticulture applications. *Remote Sensing*, 10(4):584.

De Castro, A. I., Torres-Sánchez, J., Peña, J. M., Jiménez-Brenes, F. M., Csillik, O., and López-Granados, F. (2018b). An automatic random forest-obia algorithm for early weed mapping between and within crop rows using uav imagery. *Remote Sensing*, 10(2):285.

Di Gennaro, S. F., Dainelli, R., Palliotti, A., Toscano, P., and Matese, A. (2019). Sentinel-2 validation for spatial variability assessment in overhead trellis system viticulture versus uav and agronomic data. *Remote Sensing*, 11(21):2573.

Dong, X., Zhang, Z., Yu, R., Tian, Q., and Zhu, X. (2020). Extraction of information about individual trees from high-spatial-resolution uav-acquired images of an orchard. *Remote Sensing*, 12(1):133.

Duane, C. B. (1971). Close-range camera calibration. *Photogramm. Eng*, 37(8):855–866.

El-Hakim, S. (1986). Real-time image metrology with ccd cameras. *Photogrammetric Engineering and Remote Sensing*, 52(11):1757–1766.

Fernández-Guisuraga, J., Sanz-Ablanedo, E., Suárez-Seoane, S., and Calvo, L. (2018). Using unmanned aerial vehicles in postfire vegetation survey campaigns through large and heterogeneous areas: Opportunities and challenges. *Sensors*, 18(2):586.

Franzini, M., Ronchetti, G., Sona, G., and Casella, V. (2019). Geometric and radiometric consistency of parrot sequoia multispectral imagery for precision agriculture applications. *Applied Sciences*, 9(24):5314.

Freidenreich, A., Barraza, G., Jayachandran, K., and Khoddamzadeh, A. A. (2019). Precision agriculture application for sustainable nitrogen management of justicia brandegeana using optical sensor technology. *Agriculture*, 9(5):98.

Fridgen, J. J., Kitchen, N. R., Sudduth, K. A., Drummond, S. T., Wiebold, W. J., and Fraisse, C. W. (2004). Management zone analyst (mza). *Agronomy Journal*, 96(1):100–108.

Fritz, S., See, L., Bayas, J. C. L., Waldner, F., Jacques, D., Becker-Reshef, I., Whitcraft, A., Baruth, B., Bonifacio, R., Crutchfield, J., et al. (2019). A comparison of global agricultural monitoring systems and current gaps. *Agricultural systems*, 168:258–272.

Geman, S. and Geman, D. (1984). Stochastic relaxation, gibbs distributions, and the bayesian restoration of images. *IEEE Transactions on pattern analysis and machine intelligence*, (6):721–741.

Gerhards, M., Schlerf, M., Rascher, U., Udelhoven, T., Juszczak, R., Alberti, G., Miglietta, F., and Inoue, Y. (2018). Analysis of airborne optical and thermal imagery for detection of water stress symptoms. *Remote Sensing*, 10(7):1139.

Gitelson, A. and Merzlyak, M. N. (1994). Spectral reflectance changes associated with autumn senescence of aesculus hippocastanum l. and acer platanoides l. leaves. spectral features and relation to chlorophyll estimation. *Journal of Plant Physiology*, 143(3):286–292.

Gitelson, A. A., Kaufman, Y. J., and Merzlyak, M. N. (1996). Use of a green channel in remote sensing of global vegetation from eos-modis. *Remote sensing of Environment*, 58(3):289–298.

Gitelson, A. A., Kaufman, Y. J., Stark, R., and Rundquist, D. (2002). Novel algorithms for remote estimation of vegetation fraction. *Remote sensing of Environment*, 80(1):76–87.

Gómez-Candón, D., Virlet, N., Labbé, S., Jolivot, A., and Regnard, J.-L. (2016). Field phenotyping of water stress at tree scale by uav-sensed imagery: new insights for thermal acquisition and calibration. *Precision Agriculture*, 17(6):786–800.

Gonzalez, R. C. and Woods, R. E. (1992). Digital imaging processing. *Massachusetts: Addison-Wesley*.

Gonzalez-Dugo, V., Zarco-Tejada, P., Nicolás, E., Nortes, P. A., Alarcón, J., Intrigliolo, D. S., and Fereres, E. (2013). Using high resolution uav thermal imagery to assess the variability in the water status of five fruit tree species within a commercial orchard. *Precision Agriculture*, 14(6):660–678.

González-Piqueras, J., Sánchez, S., Villodre, J., López, H., Calera, A., Hernández-López, D., and Sánchez, J. M. (2018). Radiometric performance of multispectral camera applied to operational precision agriculture. In *IGARSS 2018-2018 IEEE International Geoscience and Remote Sensing Symposium*, pages 3393–3396. IEEE.

Guerini Filho, M., Kuplich, T. M., and Quadros, F. L. D. (2019). Estimating natural grassland biomass by vegetation indices using sentinel 2 remote sensing data. *International Journal of Remote Sensing*, 41(8):2861–2876.

Bibliography

Guo, Y., Senthilnath, J., Wu, W., Zhang, X., Zeng, Z., and Huang, H. (2019). Radiometric calibration for multispectral camera of different imaging conditions mounted on a uav platform. *Sustainability*, 11(4):978.

Haralick, R. M., Shanmugam, K., and Dinstein, I. H. (1973). Textural features for image classification. *IEEE Transactions on systems, man, and cybernetics*, (6):610–621.

Hoffmann, H., Jensen, R., Thomsen, A., Nieto, H., Rasmussen, J., and Friborg, T. (2016). Crop water stress maps for an entire growing season from visible and thermal uav imagery.

Honkavaara, E. and Khoramshahi, E. (2018). Radiometric correction of close-range spectral image blocks captured using an unmanned aerial vehicle with a radiometric block adjustment. *Remote Sensing*, 10(2):256.

Huete, A. R. (1988). A soil-adjusted vegetation index (savi). *Remote sensing of environment*, 25(3):295–309.

Iqbal, F., Lucieer, A., and Barry, K. (2018). Simplified radiometric calibration for uas-mounted multispectral sensor. *European Journal of Remote Sensing*, 51(1):301–313.

Jones, H. G., Stoll, M., Santos, T., Sousa, C. d., Chaves, M. M., and Grant, O. M. (2002). Use of infrared thermography for monitoring stomatal closure in the field: application to grapevine. *Journal of Experimental Botany*, 53(378):2249–2260.

Kannala, J. and Brandt, S. S. (2006). A generic camera model and calibration method for conventional, wide-angle, and fish-eye lenses. *IEEE transactions on pattern analysis and machine intelligence*, 28(8):1335–1340.

Katsigiannis, P., Misopolinos, L., Liakopoulos, V., Alexandridis, T. K., and Zalidis, G. (2016). An autonomous multi-sensor uav system for reduced-input precision agriculture applications. In *2016 24th Mediterranean Conference on Control and Automation (MED)*, pages 60–64. IEEE.

Kaufman, Y. J. and Tanre, D. (1992). Atmospherically resistant vegetation index (arvi) for eos-modis. *IEEE transactions on Geoscience and Remote Sensing*, 30(2):261–270.

Khaliq, A., Comba, L., Biglia, A., Ricauda Aimonino, D., Chiaberge, M., and Gay, P. (2019). Comparison of satellite and uav-based multispectral imagery for vineyard variability assessment. *Remote Sensing*, 11(4):436.

Labbé, S., Lebourgeois, V., Jolivot, A., Marti, R., et al. (2012). Thermal infra-red remote sensing for water stress estimation in agriculture. *Options Méditerranéennes: Série B. Etudes et Recherches*, (67):175–184.

Li, B., Xu, X., Han, J., Zhang, L., Bian, C., Jin, L., and Liu, J. (2019). The estimation of crop emergence in potatoes by uav rgb imagery. *Plant methods*, 15(1):15.

López-Lozano, R., Casterad, M., and Herrero, J. (2010). Site-specific management units in a commercial maize plot delineated using very high resolution remote sensing and soil properties mapping. *Computers and Electronics in Agriculture*, 73(2):219–229.

López-Lozano, R., Duveiller, G., Seguini, L., Meroni, M., García-Condado, S., Hooker, J., Leo, O., and Baruth, B. (2015). Towards regional grain yield forecasting with 1 km-resolution eo biophysical products: Strengths and limitations at pan-european level. *Agricultural and Forest Meteorology*, 206:12–32.

MacQueen, J. et al. (1967). Some methods for classification and analysis of multivariate observations. In *Proceedings of the fifth Berkeley symposium on mathematical statistics and probability*, volume 1, pages 281–297. Oakland, CA, USA.

Maes, W. H. and Steppe, K. (2019). Perspectives for remote sensing with unmanned aerial vehicles in precision agriculture. *Trends in plant science*, 24(2):152–164.

Mafanya, M., Tsele, P., Botai, J. O., Manyama, P., Chirima, G. J., and Monate, T. (2018). Radiometric calibration framework for ultra-high-resolution uav-derived orthomosaics for large-scale mapping of invasive alien plants in semi-arid woodlands: Harrisia pomanensis as a case study. *International Journal of Remote Sensing*, 39(15-16):5119–5140.

Marino, A. and Marotta, F. (2019). Crop rows detection through uav images. *Master Degree Final Dissertation, Politecnico di Milano*.

Marques, P., Pádua, L., Adão, T., Hruška, J., Peres, E., Sousa, A., and Sousa, J. J. (2019). Uav-based automatic detection and monitoring of chestnut trees. *Remote Sensing*, 11(7):855.

Martin, F.-M., Müllerová, J., Borgniet, L., Dommanget, F., Breton, V., and Evette, A. (2018). Using single-and multidate uav and satellite imagery to accurately monitor invasive knotweed species. *Remote Sensing*, 10(10):1662.

Martínez-Casasnovas, J., Arnó, J., et al. (2018). Use of farmer knowledge in the delineation of potential management zones in precision agriculture: a case study in maize (zea mays l.). *Agriculture*, 8(6):84.

Matese, A., Di Gennaro, S. F., Nardi, D., and Potena, C. (2016). Piattaforme a controllo remoto e robotiche per il monitoraggio e la gestione delle colture. *Agricoltura di precisione. Metodi e tecnologie per migliorare l'efficienza e la sostenibilita dei sistemi colturali*.

Matese, A., Toscano, P., Di Gennaro, S. F., Genesio, L., Vaccari, F., Primicerio, J., Belli, C., Zaldei, A., Bianconi, R., and Gioli, B. (2015). Intercomparison of uav, aircraft and satellite remote sensing platforms for precision viticulture. *Remote Sensing*, 7(3):2971–2990.

Meron, M., Tsipris, J., and Charitt, D. (2003). Remote mapping of crop water status to assess spatial variability of crop stress. In *Precision agriculture. Proceedings of the fourth European conference on precision agriculture. Academic Publishers, Berlin*, pages 405–410.

Möller, M., Alchanatis, V., Cohen, Y., Meron, M., Tsipris, J., Naor, A., Ostrovsky, V., Sprintsin, M., and Cohen, S. (2006). Use of thermal and visible imagery for estimating crop water status of irrigated grapevine. *Journal of experimental botany*, 58(4):827–838.

Moral, F., Terrón, J., and Da Silva, J. M. (2010). Delineation of management zones using mobile measurements of soil apparent electrical conductivity and multivariate geostatistical techniques. *Soil and Tillage Research*, 106(2):335–343.

Morari, F., Castrignanò, A., and Pagliarin, C. (2009). Application of multivariate geostatistics in delineating management zones within a gravelly vineyard using geo-electrical sensors. *Computers and Electronics in Agriculture*, 68(1):97–107.

Mulla, D. and Khosla, R. (2016). Historical evolution and recent advances in precision farming. *Soil-Specific Farming*.

Mulla, D. J. (2013). Twenty five years of remote sensing in precision agriculture: Key advances and remaining knowledge gaps. *Biosystems engineering*, 114(4):358–371.

Nawar, S., Corstanje, R., Halcro, G., Mulla, D., and Mouazen, A. M. (2017). Delineation of soil management zones for variable-rate fertilization: A review. In *Advances in agronomy*, volume 143, pages 175–245. Elsevier.

Nebiker, S., Annen, A., Scherrer, M., and Oesch, D. (2008). A light-weight multispectral sensor for micro uav: Opportunities for very high resolution airborne remote sensing. *The international archives of the photogrammetry, remote sensing and spatial information sciences*, 37(B1):1193–1199.

Nebiker, S., Lack, N., Abächerli, M., and Läderach, S. (2016). Light-weight multispectral uav sensors and their capabilities for predicting grain yield and detecting plant diseases. *International Archives of the Photogrammetry, Remote Sensing & Spatial Information Sciences*, 41.

Neupane, J. and Guo, W. (2019). Agronomic basis and strategies for precision water management: a review. *Agronomy*, 9(2):87.

Nixon, D., Salgado-García, S., Gurasamy, S., Crout, N., and Rodrigues, F. (2017). An overview of the mexican crop observation, management and production analysis services system (compass) project. In *39th convention of the Asociación de Técnicos Azucareros de México, Veracruz, Mexico*.

Nonni, F., Malacarne, D., Pappalardo, S. E., Codato, D., Meggio, F., and De Marchi, M. (2018). Sentinel-2 data analysis and comparison with uav multispectral images for precision viticulture. In *GI Forum*, volume 1, pages 105–116.

Oliver, M. A., Bishop, T. F., Marchant, B. P., et al. (2013). *Precision agriculture for sustainability and environmental protection*. Routledge Abingdon.

Ortuani, B., Sona, G., Ronchetti, G., Mayer, A., and Facchi, A. (2019). Integrating geophysical and multispectral data to delineate homogeneous management zones within a vineyard in northern italy. *Sensors*, 19(18):3974.

Bibliography

Pachauri, R. K., Allen, M. R., Barros, V. R., Broome, J., Cramer, W., Christ, R., Church, J. A., Clarke, L., Dahe, Q., Dasgupta, P., et al. (2014). *Climate change 2014: synthesis report. Contribution of Working Groups I, II and III to the fifth assessment report of the Intergovernmental Panel on Climate Change*. Ipcc.

Pádua, L., Marques, P., Hruška, J., Adão, T., Bessa, J., Sousa, A., Peres, E., Morais, R., and Sousa, J. J. (2018a). Vineyard properties extraction combining uas-based rgb imagery with elevation data. *International Journal of Remote Sensing*, 39(15-16):5377–5401.

Pádua, L., Marques, P., Hruška, J., Adão, T., Peres, E., Morais, R., and Sousa, J. (2018b). Multi-temporal vineyard monitoring through uav-based rgb imagery. *Remote Sensing*, 10(12):1907.

Pádua, L., Vanko, J., Hruška, J., Adão, T., Sousa, J. J., Peres, E., and Morais, R. (2017). Uas, sensors, and data processing in agroforestry: A review towards practical applications. *International Journal of Remote Sensing*, 38(8-10):2349–2391.

Park, S., Ryu, D., Fuentes, S., Chung, H., Hernández-Montes, E., and O′ Connell, M. (2017). Adaptive estimation of crop water stress in nectarine and peach orchards using high-resolution imagery from an unmanned aerial vehicle (uav). *Remote Sensing*, 9(8):828.

Pascucci, S., Carfora, M., Palombo, A., Pignatti, S., Casa, R., Pepe, M., and Castaldi, F. (2018). A comparison between standard and functional clustering methodologies: Application to agricultural fields for yield pattern assessment. *Remote Sensing*, 10(4):585.

Perfetti, L., Polari, C., Fassi, F., et al. (2017). Fisheye photogrammetry: tests and methodologies for the survey of narrow spaces. *International Archives of the Photogrammetry, Remote Sensing and Spatial Information Sciences*, 42(W3):573–580.

Poblete-Echeverría, C., Olmedo, G., Ingram, B., and Bardeen, M. (2017). Detection and segmentation of vine canopy in ultra-high spatial resolution rgb imagery obtained from unmanned aerial vehicle (uav): A case study in a commercial vineyard. *Remote Sensing*, 9(3):268.

Poncet, A. M., Knappenberger, T., Brodbeck, C., Fogle, M., Shaw, J. N., and Ortiz, B. V. (2019). Multispectral uas data accuracy for different radiometric calibration methods. *Remote Sensing*, 11(16):1917.

Priori, S., Martini, E., Andrenelli, M., Magini, S., Agnelli, A., Bucelli, P., Biagi, M., Pellegrini, S., and Costantini, E. (2013). Improving wine quality through harvest zoning and combined use of remote and soil proximal sensing. *Soil Science Society of America Journal*, 77(4):1338–1348.

Puliti, S., Saarela, S., Gobakken, T., Ståhl, G., and Næsset, E. (2018). Combining uav and sentinel-2 auxiliary data for forest growing stock volume estimation through hierarchical model-based inference. *Remote Sensing of Environment*, 204:485–497.

Quebrajo, L., Perez-Ruiz, M., Pérez-Urrestarazu, L., Martínez, G., and Egea, G. (2018). Linking thermal imaging and soil remote sensing to enhance irrigation management of sugar beet. *Biosystems Engineering*, 165:77–87.

Richardson, A. D., Jenkins, J. P., Braswell, B. H., Hollinger, D. Y., Ollinger, S. V., and Smith, M.-L. (2007). Use of digital webcam images to track spring green-up in a deciduous broadleaf forest. *Oecologia*, 152(2):323–334.

Ronchetti, G., Pagliari, D., and Sona, G. (2018). Dtm generation through uav survey with a fisheye camera on a vineyard. *ISPRS - International Archives of the Photogrammetry, Remote Sensing and Spatial Information Sciences*, XLII-2:983–989.

Ross, S. M. (2003). *Probabilità e statistica per l'ingegneria e le scienze*. Apogeo Editore.

Rossel, R. V., Walvoort, D., McBratney, A., Janik, L. J., and Skjemstad, J. (2006). Visible, near infrared, mid infrared or combined diffuse reflectance spectroscopy for simultaneous assessment of various soil properties. *Geoderma*, 131(1-2):59–75.

Rouse Jr, J., Haas, R., Schell, J., and Deering, D. (1974). Monitoring vegetation systems in the great plains with erts.

Salamí, E., Barrado, C., and Pastor, E. (2014). Uav flight experiments applied to the remote sensing of vegetated areas. *Remote Sensing*, 6(11):11051–11081.

Sashikkumar, M., Selvam, S., Karthikeyan, N., Ramanamurthy, J., Venkatramanan, S., and Singaraja, C. (2017). Remote sensing for recognition and monitoring of vegetation affected by soil properties. *Journal of the Geological Society of India*, 90(5):609–615.

Scaramuzza, D., Martinelli, A., and Siegwart, R. (2006). A toolbox for easily calibrating omnidirectional cameras. In *2006 IEEE/RSJ International Conference on Intelligent Robots and Systems*, pages 5695–5701. IEEE.

Schmidt, F. and Persson, A. (2003). Comparison of dem data capture and topographic wetness indices. *Precision Agriculture*, 4(2):179–192.

Scudiero, E., Teatini, P., Corwin, D. L., Deiana, R., Berti, A., and Morari, F. (2013). Delineation of site-specific management units in a saline region at the venice lagoon margin, italy, using soil reflectance and apparent electrical conductivity. *Computers and electronics in agriculture*, 99:54–64.

Scudiero, E., Teatini, P., Manoli, G., Braga, F., Skaggs, T., and Morari, F. (2018). Workflow to establish time-specific zones in precision agriculture by spatiotemporal integration of plant and soil sensing data. *Agronomy*, 8(11):253.

Seifert, E., Seifert, S., Vogt, H., Drew, D., Van Aardt, J., Kunneke, A., and Seifert, T. (2019). Influence of drone altitude, image overlap, and optical sensor resolution on multi-view reconstruction of forest images. *Remote Sensing*, 11(10):1252.

Shaddad, S., Madrau, S., Castrignanò, A., and Mouazen, A. (2016). Data fusion techniques for delineation of site-specific management zones in a field in uk. *Precision agriculture*, 17(2):200–217.

Silva, B. M., Silva, S. H. G., Oliveira, G. C. d., Peters, P. H. C. R., Santos, W. J. R. d., and Curi, N. (2014). Soil moisture assessed by digital mapping techniques and its field validation. *Ciência e Agrotecnologia*, 38(2):140–148.

Smith, G. M. and Milton, E. J. (1999). The use of the empirical line method to calibrate remotely sensed data to reflectance. *International Journal of remote sensing*, 20(13):2653–2662.

Sona, G., Pinto, L., Pagliari, D., Passoni, D., and Gini, R. (2014). Experimental analysis of different software packages for orientation and digital surface modelling from uav images. *Earth Science Informatics*, 7(2):97–107.

Sörensen, R., Zinko, U., and Seibert, J. (2006). On the calculation of the topographic wetness index: evaluation of different methods based on field observations. *Hydrology and Earth System Sciences Discussions*, 10(1):101–112.

Stow, D., Nichol, C. J., Wade, T., Assmann, J. J., Simpson, G., and Helfter, C. (2019). Illumination geometry and flying height influence surface reflectance and ndvi derived from multispectral uas imagery. *Drones*, 3(3):55.

Stroppiana, D., Pepe, M., Boschetti, M., Crema, A., Candiani, G., Giordan, D., Baldo, M., Allasia, P., and Monopoli, L. (2019). Estimating crop density from multi-spectral uav imagery in maize crop. *International Archives of the Photogrammetry, Remote Sensing & Spatial Information Sciences*.

Stroppiana, D., Villa, P., Sona, G., Ronchetti, G., Candiani, G., Pepe, M., Busetto, L., Migliazzi, M., and Boschetti, M. (2018). Early season weed mapping in rice crops using multi-spectral uav data. *International Journal of Remote Sensing*, 39(15-16):5432–5452.

Teal, R., Tubana, B., Girma, K., Freeman, K., Arnall, D., Walsh, O., and Raun, W. (2006). In-season prediction of corn grain yield potential using normalized difference vegetation index. *Agronomy Journal*, 98(6):1488–1494.

Tsouros, D. C., Bibi, S., and Sarigiannidis, P. G. (2019). A review on uav-based applications for precision agriculture. *Information*, 10(11):349.

Tu, Y.-H., Phinn, S., Johansen, K., and Robson, A. (2018). Assessing radiometric correction approaches for multispectral uas imagery for horticultural applications. *Remote Sensing*, 10(11):1684.

Tucci, G., Parisi, E. I., Castelli, G., Errico, A., Corongiu, M., Sona, G., Viviani, E., Bresci, E., and Preti, F. (2019). Multi-sensor uav application for thermal analysis on a dry-stone terraced vineyard in rural tuscany landscape. *ISPRS International Journal of Geo-Information*, 8(2):87.

Tucker, C., Holben, B., Elgin Jr, J., McMurtrey III, J., et al. (1980). Relationship of spectral data to grain yield variation. *Photogrammetric Engineering and Remote Sensing*, 46(5):657–666.

Usda, N. (2004). Soil survey laboratory methods manual. *Soil survey investigations report*, 42.

Van Meirvenne, M., Islam, M. M., De Smedt, P., Meerschman, E., Van De Vijver, E., and Saey, T. (2013). Key variables for the identification of soil management classes in the aeolian landscapes of north–west europe. *Geoderma*, 199:99–105.

Veysi, S., Naseri, A. A., Hamzeh, S., and Bartholomeus, H. (2017). A satellite based crop water stress index for irrigation scheduling in sugarcane fields. *Agricultural water management*, 189:70–86.

Weiss, M. and Baret, F. (2017). Using 3d point clouds derived from uav rgb imagery to describe vineyard 3d macro-structure. *Remote Sensing*, 9(2):111.

Wierzbicki, D., Kedzierski, M., Fryskowska, A., and Jasinski, J. (2018). Quality assessment of the bidirectional reflectance distribution function for nir imagery sequences from uav. *Remote Sensing*, 10(9):1348.

Woebbecke, D. M., Meyer, G. E., Von Bargen, K., and Mortensen, D. (1995). Color indices for weed identification under various soil, residue, and lighting conditions. *Transactions of the ASAE*, 38(1):259–269.

WWAP/ UN-Water (2018). *The United Nations World Water Development Report 2018: Nature-Based Solutions for Water*. United Nations World Water Assessment Programme. UNESCO, Paris.

Zarco-Tejada, P. J., Diaz-Varela, R., Angileri, V., and Loudjani, P. (2014). Tree height quantification using very high resolution imagery acquired from an unmanned aerial vehicle (uav) and automatic 3d photo-reconstruction methods. *European journal of agronomy*, 55:89–99.

Zhang, L., Niu, Y., Zhang, H., Han, W., Li, G., Tang, J., and Peng, X. (2019a). Maize canopy temperature extracted from uav thermal and rgb imagery and its application in water stress monitoring. *Frontiers in plant science*, 10:1270.

Zhang, S., Zhao, G., Lang, K., Su, B., Chen, X., Xi, X., and Zhang, H. (2019b). Integrated satellite, unmanned aerial vehicle (uav) and ground inversion of the spad of winter wheat in the reviving stage. *Sensors*, 19(7):1485.

Zhao, L., Shi, Y., Liu, B., Hovis, C., Duan, Y., and Shi, Z. (2019). Finer classification of crops by fusing uav images and sentinel-2a data. *Remote Sensing*, 11(24):3012.